UNIVERSIDADE ESTADUAL DE CAMPINAS
Instituto de Física "Gleb Wataghin"

NATALY ZARIBETH HERRERA REINOZA

Growth of carbon nanostructures and doped Graphene via bottom-up methods

Crescimento de nanoestruturas de carbono e grafeno dopado via métodos bottom-up

CAMPINAS
2022

NATALY ZARIBETH HERRERA REINOZA

Growth of carbon nanostructures and doped graphene via bottom-up methods

Crescimento de nanoestruturas de carbono e grafeno dopado via métodos bottom-up

Thesis presented to the Institute of Physics "Gleb Wataghin" of the University of Campinas in partial fulfillment of the requirements for the degree of Doctor in Science, in the field of Physics.

Tese de doutorado apresentada ao Instituto de Física "Gleb Wataghin" da Universidade Estadual de Campinas como parte dos requisitos exigidos para a obtenção do título de Doutora em Ciências, na Área de Física.

Advisor/Orientador: Prof. Dr. Abner de Siervo

Este exemplar corresponde à versão final da tese defendida pela aluna Nataly Zaribeth Herrera Reinoza, e orientada pelo Prof. Dr. Abner de Siervo.

CAMPINAS
2022

Ficha catalográfica
Universidade Estadual de Campinas
Biblioteca do Instituto de Física Gleb Wataghin
Lucimeire de Oliveira Silva da Rocha - CRB 8/9174

H433g

Herrera Reinoza, Nataly Zaribeth, 1989-
Growth of carbon nanostructures and doped graphene via bottom-up methods / Nataly Zaribeth Herrera Reinoza. – Campinas, SP : [s.n.], 2022.

Orientador: Abner de Siervo.
Tese (doutorado) – Universidade Estadual de Campinas, Instituto de Física Gleb Wataghin.

1. Reação de acoplamento de Ullmann. 2. Microscopia de tunelamento de elétrons. 3. Nitreto de boro hexagonal. 4. Grafeno dopado. 5. Porfirinas. I. Siervo, Abner de, 1972-. II. Universidade Estadual de Campinas. Instituto de Física Gleb Wataghin. III. Título.

Informações Complementares

Título em outro idioma: Crescimiento de nanoestructuras de carbono e grafeno dopado via métodos bottom-up
Palavras-chave em inglês:
Ullmann coupling reaction
Scanning tunneling microscopy
Hexagonal boron nitride
Doped graphene
Porphyrins
Área de concentração: Física
Titulação: Doutora em Ciências
Banca examinadora:
Abner de Siervo [Orientador]
Luiz Fernando Zagonel
Tulio Costa Rizuti da Rocha
Fernando Loureiro Stavale Junior
Roberto Magalhães Paniago
Data de defesa: 20-10-2022
Programa de Pós-Graduação: Física

Identificação e informações acadêmicas do(a) aluno(a)
- ORCID do autor: https://orcid.org/0000-0001-5658-9692
- Currículo Lattes do autor: http://lattes.cnpq.br/5419841306617429

MEMBROS DA COMISSÃO EXAMINADORA DA TESE DE DOUTORADO DA ALUNA NATALY ZARIBETH HERRERA REINOZA - RA 226527 APRESENTADA E APROVADA AO INSTITUTO DE FÍSICA “GLEB WATAGHIN”, DA UNIVERSIDADE ESTADUAL DE CAMPINAS, EM 20/10/2022.

COMISSÃO JULGADORA:

- Prof. Dr. Abner de Siervo – Presidente e orientador (IFGW/UNICAMP)

- Prof. Dr. Luiz Fernando Zagonel (IFGW/UNICAMP)

- Prof. Dr. Tulio Costa Rizuti da Rocha (CNPEM/LNLS)

- Prof. Dr. Fernando Loureiro Stavale Junior (CBPF)

- Prof. Dr. Roberto Magalhães Paniago (DF/UFMG)

OBS.: Ata da defesa com as respectivas assinaturas dos membros encontra-se no SIGA/Sistema de Fluxo de Dissertação/Tese e na Secretaria do Programa da Unidade.

CAMPINAS

2022

A Wilson e Nacaré.

Acknowledgements

Em primeiro lugar, gostaria de expressar o meu profundo agradecimento ao meu orientador, o Prof. Abner de Siervo, por sua confiança, motivação e amizade durante estes quase quatro anos. Agradeço as múltiplas discussões que me permitiram crescer tanto profissional como pessoalmente, sempre me impulsionando a dar o melhor de mim. Estarei sempre grata por ter aberto as portas do laboratório de Física de Superfícies para mim.

I want to give my deepest gratitude to Thomas Jung, for the opportunity to work in his group at Paul Scherrer Institut (PSI) in Switzerland during my P.h. D. internship. I acknowledge his magnific scientific and personal support. Thank you very much for hearing me and offering your valuable friendship.

Ao Prof. Luis Herique de Lima por ter colaborado no meu projeto de doutorado, pela dedicação e discussões científicas. I also want to thank Prof. Duncan John Mowbray and Prof. Alejandro Pérez Paz for the exciting discussions and for providing the theoretical calculations which support some of our experimental results.

También agradezco al Prof. Rodrigo Casanova Bautista, quien fue mi mentor en la Universidad de Los Andes en Venezuela y me mostró con su ejemplo que hacer lo que te apasiona siempre genera satisfacción.

Aos membros do grupo de Física de Superfícies, em especial ao Prof. Richard Landers por todos seus ensinamentos e interessantes discussões. Aos meus colegas Rodrigo, Isabela e Gabriela. Em especial ao Alisson, pela amizade e a parceria no lab.

I want to express my gratitude to everyone helping me during my stay in Switzerland. Specially thank Aisha Ahsan and Rejaul SK for sharing their knowledge and all the interesting discussions. Igualmente quero agradecer a Markus Kropf, aprendi muito de você, e Angelita Kroff, a amizade de vocês fez tudo a diferença.

Agradezco a mi mamá Nacaré, cuyo amor incondicional me ha fortalecido en cada etapa de mi vida. Tú cuidado, apoyo y comprensión me han mantenido en pie.

Me siento profundamente agradecida con Ricardo. Por tu amor, comprensión y apoyo constante e incondicional durante todos estos años juntos. Gracias por haber creído en mí y alentarme a continuar adelante.

A mi amada Isabella, a tu lado las dudas se disipan. El amor que siento por ti le da sentido a mi vida. Gracias por entender, esperar y acompañar mamá.

Às professoras do Centro de Convivência Infantil da Unicamp: Valquíria, Teresa, Izamelia, Lindaura, Jessica, Fabiola, Sandra, Katia e Roseli, por ter cuidado com tanto amor da minha filha.

Ao Ministério da Ciência, Tecnologia e Inovações" e "Conselho Nacional de Desenvolvimento Científico e Tecnológico – CNPq pelo financiamento do doutorado através do processo nº 140721/2019-3

À Unicamp, à equipe administrativa do DFA e da secretaria da pós-graduação do IFGW, en especial a Luciana e Alessandra.

Agradeço ao Brasil por ter me acolhido durante estes quase seis anos, e me proporcionar as condições necessárias para continuar minha carreira acadêmica.

Resumo

Apresentamos uma investigação sistemática da síntese de nanoestruturas de carbono e de grafeno dopado (Gr) por meio de métodos de crescimentos *bottom-up*. Utilizamos microscopia de tunelamento em varredura e espectroscopia de tunelamento de eletrons (STM/STS) para explorar a morfologia das amostras durante a síntese e suas propriedades eletrônicas locais, enquanto a espectroscopia de fotoelétrons de raios-X (XPS) foi empregada para estudar o estado químico da amostra. Cálculos da teoria do funcional da densidade (DFT) foram realizados para suportar nossos resultados experimentais.

Em primeiro lugar, apresentamos o crescimento de monocamadas de boro-nitrogênio-carbono (h-BNC) na hexagonais a partir de um único e novo precursor molecular (hexametil borazina – $C6H18B_3N_3$) superfície de Ir(111). A partir de imagens de STM combinadas com cálculo DFT, demonstramos que o h-BNC é formado pela dopagem de Gr com $(BN)_8$ unidades dispostas em conformação de seis anéis, localizadas nas regiões tipo fcc e hcp do padrão moiré do Gr na superfície do Ir(111). Isso limita sua densidade em Gr e minimiza a segregação. Experimentos adicionais foram realizados em Rh(111), os resultados mostram que a síntese de h-BNC ou heteroestruturas laterais Gr-hBN a partir de um único precursor molecular não ocorre nesta superfície, devido a interdifusão dos átomos de carbono no cristal de Rh na temperatura de crescimento de h-BN. No entanto, em Rh(111) uma monocamada de h-BN de alta qualidade foi sintetizada.

Em segundo lugar, investigamos a síntese de redes quadradas porosas organometálicas de porfirinas Br4TPP sobre a superfície Ag(100) empregando a síntese química assistida por superfícies. Diferentes motivos organometalicos foram formados à temperatura ambiente (RT). Estudamos o papel crítico da temperatura do substrato durante a deposição do precursor. Os resultados mostram que o crescimento das redes quadradas é favorecido a 450K. Combinado resultados de STM e cálculos de DFT, identificamos a conformação de adsorção molecular como saddle shape e a periodicidade de rede como sendo de $(1,90 \pm 0,03)$nm. Os cálculos sugerem que, uma vez formada a rede TPP com os átomos de Ag, a remoção desses átomos é um processo altamente energético; portanto, o sistema fica cineticamente aprisionado. Portanto, promover a ligação C-C por tratamento térmico sem destruir a rede não é possível. Foram observadas cadeias de moléculas ao longo da direção $\langle 530 \rangle$ em Ag(100) para temperaturas de deposição acima da RT. As moléculas estão em estrutura totalmente invertida, a conformação típica de adsorção relatada em Cu(111).

Finalmente, mediante o método de reação de acoplamento de Ullmann, foram sintetizadas nanofitas (GNRs) porosas de grafeno dopadas com nitrogênio sobre a superfície Ag(100) e Cu(111). Para cada superfície, investigamos a influência da temperatura do substrato durante a deposição molecular na seletividade das vias de reação, encontrando o parâmetro apropriado para o crescimento das cadeias, o que permite controlar a síntese pela temperatura do substrato. A partir de imagens de STM, observamos a coexistência de cadeias organometálicas com extremidades covalentes e GNRs constituídos por cerca de seis unidades. As influências do substrato são claramente percebidas pela orientação das cadeias metálicas e das estruturas covalentes.

Abstract

In this thesis, we present the systematic investigation of the synthesis of carbon nanostructures and doped graphene (Gr) via bottom-up methods, using a comprehensive multi-technique approach. By scanning tunneling microscopy/spectroscopy (STM/ STS) the morphology of the sample during the hierarchy synthesis and their local electronic properties were explored, while X-ray photoelectron spectroscopy (XPS) probed the chemical state of the sample. Density functional theory (DFT) calculations support our experimental results.

Firstly, we present the successful growth of hexagonal boron-nitrogen-carbon monolayer (h-BNC) from a novel single molecular precursor (hexamethyl borazine – $C_6H_{18}B_3N_3$) by chemical vapor deposition (CVD) on Ir(111). From STM images combined with DFT calculation, we have demonstrated that h-BNC is formed by doping Gr with small BN nanoclusters. The dopant was identified as $(BN)_8$ units arranged in six-fold BN rings conformation, preferably sitting in the fcc- and hcp-type regions of the Gr moiré pattern on Ir(111). This behavior limits its density on Gr and minimizes the segregation between Gr and h-NB domanis. In addition, for a BN concentration of about 17%, a band gap between 1.4 and 1.6 eV was determined, showing the material's semiconductor behavior. Additional experiments were performed on Rh(111), the results show that the synthesis of h-BNC or lateral heterostructures Gr-hBN from a single molecular precursor does not take place on the surface due to the carbon atoms strongly dissolving into the Rh bulk at h-BN growth temperature. However, on Rh(111), a high-quality h-BN monolayer was synthesized.

Secondly, we investigated the on-surface synthesis of organometallic square pore network from Br4TPP porphyrin on Ag(100). Due to the substrate reactivity and low debromination barrier, different motif coordinated by Ag adatoms were already formed at room temperature (RT). We studied the critical role of substrate temperature during the deposition of the precursor. The results show that square motif growth is favored at 450K. We identified the molecular adsorption conformation as saddle shape and the lattice periodicity as (1.90 ± 0.03)nm. The calculations suggest that once the TPP network with Ag adatoms is formed, removing these atoms is a highly energetic process; hence the system becomes kinetically trapped. Therefore promoting C-C bonding by thermal annealing without destroying the network it is not possible. Moreover, chains of molecules sit along $\langle 530 \rangle$ direction on Ag(100) were observed for deposition above RT. The molecules are in fully inverted structure. From our best knowledge, this is the first time that porphyrins are observed in an inverted structure and saddle shape on Ag(100).

Finally, by surface-assisted Ullmann coupling reaction, nitrogen-doped porous graphene nanoribbons (GNRs) were synthesized on Ag(100) and Cu(111). For each surface, we investigated the influence of the substrate temperature during molecular deposition on the selectivity of reaction pathways, finding the appropriate parameters for growing the chains, which allows controlling the synthesis by the substrate temperature. From the STM data, we observed the coexistence organometallic chains with covalent ends and GNRs constituted by about six units. The substrate's influences are clearly noticed by the orientation of the metalled chains and the covalent structures.

Contents

Chapter 1

Introduction

In 2010 A. K. Geim and K. S. Novoselov were awarded the Nobel Prize in Physics [1, 2] for isolating and characterizing graphene (Gr), a two-dimensional material formed by the arrangement of carbon atoms in an sp^2 honeycomb structure. Gr is a zero band gap material [3] with high carrier mobility [4], making it suitable for electronic device applications. However, the lack of an intrinsic bandgap strongly restricts its applications [5], for example, in electronic devices, which typically require a bandgap of about 0.4 eV, at room temperature (RT), for a satisfactory operating on/off ratio [6].

Different approaches focus on opening an energy band gap in Gr have been developed over the years. One method consists in modulating the electronic properties by functionalizing the Gr, for example, by doping the material replacing carbon atoms with other elements[7–9], or even by the chemisorption of specific molecular groups in the Gr structure [10]. Another way to induce a band gap in Gr is by electronic confinement [11], which consists in reducing one dimension of the material below 10 nm, for instance, growing graphene nanoribbons (GNRs). These structures maintain many properties of Gr. However, their nanometer width and finite edges with a specific shape (armchair [12], zigzag [13], or chiral [14]) induce the energy band gap's opening and

provide them with new electronic properties. It is also possible to tailor the graphene's properties by synthesizing graphene-related functional low-dimensional materials [15], such as polyphenylene-based polymers and carbon pore networks.

Functionalized Gr, GNRs, and carbon pore networks can be synthesized by different techniques classified into two growth approach: (i) the top-down and (ii) the bottom-up approaches. On one hand, the top-down approach involves physically shaping the desired nanostructure from bulk graphite or carbon sheets, for instance, using mechanical/chemical exfoliation or lithography [16]. On the other hand, the bottom-up approach is based on the 2D confinement of well-designed molecular building blocks (precursor) to a surface [17]. In this way, it is promoted a controlled assembly of these molecules, allowing the building of well-defined molecular nanomaterials with atomic-scale precision. In this work, we employed the bottom-up methods of chemical vapor deposition (CVD) and on-surface synthesis (OSS) for growing carbon-based nanostructures and doped Gr.

The CVD growth of functionalized Gr has been investigated in previous works. For the substitutional doping of the material, many different atoms have been used, highlighting nitrogen (N) and boron (B). These impurities are appropriated carbon substitution due to their atomic size, avoiding introducing drastic changes in the Gr lattice. N-doped Gr has been reported with an n-type doping effect and the presence of localized states in the conduction band [8], without observing an gap opening in Gr. Additionally, in the case of Gr doped with 2 % B substitution, the Fermi level is shifted -0.65 eV related to the Dirac energy, inducing a p-type conductivity. Also, this system exhibits the gap opening of 0.15 eV.

Theoretical studies have predicted the band gap opening of Gr around K (or K′) point by introducing BN units as a substitutional dopant [18–20]. First-principles calculations performed by Ren *et al.* [21] showed that 6-fold BN ring is the most stable configuration for doping Gr with BN. This dopant can open an electronic band gap in Gr. The value of the band gap opened will depend on the doping concentration. In addition, Fan *et al.* [18] investigated the electronic properties of Gr doped with BN (dimer), $(BN)_3$ (one 6-fold ring), and $(BN)_{12}$ (seven 6-fold rings) units. They reported the opening of the Gr band gap due to the charge redistribution relating to the breaking of localized symmetry of the potential. For the most stable motif, $(BN)_{12}$, the band gap opening

induced ranges from 0 to 1.2 eV depending on the BN concentration.

In that regard, synthesizing Gr doped with hexagonal boron nitride units (h-BN) represents an excellent opportunity to develop new materials with a tunable band gap. Gr doped with h-BN consists of a hexagonal monolayer formed by boron-nitrogen-carbon, which is usually called in the literature monolayer h-BNC. The first study on the growth of h-BNC was published by Ci *et al.* [22], who reported the formation of randomly distributed domains of h-BN and C phases (two segregated phases) synthesized from two molecular precursors as the source of C and BN. As expected, it was not observed an gap opening. More recent studies [23–25] using a single molecular precursor have reported the growth of h-BN and Gr domains interconnected, forming h-BN–Gr lateral structures. In this case, the superposition of Gr and h-BN bands [26] is observed instead of opening the Gr energy gap. Some theoretical works associate the formation of segregated structures with the high energy cost of forming the C–N and C–B bonds compared to B–N bonds [27–32].

The synthesis of the homogeneous ternary compound of BCN (h-BNC) instead of a segregated Gr-h-BN structure was reported for the first time by Beniwal *et al.* in 2017 [33]. In this case, the material was grown on Ir(111) surface from the single molecular precursor bis-BN cyclohexane. Nonetheless, the experimental evidence of the h-BNC atomic structure is limited, and the work is strongly supported by theoretical calculations of the BCN atomic and electronic structure. Therefore, a detailed experimental study of h-BNC at the atomic scale and its correlation with the local electronic properties is lacking. Moreover, the synthesis of h-BNC remains challenging due to the tendency to segregate in systems composed of C, N, and B.

The electronic properties of Gr can also be modulated by reducing its dimensionality; i.e. is by growing GNRs, for instance. In addition, it is possible to achieve tailored properties by synthesizing organic and metal-organic coordination networks that can emulate the Gr structure from aromatic molecular precursors. In order to build GNRs and porous molecular networks, on-surface synthesis has emerged as a growth method able to produce atomically precise nanostructures with the appropriate dimensions. For that, it is relevant to design a suitable molecular precursor and carefully choose the appropriate catalytic surface for growing the desired nanostructure. Band gap engineering of GNRs is possible by on-surface synthesis of nanoribbons with a specific structure, width, and

edge [12–14]. Doped GNRs can be directly grown from molecular precursors that already contain the doping atoms [34, 35].

GNRs and nanoporous structures based on carbon are prominent candidates for applications in transistor devices [36]. Theoretical studies have predicted a semiconductor behavior of Gr by introducing nanopores into the lattice [37]. Therefore, synthesizing these nanomaterials with specific structural symmetry and new functionalities requires exploring novel molecular precursors and new on-surface synthesis routines.

Several chemical reactions have been explored to achieve novel surface-assisted motifs, for instance, direct C-H activation [38, 39], alkyne coupling [40, 41] and decarboxylative coupling [42]. However, the Ullmann coupling reaction is recognized as one of the most successful and versatile strategies to synthesize tailored covalently bonded nanostructures [43, 44]. By Ullmann coupling is possible to control the sequences of the reaction step-by-step by functionalizing the precursor with halogen atoms.

Following this approach, Ammon *et al.* [45] explored the growth of porous carbon nanoribbons on Ag(111) surface using 1,3,5-tris(3-bromophenyl)benzene. The molecular precursors are deposited at room temperature (RT) as a building blocks on the surface and form a 2D self-assembled network stabilized by halogen-bonded. After the dehalogenation process, takes place the metal-carbon coordination of chains. Thermal annealing promotes covalent bonding, producing well-ordered nanoporous chains. The last step of the synthesis involves the dehydrogenation of the chains, bringing up the formation of porous carbon nanoribbons. Also, via the Ullmann coupling reaction, porous N-GNRs with a band gap of about 2.2 eV are fabricated on Ag(111) [46]. Similarly, Basagni *et al.*[47] synthesized organic semiconducting wires using three similar brominated molecular precursors doping with a different number of N atoms on the Au(788) vicinal surface. The wires grew along the terrace with (111) plane orientation, and their periodicity matches the Au three times lattice parameter. From the direct measurement of the local density of states, they found a similar bandbag for N-doped and undoped wires of 3.3 ± 0.2 eV.

Moreover, functional porphyrins-based 2D metal-organic framework (MOFs) offer an exciting platform for new devices with magnetic and optical controllable properties

[48, 49]. The motivation for choosing porphyrins as building blocks is based on their morphological and rich electronic properties, as well as high chemical versatility and robustness [50–52]. Focusing on these structures, different systems have been studied. For instance, porphyrins functionalized with biphenylene–cyano (2H–TPCN) and phenylene–pyridyl substituents (2H–TPyPP) were used to explore the synthesis of porous metal-organic coordination networks on Ag(111) by adatoms ligands. Lin *et al.* [53] showed the synthesis of rhombus and Kagome organometallic networks with large pores via pyridyl-Fe-terpyridyl coordination of terpyridyl ligand and pyridyl-functionalized porphyrin. Typically, MOFs with hexagonal symmetry have been synthesized, exhibiting electronic structures similar to graphene. Therefore, exploring non-hexagonal lattice geometries, which would lead to new electronic structures, is desirable. For instance, Li *et al.* [54] by first principle calculations found that metal phthalocyanine-based 2D MOFs coordinated by Ni^{+2} in a square lattice exhibit rich structural and magnetic behavior.

In this thesis, we present the systematic investigation of the synthesis of carbon nanostructures and doped graphene via bottom-up methods, using a comprehensive multi-technique approach. Scanning tunneling microscopy/spectroscopy (STM/STS) are employed to explore the morphology of the sample during the hierarchy synthesis and their local electronic properties, while X-ray photoelectron spectroscopy (XPS) probed the chemical state of the sample. Density functional theory (DFT) calculations support our experimental results.

For a broader investigation on the electronic and structural impact of the functionalization of graphene sheets with heteroatoms as well as on C-based analogue materials, for instance, porous networks, we have investigated two classes of model systems:

- The synthesis of non segregating h-BN doped graphene from a novel single molecular precursor via CVD, and explore its morphological, chemical, and electronic properties.
- The on-surface synthesis of new carbon-based molecular pore networks and pore N-doped GNRs.

This manuscript contains the following chapters:

Chapter 1 is the present introduction. In Chapter 2, we present a general description of Gr's structure and electronic properties, together with an overview of fundamental bottom-up approaches. Chapter 3 introduces the experimental techniques employed in this thesis and the experimental setup. Chapter 4 presents results on the growth of h-BN doped Gr. Chapter 5 contains the results of the investigation of the hierarchical growth of the porphyrin-based pore network. In chapter 6 we describe and compare the synthesis of pore N-doped GNRs on two different substrates. Furthermore, in Chapter 7 we will give the general conclusion and perspective of this work.

Chapter 2

Synthesis of functionalized graphene and carbon pores networks by bottom up methods

2.1 Graphene electronic structure

The carbon (C) atom has four electrons and the electronic configuration of its ground state is $1s^2 2s^2 2p^2$, i.e. two strongly bound electrons occupy the $1s$ orbital, two electrons are paired and occupy the $2s$ atomic orbital, and the remaining two unpaired electrons occupy different $2p$ ($2p_x$, $2p_y$, and $2p_z$) orbitals, such as shown in figure 2.1a. Moreover, the excited state of the C, for instance due to the presence of another C atom, could be described as the electron jumps from the $2s$ to the $2p$ orbital (see figure 2.1b). Despite the higher energy cost in promoting an electron from the $2s$ to the $2p$ level, this event is favorable since to the energy compensation induces by the hybridization of the orbitals, which leads to the covalent bonding.

Therefore, four quantum states are available for the excited state to perform covalent bonds. The overlap of $2s$ and $2p$ states produces an sp^n hybridization. In the case of

Gr, basically, the $2s$ state and two components of $2p$ state, for instance, $2p_x$ and $2p_y$, are mixed to create a hybridized sp^2 bonding orbital (see figure 2.1c), these three isoenergetic orbitals are pointing outwards in a plane, forming angles of 120° and bonding adjacent carbon atoms. The fourth orbital called π orbital, $2p_z$ is unchanged, projecting above and below the plane where the sp^2 hybrid atomic orbitals were located. If two sp^2 carbon atoms are close enough, they form a strong σ bond by overlapping the $sp^2 - sp^2$ hybrid atomic orbitals, such as it is represented in figure 2.1d. Moreover, the π orbital combined with adjacent π orbitals generate a huge orbital which allows easy movement of electrons across the plane.

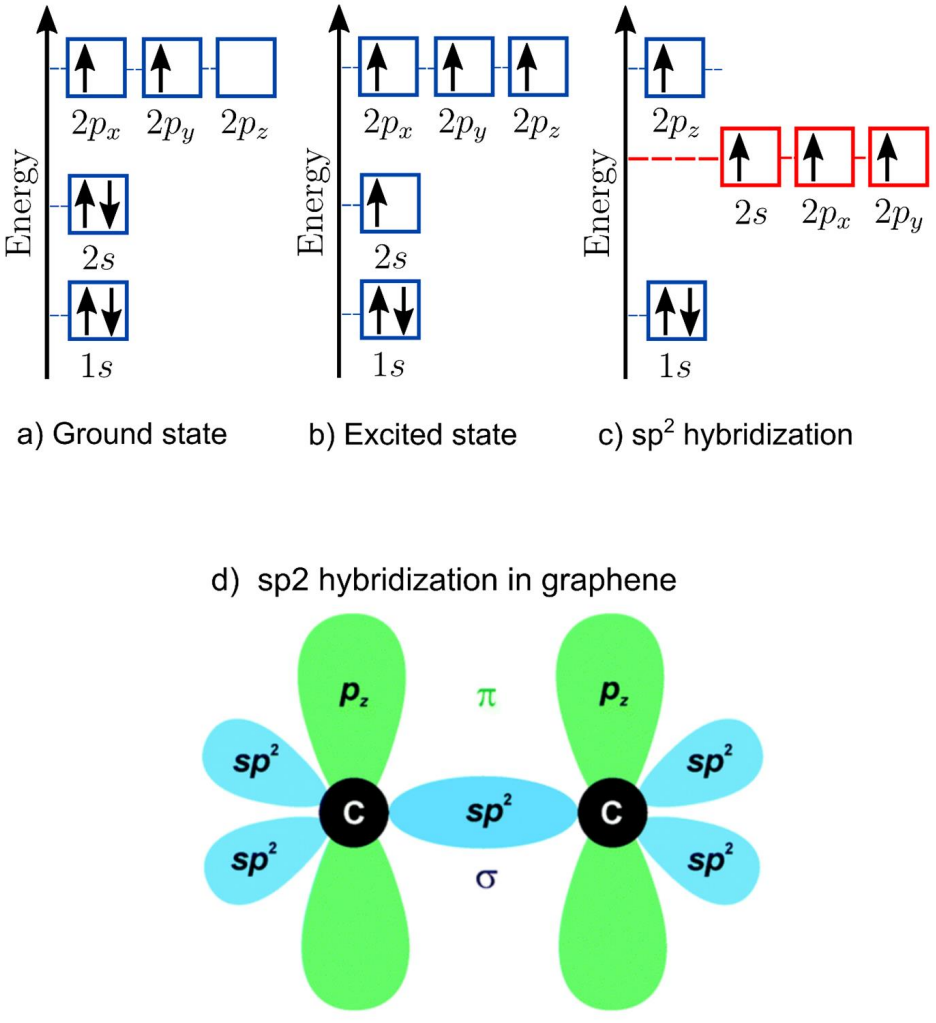

Figure 2.1: Schematic representation of the electronic configuration of carbon atoms for (a) ground state, (b) excited state, and (c) sp^2 hybridization together with (d) the atomic orbitals for two C atoms, observing the in-plane sp^2-orbitals form the -bonds leaving free p_z orbital perpendicular to the plane. The Gr honeycomb lattice is formed by 3 sp^2-bonded C atoms. Adapted from [55]

The honeycomb structure of Gr can be described as two hexagonal sublattices A and B with two atoms per unit cell, as observed in figure 2.2. The lattice is described by the primitive vectors a_1 and a_2 as follows:

$$\vec{a_1} = \frac{a}{2}(3, \sqrt{3}) \qquad \vec{a_2} = \frac{a}{2}(3, -\sqrt{3}), \tag{2.1}$$

where a corresponds to the distance between two carbon atoms and is $a = 0.142nm$. On the other hand, the high symmetry points in the first Brillouin zone can be defined as Γ, K, M, and K'. Moreover, the reciprocal vectors are given by:

$$a_1^\star = \frac{2\pi}{3a}(1, \sqrt{3}) \qquad a_2^\star = \frac{2\pi}{3a}(1, -\sqrt{3}) \tag{2.2}$$

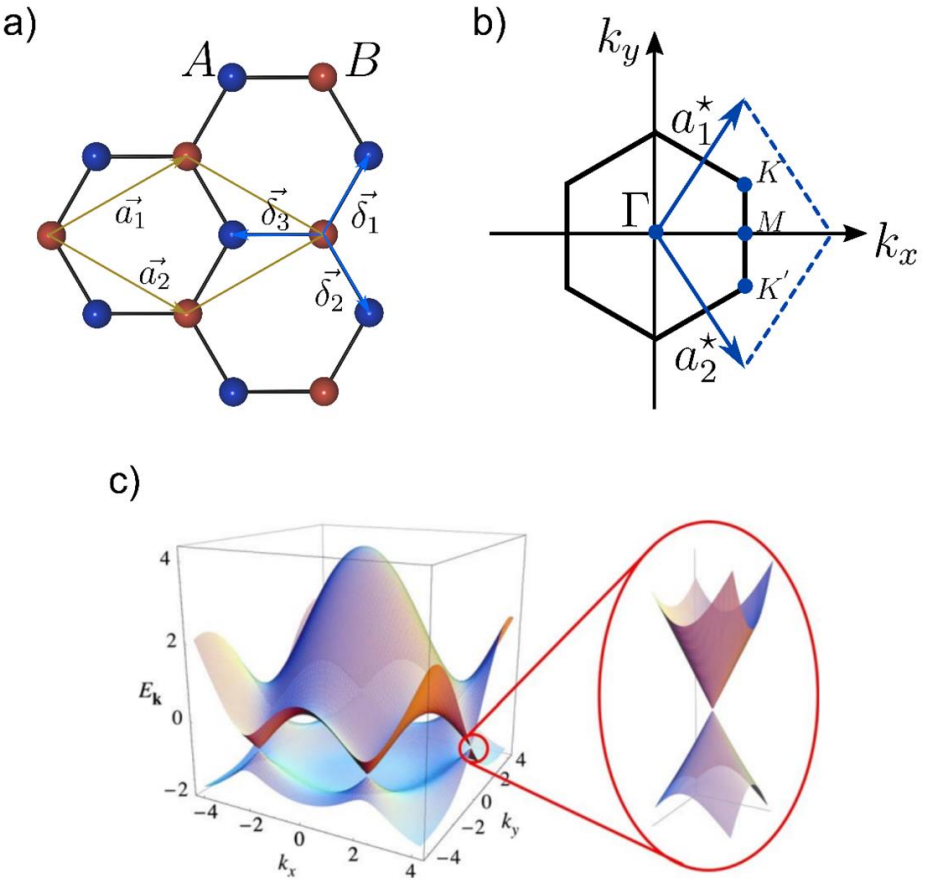

Figure 2.2: (a) Lattice Gr structure, the primitive vectors (yellow), and the first near-neighbor vectors (blue) are shown. The carbon atoms of sublattices A and B are colored blue and red, respectively. The lattice parameter is about $|\vec{a_1}| = |\vec{a_1}| = 0.25$ nm. (b) First Brillouin zone of Gr in the reciprocal lattice, the high symmetry points are indicated. (c) The electronic band structure is determined by an orthogonal tight-binding model considering just nearest neighbor atom interactions. The Dirac cone near the Fermi energy is highlighted in the figure, where it is observed the linear relation between energy and momentum for the bands. Taken and adapted from [3]

The tight-binding model is appropriate for studying the electronic structure of Gr. The theoretical model's key is finding an optimal representation for a base of pre-defined orbitals localized at atomic positions [56]. In the Gr lattice, each carbon atom could be described just by its delocalized π-electron; this is by a single $2p_z$ orbital. The other electrons are not considered for the calculations because the covalent bonds have filled the valence band (in the plane). The $2p_z$ orbitals are described by the wave function ϕ_p, which are eigenfunctions of the Hamiltonian H_s for a single isolated atom with eigenvalues ε_p, such as follow

$$H_s \mid \phi_p\rangle = \varepsilon_p \mid \phi_p\rangle \qquad \text{with} \qquad \langle\phi_p \mid \phi_p\rangle = 1 \tag{2.3}$$

The wave function of the system could be defined as a linear combination of Bloch wave function of two non-equivalent atoms in the sublattices A and B, such as

$$\psi^{\mathbf{k}}(\mathbf{r}) = a^{\mathbf{k}}\phi_A^{\mathbf{k}}(\mathbf{r}) + b^{\mathbf{k}}\phi_B^{\mathbf{k}}(\mathbf{r}) \tag{2.4}$$

where $\mathbf{k}$ is the wave vector of the electron. This wave function is a solution of the Hamiltonian of system, which is defined as

$$H^{\mathbf{k}} = H_s + V \tag{2.5}$$

where V represents the electrostatic potential due to ion cores on adjacent atomic sites.

$$H^{\mathbf{k}} = \begin{pmatrix} \langle\phi_A^{\mathbf{k}} \mid H \mid \phi_A^{\mathbf{k}}\rangle & \langle\phi_A^{\mathbf{k}} \mid H \mid \phi_B^{\mathbf{k}}\rangle \\ \langle\phi_B^{\mathbf{k}} \mid H \mid \phi_A^{\mathbf{k}}\rangle & \langle\phi_B^{\mathbf{k}} \mid H \mid \phi_B^{\mathbf{k}}\rangle \end{pmatrix} \tag{2.6}$$

To obtain the energy eigenstates of the hamiltonian of the system, in the tight binding context, some approximations are assumed: *(*1) the crystal field integral is neglected, *(*2) it was just considering the interaction between nearest neighbors; therefore, hopping integral t terms are non-zero only for these first neighbors, and *(*3) the p orbitals on different sites do not overlap.

Since atoms in sublattices A and B are chemically identical, the diagonal elements of the Hamiltonian matrix are equal $\varepsilon_p = \varepsilon_A^k = \varepsilon_B^k$, which correspond to the energy of the p_z orbital in an isolated atom. If we consider the three nearest-neighbor vectors in real

space shown in figure 2.2a and defined as

$$\vec{\delta_1} = \frac{a}{2}\left(1, \sqrt{3}\right) \qquad \vec{\delta_2} = \frac{a}{2}\left(1, -\sqrt{3}\right) \qquad \vec{\delta_3} = a\left(-1, 0\right) \tag{2.7}$$

the hopping integral Δ takes the followed form:

$$\Delta = -t\left[\exp\left(i\frac{k_y a}{\sqrt{3}}\right) + 2\exp\left(i\frac{k_y a}{2\sqrt{3}}\right)\cos\left(\frac{k_x a}{2}\right)\right] \tag{2.8}$$

In this way, it is possible to solve the matrix Hamiltonian and obtain the electronic band structure of the Gr:

$$E_{\pm}(\mathbf{k}) = \varepsilon_p \pm t\sqrt{1 + 4\cos^2\left(\frac{\sqrt{3}k_y a}{2}\right) + 4\cos\left(\frac{\sqrt{3}k_y a}{2}\right)\cos\left(\frac{\sqrt{3}k_x a}{2}\right)} \tag{2.9}$$

where E_+ correspond to anti-bonding π band and E_- describe the the bonding π band. This result describes the dispersion relation of the Gr near the K (or K') point in the first Brillouin zone, shown in figure 2.2c and known as Dirac cone, where the linear behavior of electronic bands near the Fermi level is noticed. At K point, the two bands touch; this point coincides with the Fermi energy of Gr and allows us to define it as a zero band gap semi-metal.

2.2 Graphene gap opening approaches

2.2.1 Graphene functionalized by chemical vapor deposition (CVD)

Substitutional doping of Gr with different atoms induces the disruption of the sp^2 hybridization of the carbon atoms. Depending on the doping configuration within the Gr sub-lattices, locally significant changes in their electronic properties and chemical reactivity could be promoted.

One of the most efficient methods for doping Gr is chemical vapor deposition (CVD) on catalytic metal surfaces. This method has been widely used for synthesizing large-area and high-quality Gr. On surfaces with low solubility of C atoms, such as Cu(111)

and Ir(111), the growth mechanism started through the adsorption of the precursor on the substrate. After that, the process involves the decomposition of molecules, the permanence of a certain type of atom on the surface, and the release of another as a product of the reaction. In figure 2.3, the synthesis of Gr from methane on Cu(111) is illustrated. In this example, the hydrocarbon precursor is deposited onto a preheated surface. Dissociated carbon fragments CH_x ($x = 0$–3) diffuse quickly due to the low diffusion barrier of C atoms on Cu(111), and Gr nucleation happens. Nucleation generally occurs at grain boundaries, defects, crystalline edges, and other high-energy sites. Therefore, individual Gr islands grow, CH_x radicals attached to the Gr edges dehydrogenated, followed by the coalescing of the growing Gr domains [57–59].

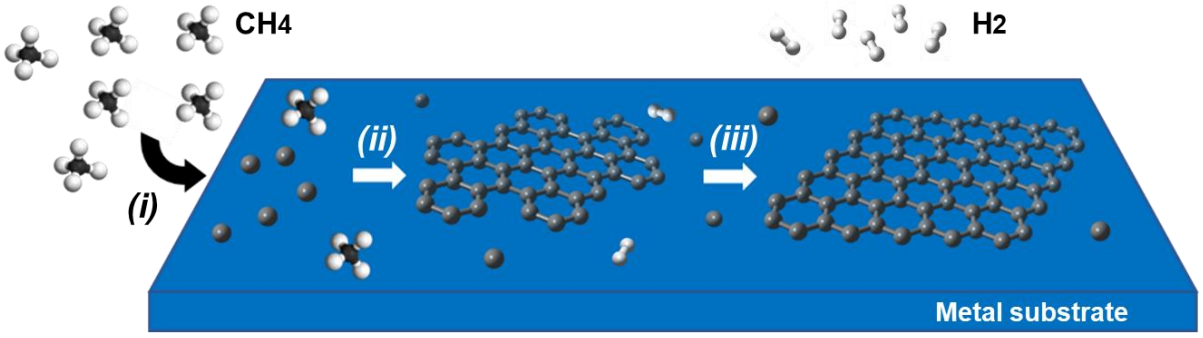

Figure 2.3: Schematic representation of Gr growth by CVD on a low solubility Carbon surface from methane (CH_4), showing the synthesis steps: (i) deposition and catalytic decomposition, (ii) Surface diffusion, and first nucleation, and (iii) Growth and expansion. Adapted from [58].

The substrate's catalytic activity and atomic structure play a determinant role in the synthesis, i. e., the type of sp^2 monolayer - substrate interaction and the difference between the lattice parameter of the two systems. For example, the almost perfect matching of the lattice constants between Gr and Ni(111) promotes the growth of a high-quality well-oriented monolayer with a (1×1) structure. Otherwise, when a system is formed by two periodic lattices, one on top of the other with a mismatched lattice constant or a relative twist, a new periodic pattern, in the range of nm, is formed and known as the Moire pattern. Hence, mismatch plays a fundamental role in the sp^2 monolayer epitaxy, depending on its value could induce compression or tension in the sp^2 layer.

For instance, monolayers of hexagonal boron nitride (h-BN) (see figure 2.6a), which is a 2D material formed by boron and nitrogen atoms covalently bonded in a hexagonal sp^2 lattice, have been grown on transition metal surfaces. From molecular precursor as

borazine, at high metal substrate temperature a single epitaxial monolayer is synthesized. On Rh(111) the lattice mismatch of -7.0% leads to a strongly corrugated structure as shown in figure 2.6b-c. The superstructure consists of 13 × 13 unit cells of h-BN on top of 12 × 12 unit cells of Rh(111) with an in-plane superlattice parameter of 3.22 nm.

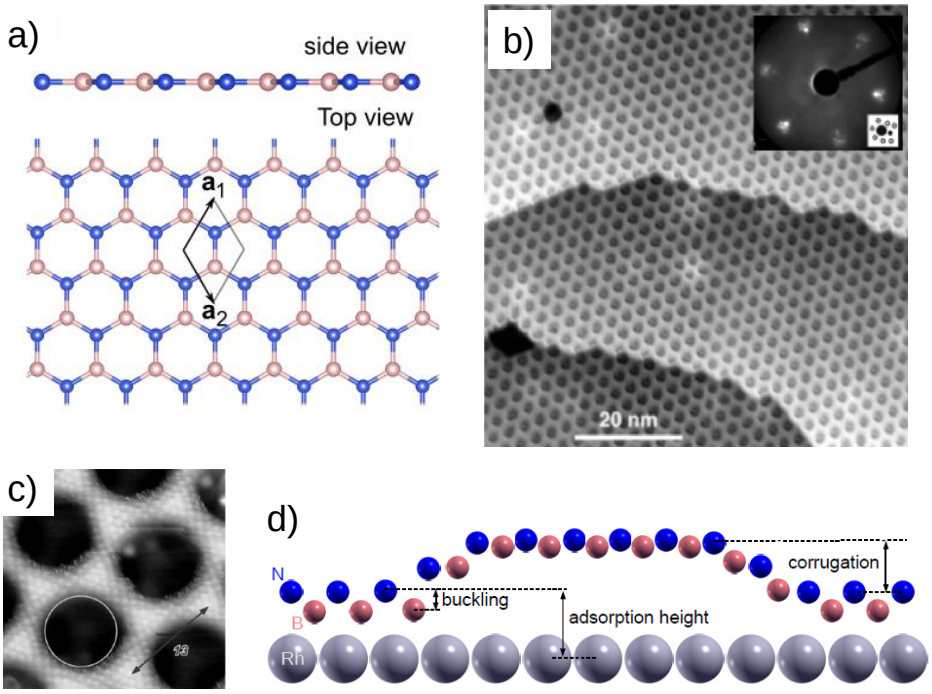

Figure 2.4: (a) Side view and top view of a single monolayer h-BN. Vectors $\mathbf{a}_1$ and $\mathbf{a}_2$ indicate the unit cell. (b) Large-scale STM image and LEED pattern (inset) of h-BN on Rh(111). Adapted from [60] (c) High resolution STM image. The bright regions are known as wires, in this sites the interaction with the substrate es weak. The dark regions are depressions in the continuous h-BN layer due to the strong interaction with the metal substrate, called as pores. Adapted from [61]. (d) Illustration of a vertical cut through the layer along the main diagonal of the supercell. Adapted from [62].

Substitutional doping on Graphene

Experimentally and theoretically efforts for incorporating nitrogen or boron atoms into Gr have been attempted by several groups in order to bring on the opening of a band gap and introduce additional n-type or p-type carriers in carbon systems, respectively. For instance, Usachov *et al.* [63] synthesized N-doped Gr on Ni(111) by CVD using s-triazine molecules. They reported a band gap opening of 0.2 eV and an n-type doping effect. Moreover, Lv *et al.* [8] reported the growth of N_2 Gr doping from methane (CH_4) and ammonia (NH_3) on Cu foil. STS measurements show the presence of localized states in the conduction band. On the other hand, Cattelan *et al.* [64] produced boron-doped Gr with a relatively small number of structural defects by catalytically breaking a carbon-rich precursor (CH_4) mixed with diborane (B_2H_6) on the surface of

the Cu(111). ARPES (angle-resolved photoemission spectroscopy) measurements showed p-type doping of ~ 0.3 eV. From the XPS and RAMAN data, it was possible to verify a B concentration in Gr of $\sim 2.5\%$, as well as the formation of boron carbide. A similar strategy was applied by Usachov *et al.*[9], who used the catalytic decomposition of the carborane precursor ($C_2B_{10}H_{12}$) in the CVD process on Ni(111) and Co(0001). Under these conditions, B-Gr with concentrations of up to 19% boron was obtained. For lower concentrations of B, the process can be controlled by introducing propylene (C_3H_6) together with diborane. In this case, doping shows a strong asymmetry between Gr sites, typically occurring more strongly at top sites. Compared to the previous case, the higher degree of doping and the type of site doped depend on the precursor, and the substrate strongly influences it. ARPES measurements indicate the Dirac cone for energies greater than 2 eV below the Fermi level, while the region between $0 - 2$ eV shows B-Gr states strongly hybridized with substrate states. In this case, the precursor-substrate combination allowed greater flexibility of the doping level but still showed certain randomness in the doped sites and, unfortunately strong hybridization of the electronic states of the material and the substrate.

The structural similarity between graphene and hexagonal boron nitrate (h-BN) with a lattice mismatch by about 2% [66, 67] motivates the growth and investigation of Gr doped with h-BN units. Considering that monolayer h-BN is an insulating material with a large band gap of about 6.8 eV [68] and Gr is a zero-band gap semi-metal, several studies have predicted a semiconductor behavior for ternary h-BNC structures, with a tunable band gap between 0 and ∼6.8 eV. Therefore, the synthesize this kind of materials represent a plethora of new areas of applications, for instances in nanoelectronics [20, 69] and nanophotonics devices [70], photocatalytic activity [71], gas adsorption [72], and supercapacitors [73].

Several experimental attempts have been carried out in order to synthesize h-BNC monolayers. Ci *et al.* [22] reported for the first time h-BNC hybrid structures, which consist of randomly distributed domains of h-BN and C phases. These are two segregated phases, as shown in figure 2.5a-b. In this growth, two molecular precursors were used simultaneously, methane and ammonia borane (NH_3–BH_3), and the atomic ratio of B, C, and N was tuned by controlling the experimental parameters, keeping B:N equal 1. The local density of states (LDOS) was explored, showing that h-BN domains induce

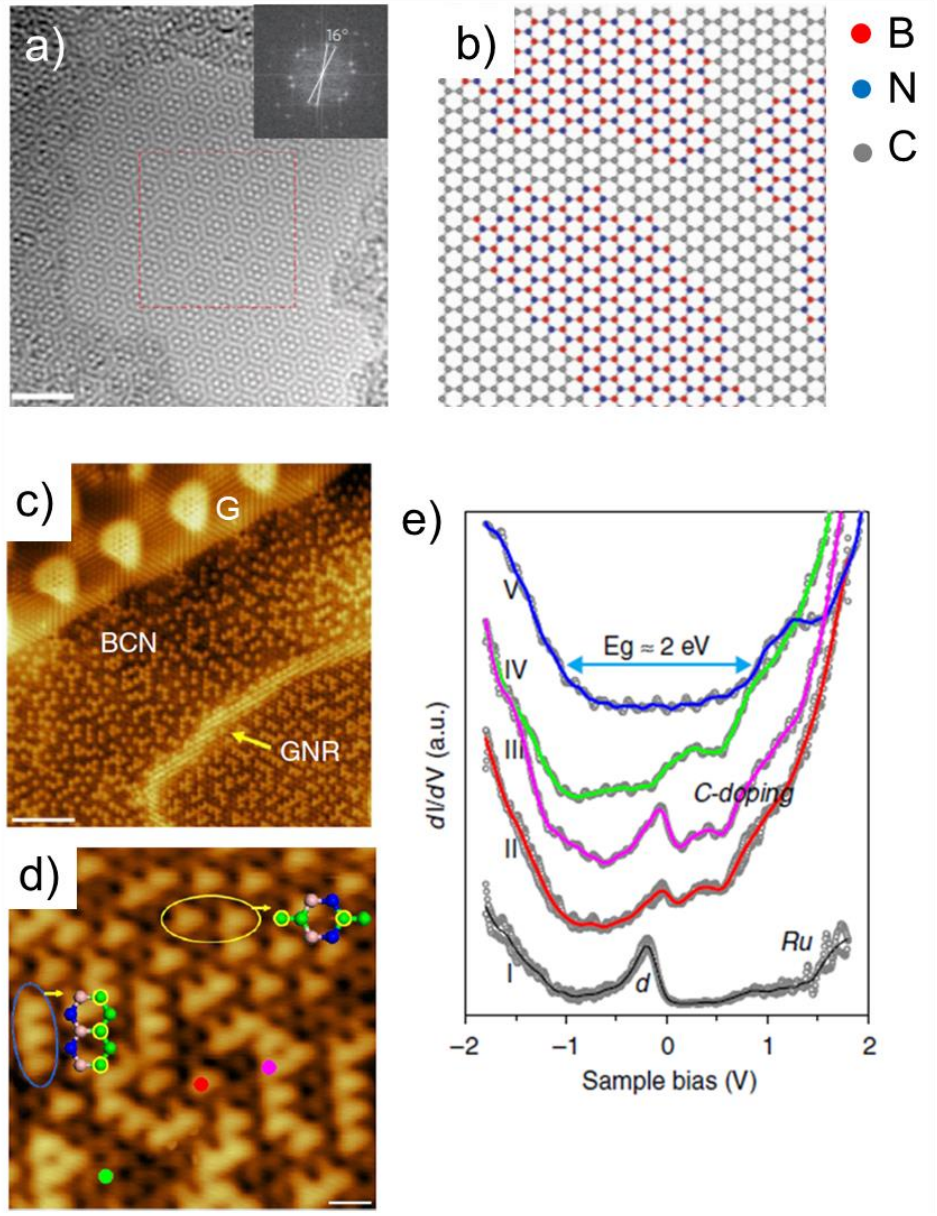

Figure 2.5: (a) Atomic structure of h-BNC film acquired by High-resolution transmission electron microscopy (HRTEM) together with its (b) atomic model highlighted the hybridization between h-BN and Gr domains. Adapted from [22]. (c)-(d) STM images of the lateral heterostructure formed by Gr, BNC, and some GNRs. (e) The dI/dV spectra on Ru (I), (II) bright spot, (III), bright clusters, (IV) dark region, and (V) decoupled BCN. Adapted from [65].

distortion in the zero Gr band gap. Alternatively, the sequential two-step growth method (Gr is grown on preexisting h-BN patches or vice versa) was employed [65, 74, 75] to synthesize lateral h-BN–Gr heterostructures with controlled domain sizes and the edge structures. Lu *et al.* [65] used this approach on Ru(0001) and found an alternative route for doping under non-equilibrium conditions, where the atomic exchange of C atoms by BN units or vice versa is moderate by the metallic substrate. They reported the synthesis of $h - BC_2N$ fuse GNRs (see figure 2.5c-d). In addition, after decoupling it from the

surface by oxygen intercalation, an energy gap of 2 eV was observed from the STS data, as shown in figure 2.5e.

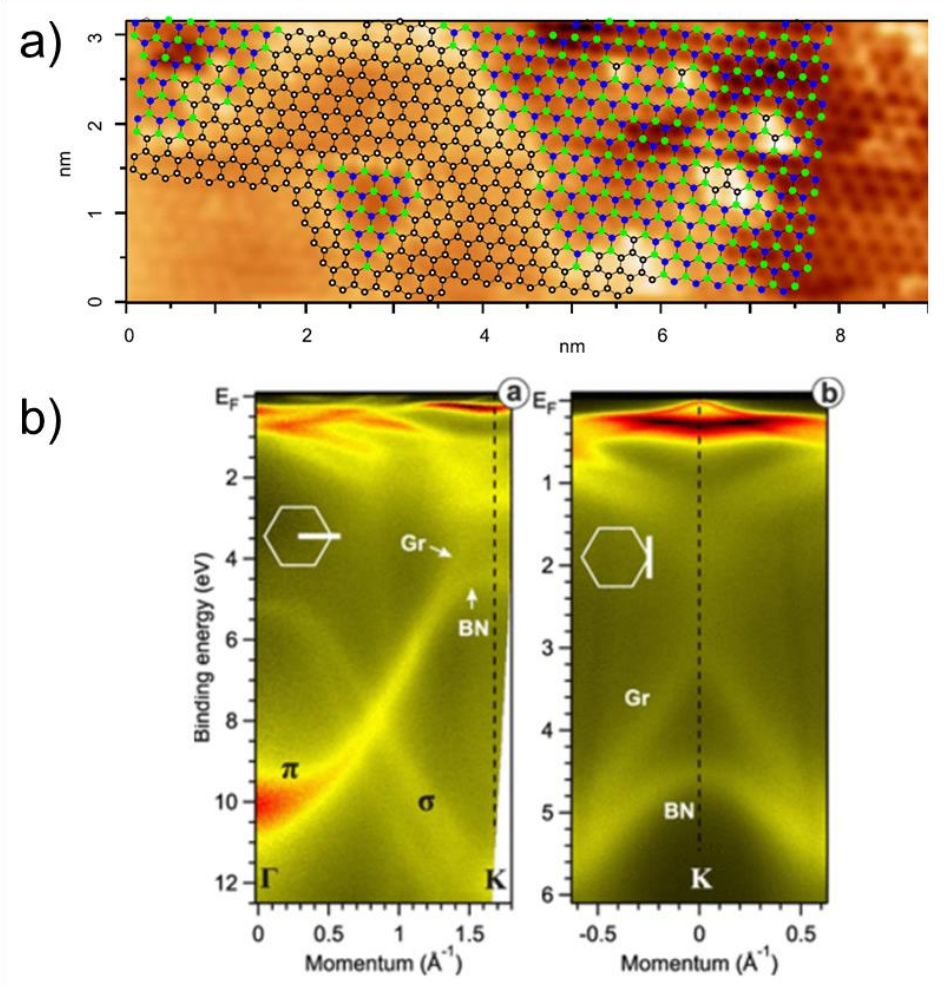

Figure 2.6: (a) h-BN–Gr lateral heterostructure on Co(0001) obtained from a single molecular precursor (1,3,5-trimethylborazine). (b) The Angle-resolved photoemission spectroscopy (ARPES) data clearly shows the π and σ h-BN and Gr bands. Adapted from [26]

In order to get more homogeneous h-BNC structures, growth using a single precursor containing C, B, and N atoms in the same molecule has been reported. For example, trimethylamine borane [25] and methylamine borane [24] on Cu foil, 1,3,5-trimethylborazine on Co(0001) [26] and dimethylamine borane on Pt(111) [23]. These studies reported that h-BN and Gr domains interconnected, forming h-BN–Gr lateral structures (see figure 2.6), which leads to a superposition of Gr and h-BN bands, such as it is shown in figure 2.6c. The formation of these segregate structures has been predicted by several theoretical studies [27–32] that found C–C and B–N bonds tend to be energetically more favorable than other bonds in a system composed of C, B and N atoms. In addition, Beniwal *et al.* [33] reported the synthesis of 2D hexagonal graphic

BCN monolayers using bis-BN cyclohexane on Ir(111), here they described the structure as a homogeneous ternary compound of BCN.

Despite enormous effort, experimental evidence of h-BNC formation is limited. This motivate us to continue exploring the synthesis of innovative material. For that purpose, we chose an unexplored precursor and two metallic subtracted Rh(111) and Ir(111).

2.2.2 Growth of GNRs via on surface synthesis (Ullmann reaction)

On-surface synthesis has received tremendous attention as an alternative to conventional synthesis methods, showing highly successful in building stable and atomic precision one-dimensional (1D) and two-dimensional (2D) nanostructures with tunable electronic, chemical, and magnetic properties. In this approach, from single building blocks carefully selected, chemical reactions confined to the single-crystal surfaces are stimulated under ultra-high vacuum (UHV) conditions[76, 77].

In simple words, the method could be described in three steps: (1) The deposition and adsorption on the surface of the molecular building block with connections and substituent units. (2) The activation process, which consist in removing the substituents and leaves free radicals in specific positions, and (3) the diffusion and connection of the active molecules, forming a nanostructure, as shown in figure 2.7.

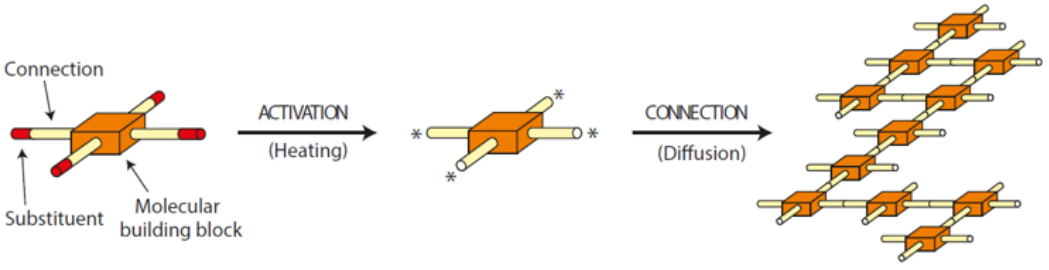

Figure 2.7: Schematic representation of on-surface synthesis approach. Adopted from [78].

In this way, the catalytic role of the surface in the synthesis process has to be in the spotlight. For example, the balance between adsorption energy and diffusion energy barrier is crucial. Ourdjini *et al.* [79] investigated the synthesis of a two-dimensional polymer via dehydration of 1,4-benzenediboronicacid (BDBA) molecules on Ag(111), Ag(100), Au(111), and Cu(111) substrates, they found that Ag(111) exhibits the best compromise between adsorption strength and mobility. Otherwise, on Cu(111),

molecules have less mobility which avoids the polymerization process. In contrast, on Au(111), the interaction between the molecules and the surfaces is too weak, leading to the molecular desorption before the synthesis occurs.

Ullmann coupling reaction

Many coupling reactions have been explored to achieve novel surface-assisted motifs, for instance direct C-H activation, alkyne coupling and decarboxylative coupling. However, the Ullmann coupling reaction is recognized as one of the most successful strategies to synthesize tailored covalently bonded nanostructures.

The Ullmann coupling scheme is based on the deposition of halogen custom designed molecular precursors on metal substrates. The cleavage of these carbon halogen bonds results in carbon radicals (surface-stabilized radicals - SSRs), which after surface diffusion could form metastable organometallic bonds or ultimately carbon-carbon (C-C) bonds. For the synthesis of biphenyls from a brominated precursor on Cu(111), the dehalogenation of monomers is followed by the formation of organometallic structures. This is, the SSRs are bonded to Cu adatoms (C-Cu-C). By the heating of the surface, the covalent coupling is promoted, and an organic structure is built.

In the Ullmann reaction, as expected, the molecular building blocks are usually functionalized with iodine, bromine, or both. On the other hand, chlorine and fluorine are less explored. This could be understood as a function of their dissociation energy, which is specific for each halogen atom and leads to different activation temperatures. For example, Blanksby S. and Ellison B. studied the bond dissociation energies of organic molecules. They found for $C_6H_5 - X$ with X=Br,I, Cl, and F, the following results: for iodine 280 kJ mol^1, bromine 351 kJ mol^1, chlorine 406 kJ mol^1 and fluorine 531 kJ mol^1. Another interesting aspect to consider is that the carbon-halogen bonding energy is lower compared to C-C bonds. Therefore the dehalogenases process can happen without destroying the molecular backbone.

Hence, different annealing temperatures are needed to cleavage the halogen substituents. The complete dissociation of bromine and iodine occurs on Cu(111) at RT. As a result, organometallic structures are already observed under this condition. On Ag(111) has been reported the partial debromination at RT. However, on Au(111), the bromine is split off just after thermal activation. These studies show the careful balance between

carbon-halogen and the surfaces.

For instance, Moreno *et al.* [80] explored the metallic catalytic surface effect from a single molecular brominate precursor, finding very distinct polymers. On Au(111), after the Ullman coupling and cyclodehydrogenation, well-defined GNRs were obtained. On this substrate, it is not reported organometallic intermediates species. In the case of Ag(111), the dehalogenation and dehydrogenation process take place at 150C, and the covalent C-C bond is inhibited, which leads just the growth of organometallic chains. On a more reactive surface like Ag(100), metal-coordinated chains are already formed at RT. This last result also shows the dependence on the orientation of the crystal. Finally, on Cu(111) was not observed a ordered polymerization, in fact the formation of organometallic intermediate structures blocks the Ullmann C-C coupling.

Therefore, molecule-substrate interactions and direct molecule–molecule bonds determine the hierarchy of reaction steps and their thermal activation energies. Some of the factor involved are: the design, adsorption energy, and diffusion of the precursor, as well as the reactivity, reconstructions, and adatoms availability of the surface. Moreover, it is possible to promote new reaction pathways through thermal stimuli, which represent a promising strategy in the on-surface synthesis context and it is explored in this thesis.

Figure 2.8 illustrates the subsequent surface-assisted synthesis steps followed to grow GNRs via the Ullmann coupling reaction. In this example, Au(111) is the substrate, and a brominated molecule is used as a precursor. Here, the monomers are deposited, keeping the surface at T_0. Then, the sample temperature is increased to T_1, inducing the monomer dehalogenation and T_2 for the polymerization of the activated precursors. GNRs are formed at T_3 when the cyclodehydrogenation is activated.

2.2.3 Synthesis of carbon pore networks from porphyrins molecular precursors

Figure 2.9a illustrates the basic planar structure of the porphyrin macrocycle, together with the International Union of Pure and Applied Chemistry (IUPAC) numeric ring system. The basic structure of the macrocycle consists of four pyrroles rings joined by four methine groups ($= CH-$). The porphyrin skeleton has twenty carbon atoms with two iminic ($= N-$) and two aminic (NH) nitrogen atoms forming part of the pyrrolic

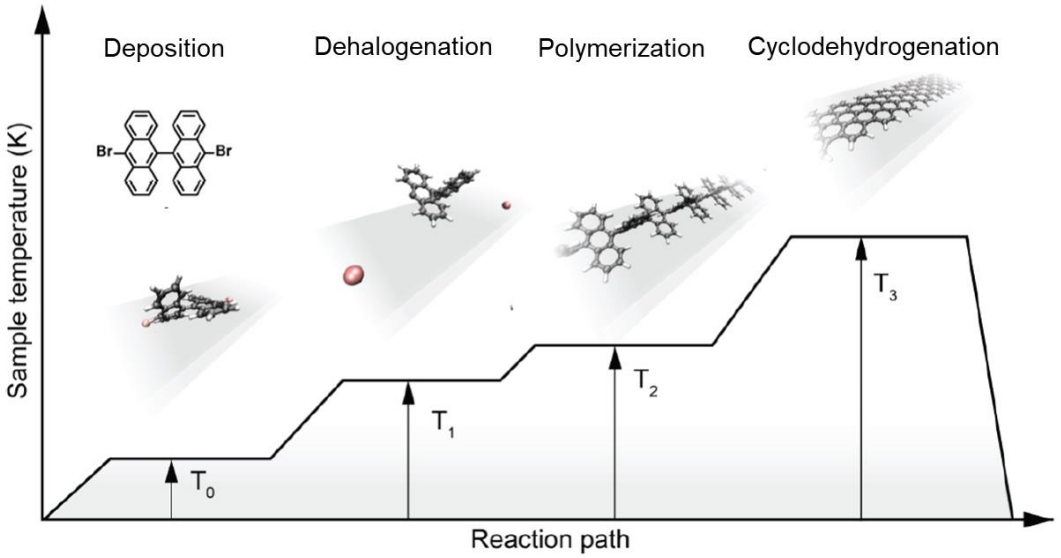

Figure 2.8: Synthesis of GNRs on Au(111) from deposit a halogen-substituted precursor keeping the substrate at T_0. The activation of the precursor is promoted at T_1, followed by the polymerization at T_2. GNRs are finally obtained at T_3, temperature for the cyclodehydrogenation. Adapted from Backes *et al* 2020 2D Mater. 7 022001

groups. According to the nomenclature present in figure 2.9a, α positions, next to N atoms are labeled as 1, 4, 6, 9, 11, 14, 16 and 19 , β positions, in front to the N atoms are labeled as 2, 3, 7, 8, 12, 13, 17 and 18, and *meso*-carbon, labeled as 5,10,15 and 20, this is in the bridging methane. Moreover, porphyrins are aromatic compounds with 18 delocalized π-electrons. These carbon-nitrogen macrocycles play fundamental roles in many biological process, such as photosynthesis [81], respiration and metabolism[82].

The conformation, electronic, optical and magnetic properties of the molecule can be tuning by chemical substitutions over the macrocycle. The central hole of the porphyrins macrocycle can host different metals ions (M^{n+}), for instances Co, Ni, Cu, Fe and so on. The coordination of the metal ion M is stabilized by the bonds with the four nitrogen atoms within the macrocycle and leads to the formation of metalloporphyrin, as is illustrate in figure 2.9b. Moreover, the tetrapyrrole macrocycle can be functionalized by a wide variety of terminal moieties, for instance with four phenyl groups bound to the carbon bridge between adjacent pyrrole groups. This kind the molecule is known as tetraphenylporphyrin (TPP). If the macrocycle is not functionalized, the molecule is called as free-base porphyrins, such as one can observe in figure 2.9c.

Tetrapyrroles have shown great potential as highly appropriate building blocks, thanks to their morphological and rich electronic properties, high chemical versatility, and

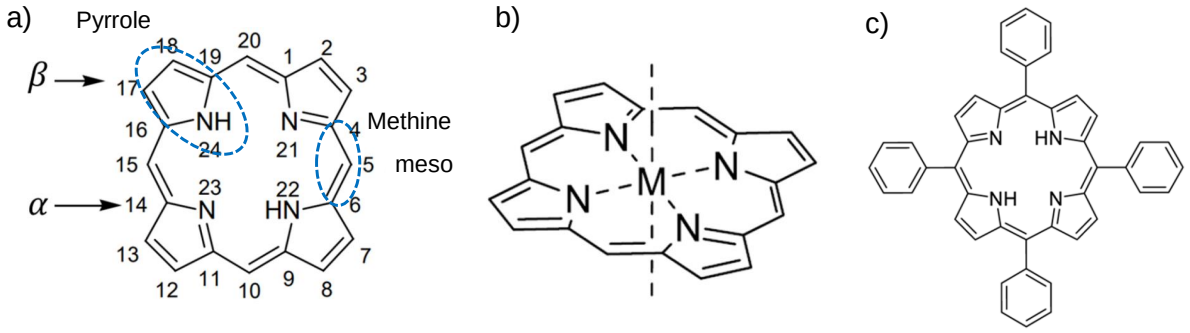

Figure 2.9: a) Structure of the porphyry's macrocycle forming by four pyrroles connected by a methine carbon. The actual IUPAC numeric system is also shown. b) Nitrogen atoms within the macrocycle cavity allow the conformation of stable complexes with metal ions, M. This is the metalloporphyrin cycle. c) 5,10,15,20-tetraphenylporphyrin (TPP), where each methine is connected to a phenyl.

robustness [50–52]. In particular, porphyrins have received much attention due to their potential applications in catalysis [83], molecular electronics such as organic light-emitting diodes [84], and field-effect transistors [85, 86].

TPP derivates have been investigated on different metallic surfaces. In most cases, the molecules exhibit a specific adsorption geometry called saddle-shape conformation. Figure 2.10a-b shows the optimized geometry reported by Lepper *et al.* [87]. In this conformation, the overall orientation of the porphyrin macrocycle can be described as parallel to the surface. The molecule-substrate interaction is considered the van der Waals type.

On the other hand, on Cu(111), STM data acquired at RT have shown a peculiar adsorption features as displayed in figure 2.10c-d. In this conformation, two opposing pyrrole rings undergo a drastic rotation and the iminic nitrogens point towards the bridge positions.

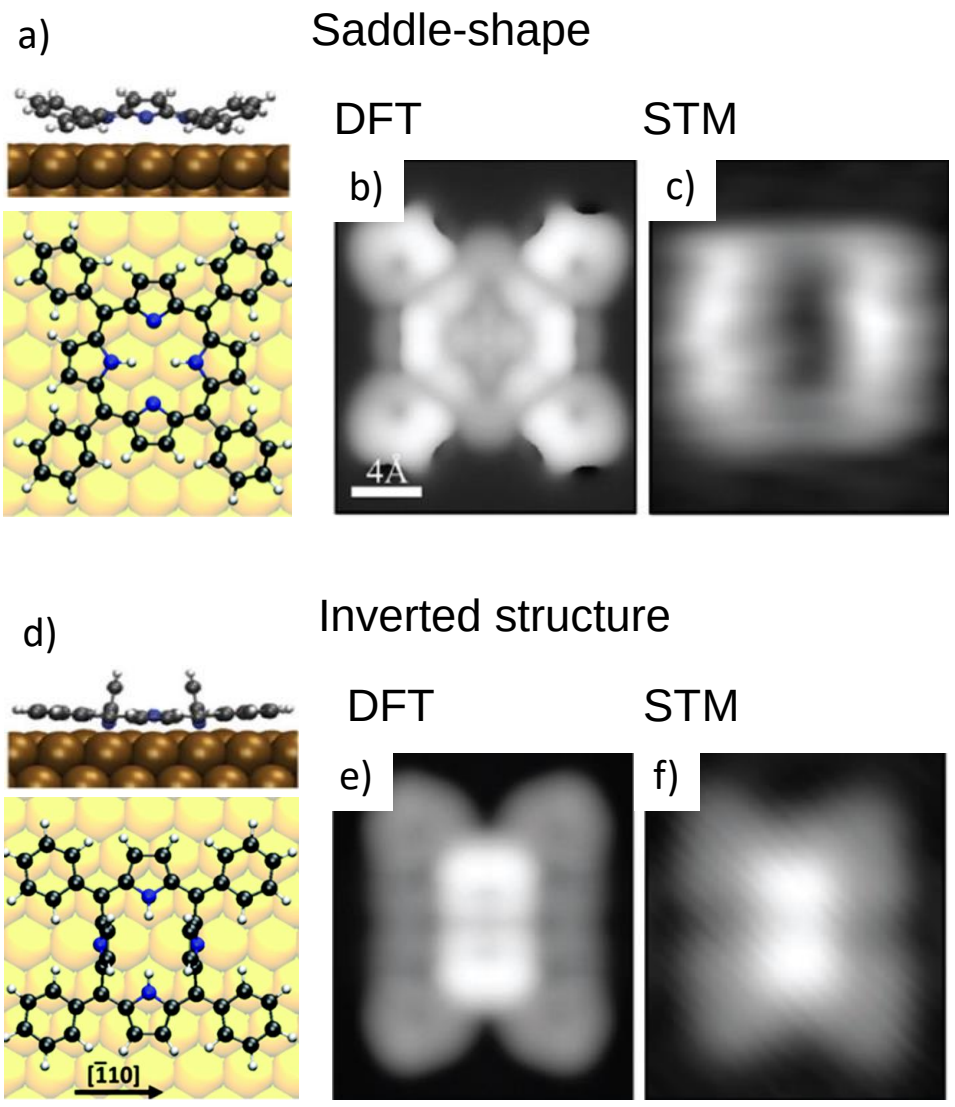

Figure 2.10: Molecular conformation of TPP on Cu(111) surface. (a) side and top view of the atomic model for saddle-shape molecular conformation. (b) DFT and (c) STM images of a molecule in saddle-shape conformation. (d) side and top view of the atomic model for the inverted molecular conformation. (e) DFT and (f) STM images of a molecule in inverted structure. Adapted from [87].

Chapter 3

Experimental methods

3.1 X-ray photoemission spectroscoy

X-ray photoelectron spectroscopy (XPS), also known as electron spectroscopy for chemical analysis (ESCA), is a powerful surface-sensitive experimental tool to investigate elemental composition, the chemical and electronic state of the atoms on the surface sample. This technique is based on the photoelectric effect first observed by H. R. Hertz in 1887 and later explained by A. Einstein in 1905. XPS spectrum is obtained by irradiating the sample using an X-ray beam resulting in the photoemission of its electrons. A photoelectron spectrum is acquired by counting ejected electrons as a function of their kinetic energies. The energies, intensities and shape of the photoelectron peaks allow identification and quantification of almost surface elements.

3.1.1 Photoemission process and fundaments

In 1887, Frank Hertz noticed that an electrical discharge between two electrodes subjected to high voltage occurs more readily when ultraviolet light incidents one of them. In 1905 Albert Einstein explained this phenomenon based on Planck's quantization of

energy concept. In simple words, incident photons directly transferred their energy to electrons within the atom, causing the emission of these electrons without energy loss, as can see in the photoelectric effect theory proposed by Einstein:

$$\epsilon_{max} = h\nu - \phi, \tag{3.1}$$

where ϵ_{max} is the kinetic energy of emitted electron coming from the Fermi level of the sample, $h\nu$ is the energy of the incident radiation, being h the Planck's constant and ν the frequency of the radiation, and ϕ the work function of the metallic surface, which is defined as the minimum energy required to remove an electron from the Fermi level to the vacuum level and it considered as a consequence of translational symmetry breaking at the solid boundary. For his work on the photoelectric effect, Albert Einstein was awarded the Nobel Prize in Physics in 1921.

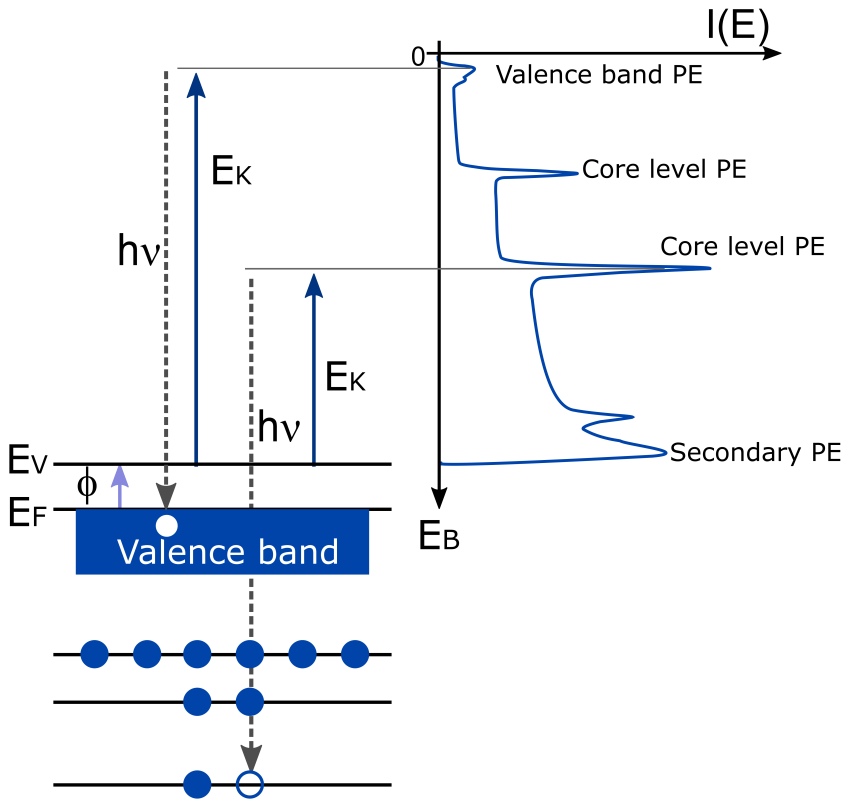

Figure 3.1: Illustration of the photoemission process on a metal sample. The correspondence between the density of occupied states on the surface and the photoemission spectrum is shown. The elastic photoelectron peaks are superposed on the continuous background of inelastic secondary electrons. Such as is shown in the diagram, the binding energy is measured with respect to the Fermi level and the kinetic energy of the photoelectrons with respect to the vacuum level.

In 1957, Kai Siegbahn in Uppsala University developed the instrumentation and theory of

Electron spectroscopy for chemical analysis (ESCA) technique, currently known as X-ray photoelectron spectroscopy (XPS). In recognition of his contributions to experimental physics, K. Siegbahn received the Nobel Prize in 1981. Such as its name suggests, in the case of XPS, the energy of the incident photon is in the soft X-ray region, which could be defined between 200.0 ev and 2.0 keV. Figure 3.1 illustrates how the photoemission spectrum reflects the distribution of energy levels occupied by electrons within the solid. Similar to the photoelectric effect equation, in the photoemission process, an electron located at a certain core level within the solid is emitted into the vacuum by the complete absorption of a quanta of energy h from the incident photon:

$$E_k = h\nu - E_B - \phi, \tag{3.2}$$

where E_k is the kinetic energy of the emitted photoelectron, E_B is the electron's binding energy within the solid, and ϕ is the work function.

The photoemission spectrum shows the intensity or number of photoelectrons detected as a function of the kinetic energy (or binding energy). The intensity and shape of the spectra are defined by the photoemission cross-section, σ, which is different for each electron level and depends on the exciting radiation. In the case of x-ray photons, photoelectrons coming from the core levels formed sharp peaks located at specific binding energies, which are characteristic of atomic species, giving information on the elemental composition of the surface samples. Besides elastic events, photoelectrons undergo inelastic scattering that reduces their kinetic energy. If the loss energy is a quantized amount, these electrons form features called satellites, for instance, shake-up and multiplet splitting [88], and could use them in the chemical analysis.

On the other hand, photoelectrons undergoing multiple inelastic collisions make up the inelastic background observed as a step function of the side with the lower kinetic energy for each elastic peak. The background is continuous because the energy loss is multiple random processes. Figure 3.1 represents the typical signal related to the valence band, which is a broad and weak feature in the spectrum due to a low photoelectric cross-section at XPS photon energies. Such as is spotlight in [89] photoemission has a maximum probability at photon energies close to the threshold and drops off rapidly when the photon energy exceeds the electron binding energy sufficiently. Consequently, XPS is a tool to probe mainly deep core levels.

Even though the electrons probed with XPS do not participate directly in the chemical bonding, the core levels' binding energy varies depending on the atom's chemical environment. In simple words, if there is a change in the spatial distribution of the electronic charge of the valence levels of an atom due to the formation of a chemical bond, whether ionic or covalent, the electrons of the internal levels perceive the distortion of the chemical environment, which is reflected as a change in the bond energy, known as chemical shift ΔE_B, that is, the difference in energy between two different chemical forms of the same atom. By means of chemical shifting, information is obtained about bond types, oxidation states, and other data about the chemistry of the atoms in the material. Weak interactions between atoms, such as hydrogen bonding, do not alter the electron distribution enough to change the binding energy [90, 91].

Moreover of the photoelectron peaks, the XPS spectrum shows up additional peaks related to Auger electrons, which are emitted by the relaxation process of the excited ions left over from photoemission. In this process, the vacancy created in the atom can be neutralized through a transition of an outermost electron towards the vacancy. This represents the relaxation process of the atom. Since the transition is from a less bound level, an excess of energy equal to the difference between the levels involved is remains in the system. This energy can be released by expelling a second electron known as an Auger electron. In contrast to the photoelectron, the kinetic energy of the Auger electron is independent of the frequency of the exciting photon and is only a function of the energy of the three levels involved in the process [92]. Another relaxation process, which competes with the emission of Auger electrons, is the X-ray photon emission by fluorescence. According to Hercules *et al.* [93] for low energy processes of 1 keV, the Auger effect is predominant as a relaxation mechanism, whereas for high energies such as 10 keV, the emission of X-rays is more likely to occur. Moreover, X-ray emission is a minority process for light chemical elements ($Z > 30$).

Such as was mentioned before, XPS is a surface analysis. Although x-rays have a high penetrating power of approximately $1\mu m$, without appreciable attenuation, and photoionize electrons from the bulk atoms, the information obtained by the technique corresponds to a few layers of atoms in the surface region of the solid. This is because photoelectrons have a high probability of losing energy, since they are highly interacting particles with the solid (they can lose energy when interacting with phonons, plasmons

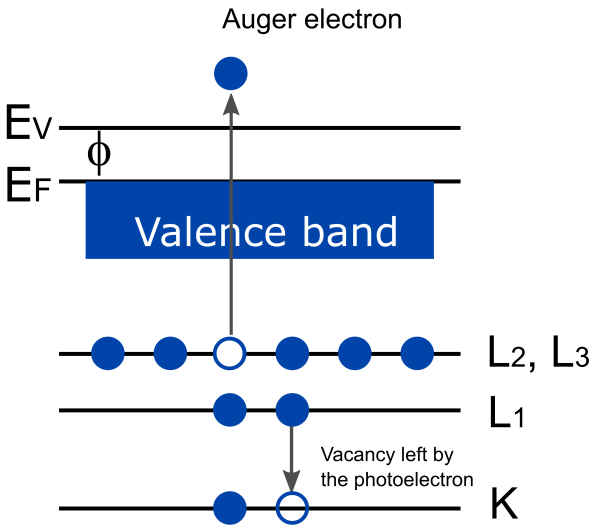

Figure 3.2: Illustration of the secondary electron emission (Auger electron), in this case, KL_1L23.

or electrons), therefore they are the electrons of the outermost layers of atoms those that manage to get out and only these are analyzed. This effect is particularly relevant at kinetic energies from 50 to 1500 eV, where the surface sensitivity varies around 2 to 10 atomic layers (an atomic layer is of the order of 3Å).

In order to understand the surface sensibility of the technique, Beer's law is inspection, which defines the probability that a photoelectron will escape from the sample without losing energy. The flow of electrons I_k passing through a solid of thickness d without loss of energy, where each unit of thickness of matter absorbs the same fraction of energy, experiences an exponential attenuation that is given by

$$I_k = I_0 \exp^{-d/\lambda \cos\theta}, \tag{3.3}$$

where I_0 is the intensity or flow of emitted electrons, θ is the exit angle of the electrons concerning the normal to the surface, and λ is the inelastic mean free path (IMFP), which is defined as the average distance an electron travels between successive inelastic collisions. When θ is normal to the surface, 95% of the detected photoelectrons originate from a depth of 3λ, known as the analysis depth. For a grazing angle, the depth of analysis is shallow, and the inelastic bottom is practically non-existent.

The IMFP for electrons varies with their kinetic energy, as shown in figure 3.3 (dots), and it can be described by a universal curve (solid line), which is experimentally derived,

and it is express as:

$$\lambda = \frac{538}{E_k^2} + 0.41(\alpha E_k)^{1/2}, \tag{3.4}$$

where E_k is the kinetic energy, and α is the monolayer thickness (nm). From a careful inspection of the plot, it is possible to notice that for typical kinetic energy range in XPS experiments, the IMFP around is about 5 nm, which implies that effectively the photoelectrons that did not suffer any energy loss must have been emitted from the last atomic planes of the material, close to the surface.

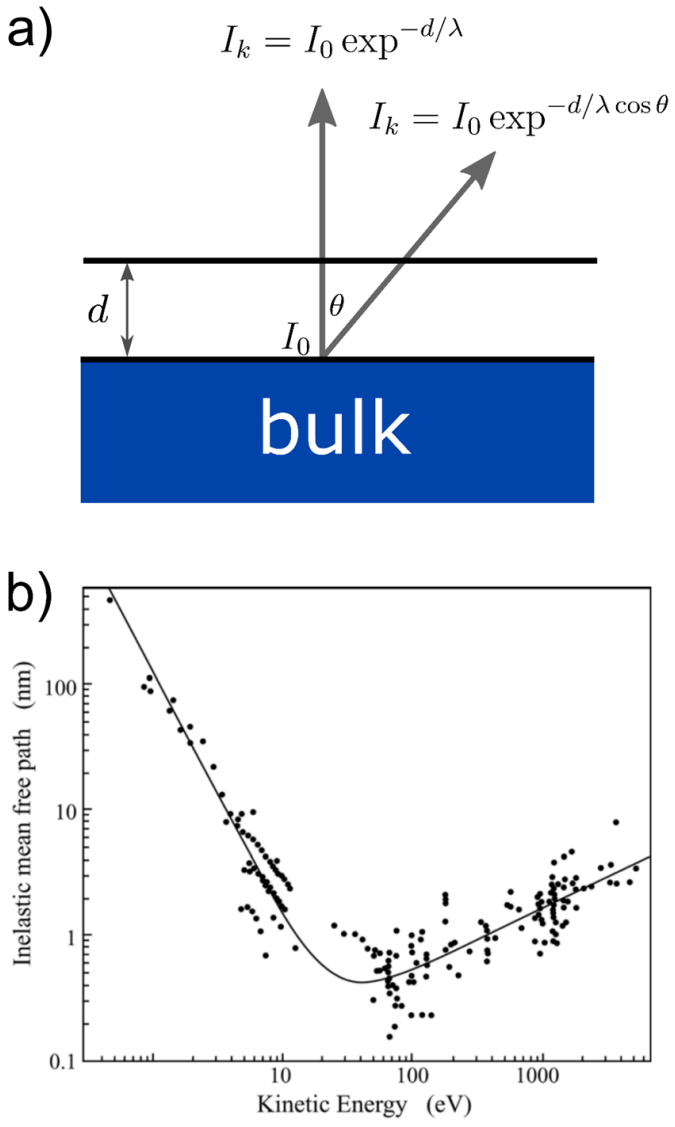

Figure 3.3: (a) Flux of electrons I_k passing through a solid of thickness d without energy loss. The dependence of I_k on θ, d and λ is given by equation 3.2. (b) The dependence of the IMFP on the kinetic energy (each dot represents a different element or transition for metals). The solid line represents the universal curve that describes the experimental data. Taken from [94]

3.1.2 Instrumentation

The experiment needs a source of photons, an electron analyzer, and a control and data acquisition system (see diagram in figure 3.4). Furthermore, the photoemission experiment has to be carried out under ultra-high vacuum (UHV) conditions to *(1)* guarantee the surface of the sample does not change during the experiment. According to the kinetic theory of gases, the flux of molecules impinging on the surface is directly proportional to the pressure, so at 10^{-6} mbar and RT a monolayer is formed on the surface in $1.5s$, unlike pressure around 10^{-10} mbar where this happens after hours, and *(2)* avoid the loss of information caused by possible collisions of the photoelectrons with residual gases on their way from the sample to the detector through the analyzer.

The photon source could be synchrotron radiation sources, which cover the whole photo emission energy range, or a laboratory source that has a specific energy, such as UV or X-ray. In our case, we use an X-ray tube to explore the sample's core levels. The X-ray tube has two anodes (Mg and Al), and the highest probability transitions of occurrence, given by the selection rules, are the $k_{\alpha 1,2}$ ($2p_{3/2,1/2} \rightarrow 1s$) and the energy of the transition are $1486.6eV$ and $1253,6eV$ for Al and Mg respectively. The line width of these transitions is about $1.0eV$, which does not limit the resolving power needed for the technique. The same transitions for doubly and triply ionized Al and Mg atoms produce the $k_{\alpha 3,4}$ (which are approximately $10eV$ from the main line and have about 10% its intensity) and $k_{\alpha 5,6}$ lines, which have much less likely to occur than the $k_{\alpha 1,2}$ and are known as satellite lines. In addition, these lines are superimposed on a continuum that is a consequence of the *bremsstrahlung* process or braking radiation produced by the deceleration of a charged particle.

The concentric hemispherical analyzer (CHA) consists of three components: *(1)* a collection of electrostatic lenses, which retarding and focusing the electrons emitted from the sample; *(2)* a hemispherical electron analyzer, which uses an electric field to scatter electrons and filters, allowing only those with particular kinetic energy to pass through; and *(3)* a multiplier set, where the electrons that make it through the detector are counted.

Two metallic concentric hemispheres constitute the deflector. An electrostatic field is established between them, which scatters electrons so that just those with a range of

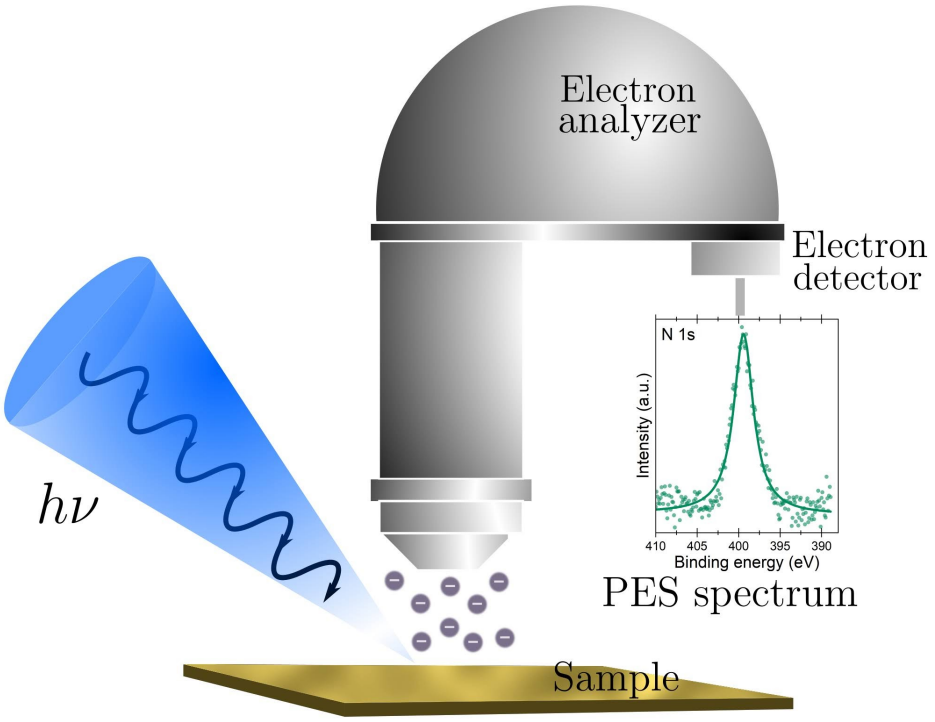

Figure 3.4: Experimental setup diagram for PES, consisting of an ultrahigh vacuum system, an X-ray source, a concentric hemispherical analyzer (CHA) and the data acquisition system.

specific kinetic energies can pass the exit slit. There is a mean equipotential surface between the two hemispheres at $R_0 = (R1 + R2)/2$, the kinetic energy of an electron traveling along the center line R_0 is called the pass energy E_0, the relation between the potential deflector ΔV and the pass energy $E_0 = eV_0$ of the electrons is given by:

$$E_0 = \left(\frac{R_1 R_2}{R_2^2 - R_1^2} \right) e\Delta V, \tag{3.5}$$

The analyzer resolution is defined by ΔE, which is the full width at half maximum (FWHM) for the energy distribution of a monoenergetic electron beam. Mathematically it can be described as

$$\Delta E = E_0 \left(\frac{\omega}{2R_0} + \frac{\alpha^2}{4} \right), \tag{3.6}$$

where ω is the size of the output slit and α is the angle at which the electrons enter the deflector. This equation is obtained from the development of the expressions that describe the trajectories of the electrons, considering just lower-order terms.

The analyzer can be operated in two modes: *1)* constant $\Delta E/E$ mode. In this case, the collection of lenses is used to focus and transport the electrons to the analyzer input slit, while the pass energy varies according to electron kinetic energies E_k. *2)* constant ΔE

mode, the analyzer pass energy is kept constant, and the lens system is used to focus and decelerate the electrons coming from the sample with a potential delay difference V_R. This potential varies within a range to sweep the interval of kinetic energies explored. In this last operating mode, ΔE has the same value for the whole spectrum. Therefore it is easier to quantify it. A set of channel electron multipliers (CEM) is used to count

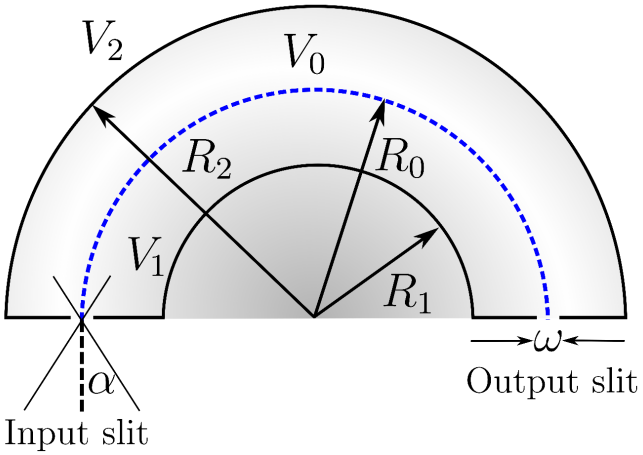

Figure 3.5: Schematic sketches of the concentric hemispherical analyzer (CHA).

the electrons after passing through the deflector output split. This device is made of glass, and inside, it is covered by a highly resistive material with suitable emissivity for secondary electrons. An electron enters one end of the CEM, collides with its internal wall, and causes the emission of secondary electrons. These are accelerated by the high potential difference and cause the emission of more electrons that will continue with the same process, generating a measurable current.

3.1.3 Spectra analysis

The chemical information, for instance, composition and relative concentration between the elements on the sample's surface, can be determined from curve fitting XPS spectra. In order to obtain meaningful results, all the physical and chemical contributions to the photoelectron spectra have been considered.

1) **Background subtraction.** For the background subtraction, the Shirley method [95] was used, in which two arbitrary points P_a and P_b are selected on each side of the peak, the intensity at point b, at higher kinetic energy, I_b is taken as background and is subtracted from the initial intensity I_s obtained for each point P_n, so that the intensity

at each point is given by:

$$I_s^{'}(n) = I_s(n) - I_b, \tag{3.7}$$

which correspond to an iterative process.

2) **Lineshape of the peak.** The uncertainty principle defines the intrinsic lineshape of the energy level, and it is described as Lorentzian energy distribution. This original shape is modified by the photon broadening and instrumental factor, which have Gaussian character. In this way, the lineshape of the photoemission peak is a convolution of Lorentzian and Gaussian functions, this is Voigt function. For this thesis, pseudo-Voigt functions, which are Gaussian–Lorentzian sum and product functions, were used.

3) **FWHM of the peak.** The spectral resolution or FWHM of the peaks in the photoemission spectra is determined by the intrinsic width of the photoelectric line, and the resolution of the instrument [96]. The intrinsic width of the ΔE_{line} peak is related to the Heisenberg uncertainty principle and is determined by the half-life time τ of the state after the photoemission. Instrumental effects broaden the photoemission peak due to the inherent FWMH of the incident ΔE_{x-ray} radiation line and the resolution of the $_{analyzer}$. Hence, the contributions to the FWHM of the photoemission peak are related through the following expression:

$$FWHM_T = \Delta E_{x-ray}^2 + \Delta E_{line}^2 + \Delta E_{analyzer}^2, \tag{3.8}$$

The area under the photoemission peaks is related to the concentration of the elements present on the sample surface. Calculating the area and correcting for the appropriate instrumental factors can determine each element's percentage. The number of electrons coming from an element of volume with constant area and thickness dz is given by,

$$I_{ij} = KT(E_k)\sigma_{ij}L_{ij}\int_0^b N_i(z)e^{\frac{-z}{\lambda(E_k)\cos\theta}}, \tag{3.9}$$

where I_{ij} is the intensity of the peak j of the element i, in the equation, K represents the instrumental constant and contains the X-ray flux, geometric factors, the irradiated sample area, and the acceptance angle of the photoelectrons by the analyzer. $T(E_k)$ is the function of transmission of the analyzer and could be obtained from the equipment

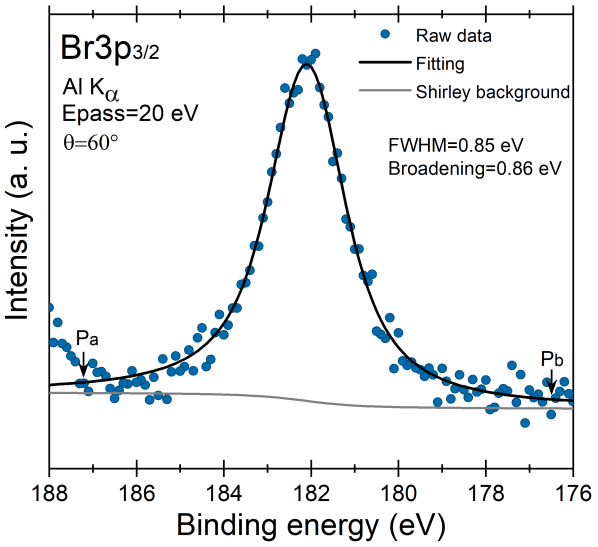

Figure 3.6: $Br3p_{3/2}$ spectrum after deposition of Br4TPP on Cu(111) at submonolayer regimen. The data was collected at a grazing emission angle of 60° from the surface normal and $E_{pass} = 20eV$. The energy of peak at $182.1eV$ indicates that Br-Cu bonds are formed. The Shirley background is also shown between P_a and P_b.

and properly used to normalize the raw data. The angular asymmetry factor L_{ij} is the probability of photoelectron emission in the direction of the analyzer; when the angle between the incident radiation and the input axis of the analyzer is 60° this quantity is constant for each orbital, and element. The photoemission cross-section σ_{ij} is the probability that an incident X-ray photon generates the photoemission of an electron from orbital j of an element i. The values of σ_{ij} were calculated by Scofield for the radiation $Al\alpha_{k1,2}$.

$N_i(z)$ is the number of atoms per unit volume or concentration of element i, $\lambda(E_k)$ is the IMFP in the sample, and θ corresponds to the input angle of the electrons with respect to the normal to the surface. The exponential term represents the fraction of photoelectrons produced at a depth z that manage to leave the sample without energy loss. If it is assumed that the concentration of the elements in the sample is homogeneous at a depth of analysis, equation 3.7 can be integrated between zero and the thickness of the sample; the term $e^{\frac{-z}{\lambda(E_k)\cos\theta}}$ tends to zero, because the depth of analysis is more significant than IMFP, so now,

$$I_{ij} = KT(E_k)\sigma_{ij}L_{ij}n_i\lambda(E_k)\cos\theta \tag{3.10}$$

In order to determine the relative concentration between two elements, several parameters in equation 3.8 are equal for both elements. Thus they cancel, and now

we have,

$$\frac{n_i}{n_k} = \frac{I_i}{I_j}\frac{\sigma_{kl}\lambda(E_k^{kl})T(E_k^{kl})}{\sigma_{ij}\lambda(E_k^{ij})T(E_k^{ij})} \tag{3.11}$$

3.2 Scanning Tunneling Microscopy

Scanning tunneling microscopy (STM) is an experimental technique based on the principle of quantum tunneling of electrons between two electrodes separated by a potential barrier. This technique is typically used for imagining surfaces of materials with sub-atomic resolution.It was pioneered by Gerd Binnig and Heinrich Rohrer in 1982, who were awarded a Nobel Prize in Physics in 1986. This invention opened up a new research field, directly accessing the local density of the surface sample's state and allowing the visualization of atomic and molecular structures.

3.2.1 Quantum tunneling effect

According to the classical mechanic's theory, a particle traveling toward a one-dimensional potential barrier, as it is shown in figure 3.7, with mass m and energy E lower than the height of the barrier ($E < V_0$) can not penetrate it to go from one side to the other. In quantum mechanics, on the other hand, the particle's motion is described by a wavefunction that satisfies Schrödinger's equation. Solving Schrodinger's equation inside the barrier, the motion of the particle can be given by:

$$\psi(z) \propto e^{-kz} \tag{3.12}$$

where $k = \sqrt{2m(V_0 - E)/\hbar}$ for $E < V_0$, with $\hbar$ Planck constant and m the electron mass. This result shows up there is a non-zero probability ($|\psi(z)|^2$) that the particle penetrates the barrier, this phenomenon is known as quantum tunneling. Moreover, probability of observing the electron in the other side of the barrier is described by the transmission coefficient,

$$T = \frac{|\psi(z)|^2}{|\psi(0)|^2} \propto e^{-2kd} \tag{3.13}$$

such as one can notice, the transmission coefficient depends exponentially on the width of the potential barrier d.

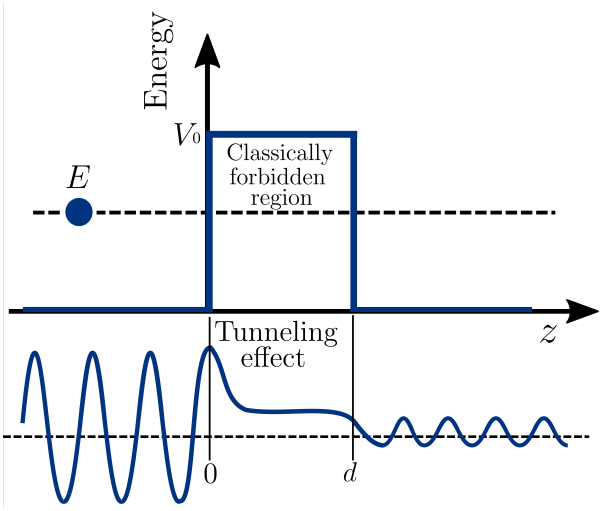

Figure 3.7: One dimensional model of quantum tunneling effect representation.

3.2.2 Working principle

Figure 3.8a) illustrates how the STM works. A sharp metallic tip is attached to a piezoelectric scanner. This scanner can position the tip both lateral and vertically with sub-angstrom precision. The wavefunction of the electrons in the sample and the tip overlap for a small tip-sample distance. Hence, when a bias voltage is applied, the Fermi level of the sample is shifted with respect to the Fermi level of the tip, and the tunneling of the electrons happens (see figure 3.8b).

In order to get a better understanding of the physics behind the tunneling phenomenon, the one-dimensional potential barrier model could be used, assuming the tunneling junction as a metal-vacuum-metal, where the electron wavefunction at the metallic surface decays exponentially inside the vacuum barrier as a function of the distance. Moreover, electrons into the solid experiment an effective potential barrier defined by the work function Φ. If considering the same work function for the tip and the sample and small biases ($eV << \Phi$) it is possible to approximate the tunneling barrier as a rectangular potential barrier, and the electrons will tunnel from energy level close to the Fermi level in one of the electrodes to the Fermi level in the other one. Now, the tunneling current I_t could be given by

$$I_t \propto e^{-2kz} \text{ with } k = \sqrt{2m_e\Phi/\hbar} \tag{3.14}$$

where $V_0 - E = E_{vacuum} - E \approx \Phi$.

On the other hand, strictly speaking, the expression describing the tunnel current at the STM tunnel junction is given by

$$I_t(x,y,z,eV) \approx -\frac{4\pi e}{\hbar}\int_0^{eV} T(z,\epsilon,V)\rho_{\mathrm{s}}(\epsilon,x,y)\rho_{\mathrm{t}}(\epsilon-eV)d\epsilon \tag{3.15}$$

where ρ_{s} is the local density of state (LDOS) of the sample and ρ_{t} is the density of state (DOS) of the tip. Typically in STM, the tip is made of Tungsten (W) or Platinum-Iridium alloy (Pt-Ir). These tips have a flat DOS around the Fermi Level. In this scenario, $\rho_{\mathrm{t}}(\epsilon - eV) \sim \rho_{\mathrm{t}}(0)$, which means that the DOS of the tip is independent of the energy and therefore the STM image represents just the LDOS of the sample. In this way, the tunneling current expression is simplified as:

$$I_t(x,y,z,eV) \approx -\frac{4\pi e}{\hbar}\rho_{\mathrm{t}}(0)\int_0^{eV} T(z,\epsilon,V)\rho_{\mathrm{s}}(\epsilon,x,y)d\epsilon \tag{3.16}$$

For a rectangular barrier, the transmission coefficient $T(z,\epsilon,V)$ can be written as

$$T(z,\epsilon,V) \approx e^{-2\frac{d}{\hbar}\sqrt{2m\phi}} \tag{3.17}$$

where ϕ is the effective local barrier height, this term shows the exponential dependence of the tunneling current with sample-tip distance z, which defines the high vertical spatial resolution of the technique. Now the final expression for the tunneling current in STM is given by

$$I_t(x,y,z,eV) \approx -\frac{4\pi e}{\hbar}\rho_{\mathrm{t}}(0)e^{-2\frac{d}{\hbar}\sqrt{2m\phi}}\int_0^{eV} \rho_{\mathrm{s}}(\epsilon,x,y)d\epsilon \tag{3.18}$$

which shows that the tunneling current measured at a particular bias is proportional to the integral of the DOS of the sample from the Fermi level to eV.

The most used mode to acquire an STM image is the constant-current topographic. The tip scans the sample at a fixed bias voltage. The feedback loop adjusts the position of the tip in the z direction to keep the measured current at a fixed setpoint value. The z trajectory of the tip maps the surface contour, leading to the STM image formation. The tunneling current depends on the tip-sample distance and the integral of the DOS from the Fermi level to eV. Hence, the image corresponds to surface corrugations for samples with a homogeneous DOS. On the other hand, STM images from materials with the heterogeneous spatial distribution of DOS represent a combination of elects due to

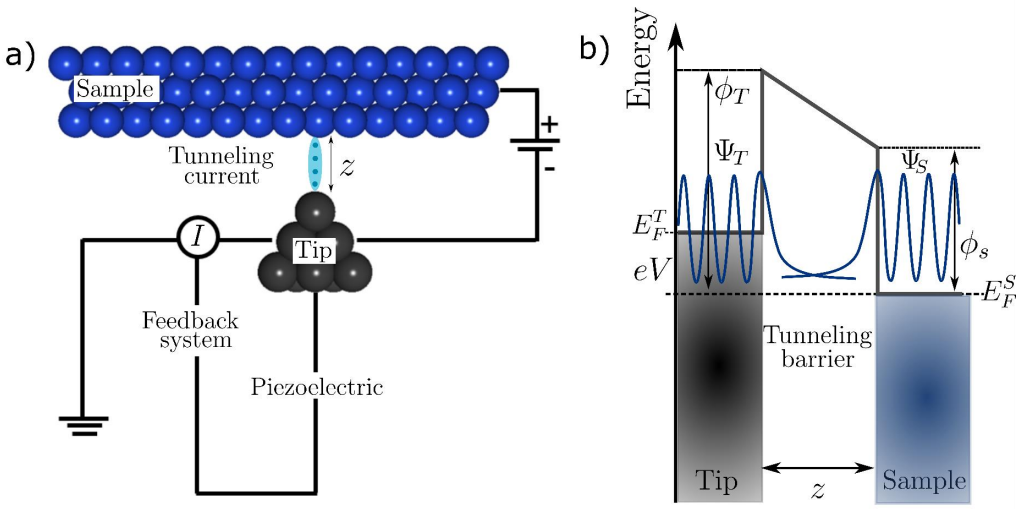

Figure 3.8: Representation of the tunneling process at the STM tunnel junction. For positive sample bias ($V > 0$) empty sample states are probed. The opposite process happens at negative bias ($V < 0$), where occupied states are explored.

geometric corrugations and electronic density of states [97, 98].

Probing locally the electronic properties of the sample is possible by scanning tunneling spectroscopy (STS), which consists of measuring directly the difference conductance (dI/dV). According to the equation 3.9 the deviate of the tunneling current respect to the sample bias V is proportional to $\rho_s(\epsilon, x, y)$, such as:

$$\frac{dI}{dV} \propto \rho_s(eV, x, y), \tag{3.19}$$

3.2.3 Experimental setup at Grupo de Fisica de Superficies

The results shown in this thesis were obtained from experiments carried out in the Grupo de Fisica de Superficies, located in the Department of Applied Physics of the Institute of Physics "Gleb Wataghin" (IFGW) at Campinas State University (UNICAMP). The system consists of two interconnected chambers, one equipped with standard cleaning facilities, a Low Energy Electron Diffraction (LEED), an e-beam evaporator for metal depositions, and a Knudsen-cell evaporator for molecular depositions. Moreover, the chamber contains the hemispherical energy analyzer SPECS PHOIBOS 150 with multi-channeltron detection. This chamber has a base pressure of 2×10^{-10} mbar. The XPS data presented in this thesis were acquired using Mg K_α and Al K_α sources with a photon energy of 1253.6 eV and 1486.6 eV, respectively.

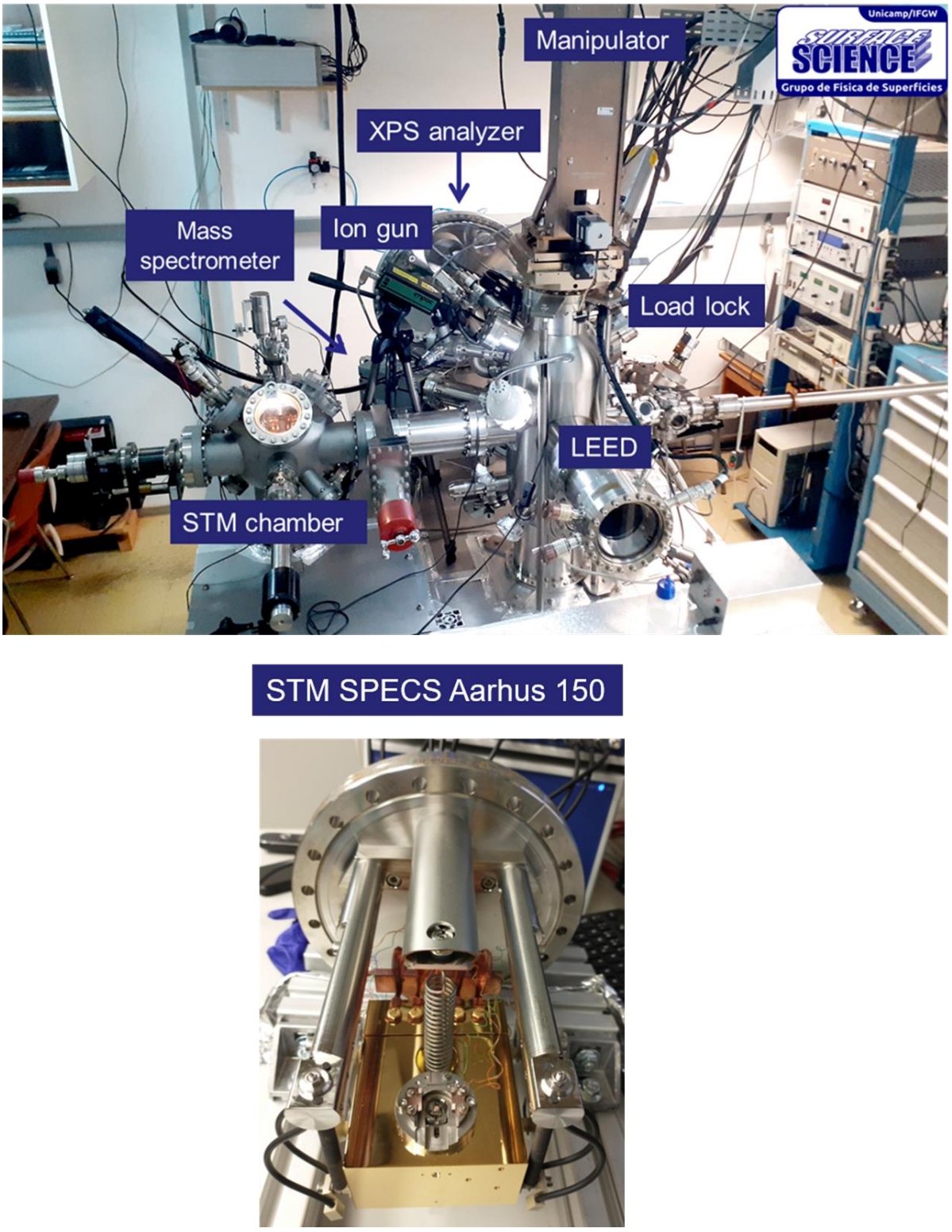

Figure 3.9: UHV system at GFS, IFGW - UNICAMP. Above panel: Both chambers are shown, highlighting principal components of the system (Credit: Abner de Siervo). Below panel: SPECS Aarhus 150 with a tungsten tip cleaned *in situ* by Ar^+ sputtering and equipped with a SPECS SPC 260 controller.

The other one is equipped with an STM SPECS Aarhus 150 with a tungsten tip cleaned *in situ* by Ar^+ sputtering (SPECS SPC 260 controller). All STM data were acquired at

RT, with a base pressure of 6 $\times$ 10^{-11} mbar and in the constant current mode where bias is applied to the sample while the tip is maintained closed to ground potential. The images were analyzed using the WSxM [99], and Gwyddion [100] software. In addition, a correction matrix was determined using an atomic resolution image of the substrate to calibrate each analyzed STM image.

3.3 Sample preparation

3.3.1 Molecular precursor

In order to synthesize complex carbon nanostructures and doped Gr via bottom-up methods, we selected three different single molecular precursors (see figure 3.3.1):

(1) Hexamethyl borazine $C_6H_{18}B_3N_3$ (HMB), see figure 3.3.1a), is a commercial molecule (Sigma-Aldrich), which has to be kept at ∼253 K and preserved from light to avoid its degradation due to photo-thermal decomposition. For this purpose, the molecules in powder form were introduced into a quartz ampoule which were also maintained below ∼253 K inside a Peltier cooler (homemade). The reservoir was connected to the UHV chamber via a leak valve, as shown in figure 3.11a). It is also connected to a valve that allows differential pumping down to 10^{-4} mbar. Before experiments, the precursor was degassed by heating and pumping cycles. To introduce HMB into the UHV chamber, it was heated at 350 K, where the entire molecule (164.7 g/mol) was detected by the mass spectrometer, which suggests that HMB precursor did not degrade during evaporation, see figure 3.11b).

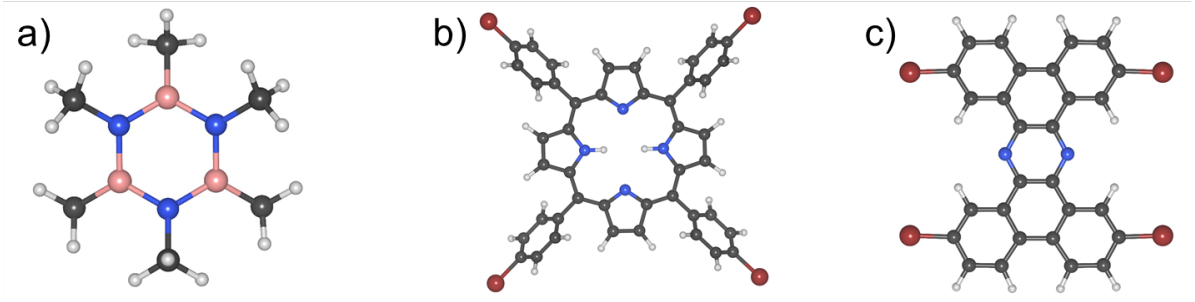

Figure 3.10: Atomic structure of (a) Hexamethyl borazine $C_6H_{18}B_3N_3$ (HMB) (b) 5,10,15,20-tetrakis(4-bromophenyl)-porphyrin (H_2TBrPP) and (c) 2,7,11,16-Tetrabromotetrabenzo[a,c,h,j]- phenazine (2TBTBP). C, H, N, B and Br atoms are marked in gray, white, blue, pink and burgundy, respectively

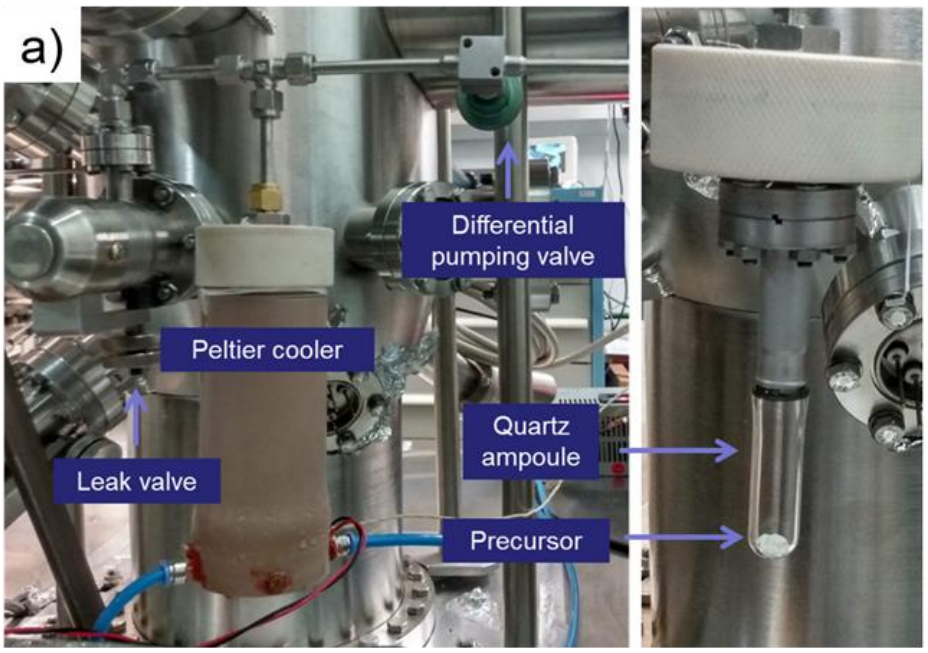

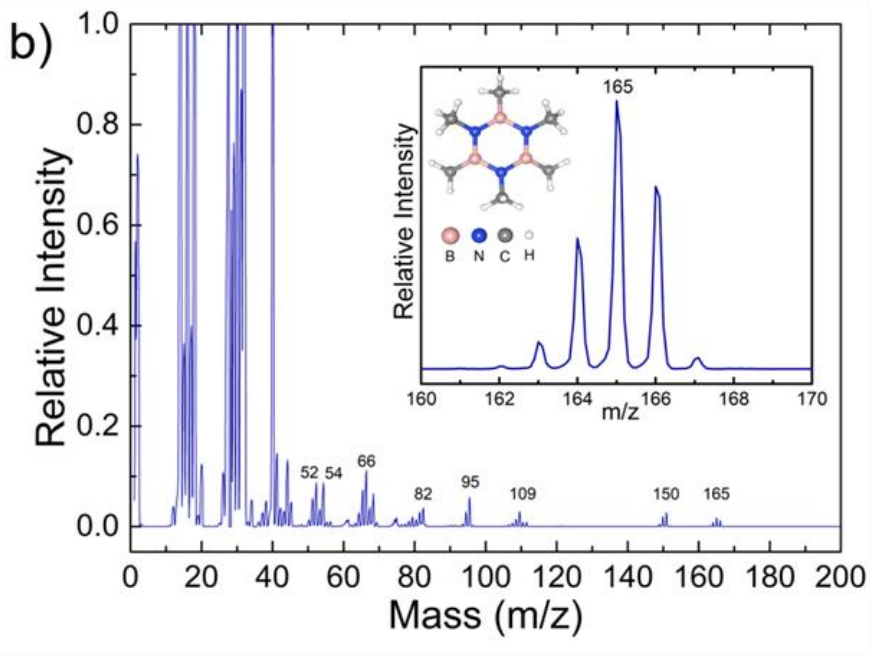

Figure 3.11: (a) System implemented during this thesis's development in the GFS main chamber to deposit HBM. (b) The mass spectrum of hexamethyl borazine was acquired during the synthesis. Peaks at m/z of 165 correspond to the molecular weight of the precursor (164.7 g/mol), which suggests that the molecule did not degrade during evaporation at 350 K. According to NIST Mass Spectrometry Data Center, other peaks indicated in the spectrum, along with peaks around them but less abundance, are expected for the precursor. Pressure chamber: 1.5×10^{-6} mbar

.

(2) 5,10,15,20-tetrakis(4-bromophenyl)-porphyrin (H_2TBrPP), see figure 3.3.1b, is also a commercial molecule purchased from Porphyrin Chemical Engineering. The sublimation was carried out in a homemade Knudsen-cell evaporator. After a long evaporator degassing, the sublimation temperature was maintained at around 560 K. As our system

does not have a quartz balance, for our experiments, we determined the coverage of the sample after deposition by counting the number of molecules per area in STM images.

(3) 2,7,11,16-Tetrabromotetrabenzo[a,c,h,j]- phenazine (2TBTBP) molecule is a planar polycyclic hydrocarbon with two nitrogen atoms and four bromine atom terminals. Liu *et al.* [101] reported for the first time the synthesis of the molecule, and for our study the Prof. Ronaldo Aloise Pilli's lab at the Chemistry Institute -IQ Unicamp synthesized the precursor. Due to it is not a commercial precursor, long periods of degassing and mass spectrometry measurements were necessary. These allowed the estimation of the precursor sublimation temperature. According to Liu W. *et al.* [101] sublimation is promoted after reaching $350°C$. According to the experimental setup and the thermocouple placement within the system, this value may vary, as shown in our results, where we estimate the sublimation of molecules from $280°C$.

3.3.2 Metal surface substrate

For preparing the different metal surfaces used in this thesis, we carried out the conventional clean surface procedure, which consists of several cycles of sputtering-annealing. In simple words, a beam of accelerated Ar^+ ions is directed toward the surface, bombarding it. This process removes all the impurities from the first layers of the surface. Typically the pressure in the chamber after opening the leak valve Ar gas is about 1×10^{-6} mbar, and the beam energy of sputtering is between 0.6 and 1.2 keV. In order to give enough energy for the reconstruction of the erosion substrate left by the sputtering and promote the desorption of additional impurities, heat treatment, called annealing, is applied. The annealing temperature depends on the material. According to Castro *et al.* [102] the temperature has to be chosen at about 50% - 70% of the melting point. After several cycles, depending again on the initial conditions of each crystal, the quality of the sample is verified by LEED, XPS, and STM.

For this project, we used four different single face-centered cubic (fcc) crystals: Rh(111), Ir(111), Cu(111), and Ag(100). Figure 3.12 shows these crystalline planes, together with the unitary cell and atomic resolution STM images of Ag(100) and Cu(111). .

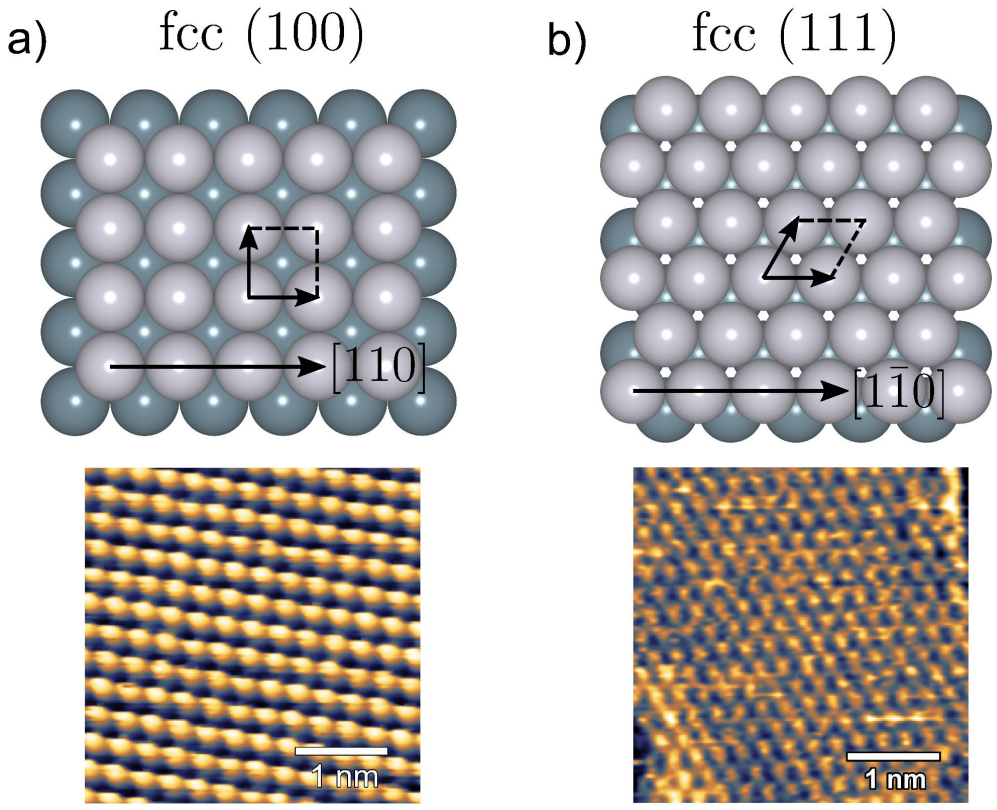

Figure 3.12: Top view of the (a) (100) and (b) (111) surface of the fcc lattice together STM atomic resolution of Ag(100) and Cu(111) acquired during the developed of this thesis.

Chapter 4

Doping effect by introduction of h-BN defects in Graphene

This chapter is based on the publication:

Nataly Herrera-Reinoza ,Alisson Ceccatto dos Santos, Luis Henrique de Lima, Richard Landers, and Abner de Siervo

Atomically Precise Bottom-Up Synthesis of h-BNC: Gr Doped with h-BN Nanoclusters

Chem. Mater. 2021, 33, 8, 2871–2882

In this Chapter, we present the successful growth of hexagonal boron-nitrogen-carbon monolayer (h-BNC) as a ternary alloy monolayer obtained from an unexplored single molecular precursor (hexamethyl borazine – $C_6H_{18}B_3N_3$) using a conventional CVD approach on Ir(111). Due to the stoichiometry of this novel precursor, we would expect that the h-BN to Gr ratio should be 1:1 for a totally segregated sample, and in the case of h-BNC alloy formation, a B:N:C ratio of 1:1:2. Therefore, it is possible considering that the growth happens under conditions that do not benefit a specific sp^2 bond formation (i.e. B–N, C–N, C–B, C–C), leaving the control of the synthesis exclusively to the choice of the substrate conditions. Rh(111) and Ir(111) crystals were chosen as substrates since the on-surface synthesis of Gr and h-BN by CVD has been widely explored on these surfaces. Based on references [60, 103–115] we recognized that the growth temperature range for Gr and h-BN on Rh(111) and Ir(111) are similar which favors the simultaneous chemical activation of bound breaking and bond formation between the atoms in the precursor. Furthermore, the typical superlattice formed for the h-BN is easily distinguishable from the Gr moiré pattern, which represents an advantage for STM measurements. Thus, this Chapter aims to provide a careful study of h-BNC alloy synthesis using a novel single precursor. The conformation structure of the monolayer h-BNC on Ir(111) and its correlation with the local electronic properties is discussed based on scanning tunneling microscopy/spectroscopy (STM/STS) and X-ray photoelectron spectroscopy (XPS) results. The results show an h-BNC structure that can be described as BN-doped Gr since the moiré lattice parameter is preserved along with the alloy. This BN-doped cluster, renamed as h-BN "nanodonuts" according to the electronic density exhibited in STM images, have a tendency to place specific positions within the moiré superstructure, and it is constituted by at least $(BN)_8$ units arranged in six-fold BN rings conformation, as evidenced by simulation of STM images based on density functional theory (DFT), Prof. Luis Henrique de Lima carried out these calculations. For a BN concentration of about 17%, a band gap between 1.4 and 1.6 eV was determined. The versatility of the novel molecular precursor is proved by the growth of a high-quality h-BN monolayer on Rh(111).

4.1 Growth of h-BNC on Rh(111) surface

In order to explore the adsorption and reaction behavior of HMB as a new precursor to create the so-called sp^2 *nanomesh* systems with carbon, boron, and nitrogen atoms distributed over the honeycomb lattice, we started with Rh(111) as substrate. First, the Rh(111) surface was kept at room temperature (RT) while it was exposed to the precursor vapor at 1.5×10^{-6} *mbar* for 7 min, followed by subsequent annealing treatments. STM image (see figure 4.1b) recorded after the deposition shows the saturation of the surface. The first important conformation changes occur at 800 K, as seen in the figure 4.1c, given that initial arrangements into nanoscale cluster are recognized. Figure 4.1g shows the evolution of C 1s core level spectrum with temperature. At 800 K the spectrum shows a slight shift of the peak position, which suggests a chemical reaction with new bond formation.

At 900 K, carbon atoms are still presented on the surface and some fragments display the characteristic h-BN nanomesh conformation (see figure 4.1d). Self-limited h-BN islands with multiple short domains and high density of defects are formed after annealing at 1000 K, as displayed in figure 4.1e. XPS results also exhibit a considerable decrease in the intensity of the C 1s peak, which indicates that the most of the carbon atoms supplied by the precursor are not present on the rhodium surface. Since the last annealing step happened near the temperature where the Rh has a high carbon solubility [116, 117] ($\sim$ 1100 K), carbon dissolution into the substrate without the formation of an sp^2 structure at the surface is a rather plausible scenario.

It is important to note that depositing the precursor at RT that saturates the surface with disordered but still intact molecules and subsequently annealing the system does not promote an efficient route to synthesize h-BN, Gr, neither h-BNC. A plausible explanation involves the competition between energetic chemical reaction barriers and an efficient on surface diffusion of the products to overcome the entropy of the disordered system to form a ordered framework. However, the already formed amorphous system with new chemical bonds produced during the annealing treatments is probably blocking an efficient self-assembling and higher annealing temperatures only decompose the precursor without an appreciable effect on inducing ordering [110, 118, 119].

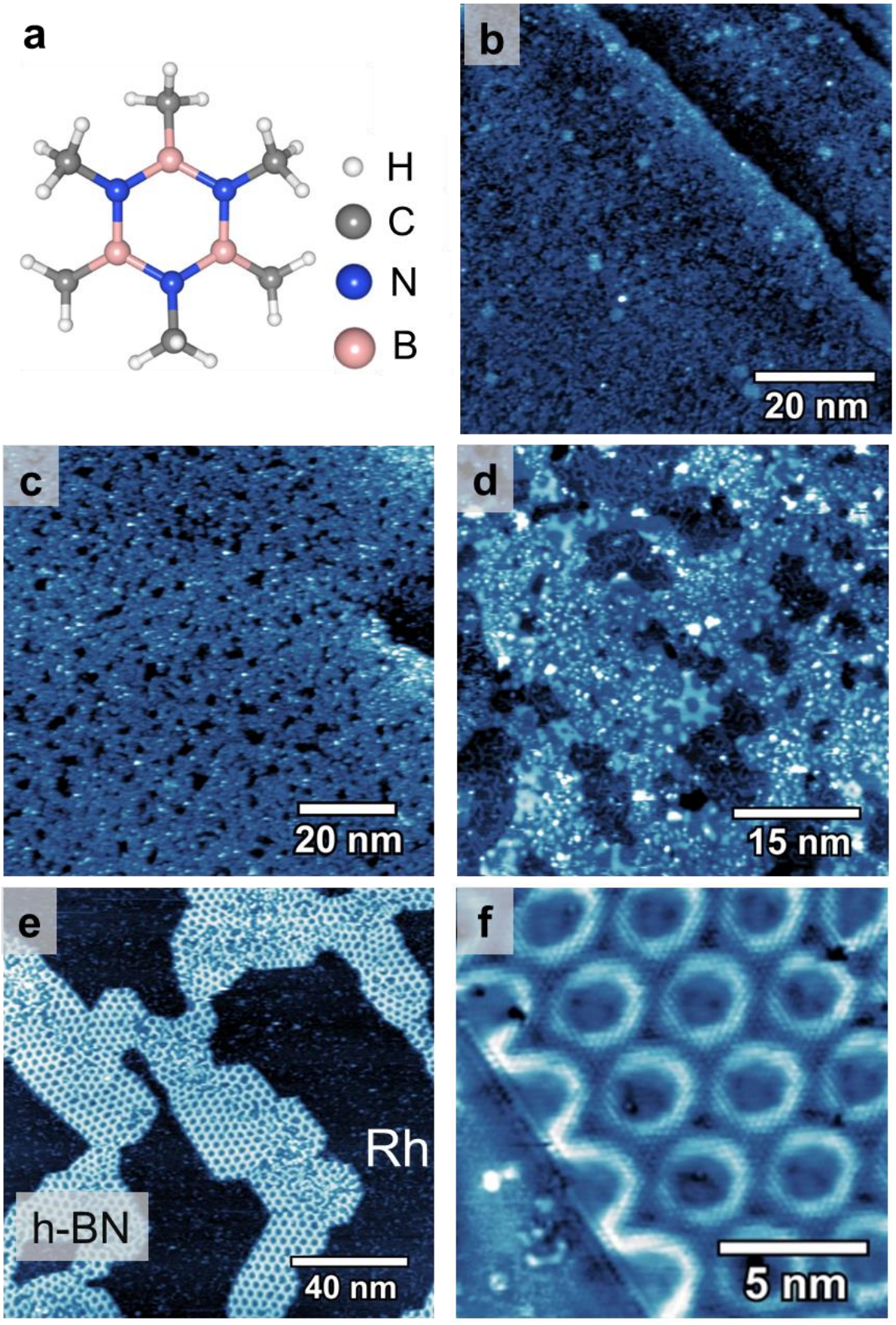

Figure 4.1: Synthesis process of hexamethyl borazine (HMB) on Rh(111): (a) Sketch of HMB. STM images of Rh(111) surface after be exposed to molecular precursor at (b) RT, (c) annealing at 800 K, (d) annealing at 900 K, and (e) annealing at 1000 K, where is observed h-BN auto-limited island. (f) STM image displays the boundary of the island. Tunneling parameters: (b) $V = -0.85\ V$, $I_t = -0.73\ nA$, (c) $V = 1.58\ V$, $I_t = 0.12\ nA$, (d) $V = -0.67\ V$, $I_t = -0.30\ nA$, (e)-(f) $V = -0.26\ V$, $I_t = -5.30\ nA$.

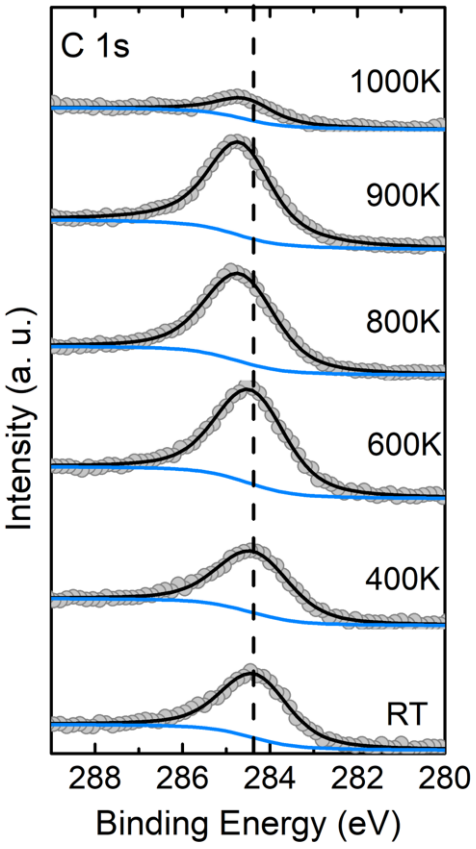

Figure 4.2: C 1s core-level XPS spectrum acquired for each thermal treatment carried out on the Rh(111) surface after precursor deposition at RT. The XPS data was collected at a grazing emission angle of 60° from the surface normal. The dashed line indicates the peak position at RT.

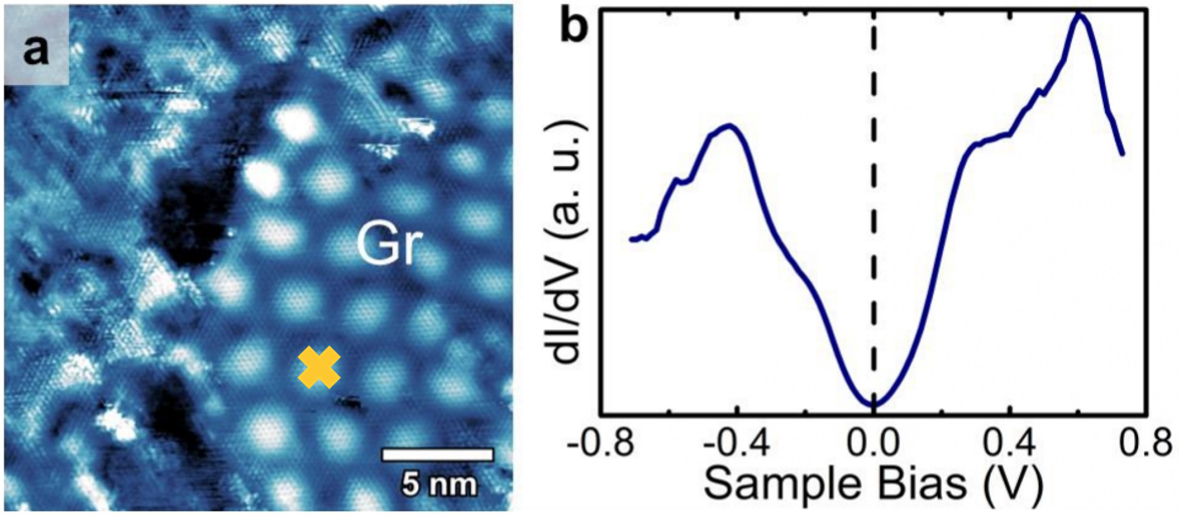

Figure 4.3: (a) STM image of Gr nanoisland formed from precursor deposition with substrate at 800 K and subsequent annealing at 900 K. (b) Representative STS curve acquired on the top of the moiré pattern of Gr nanoisland shown in (a) (position indicated by a cross). Tunneling parameters: $V = 0.02\ V$, $I_t = 5.64\ nA$

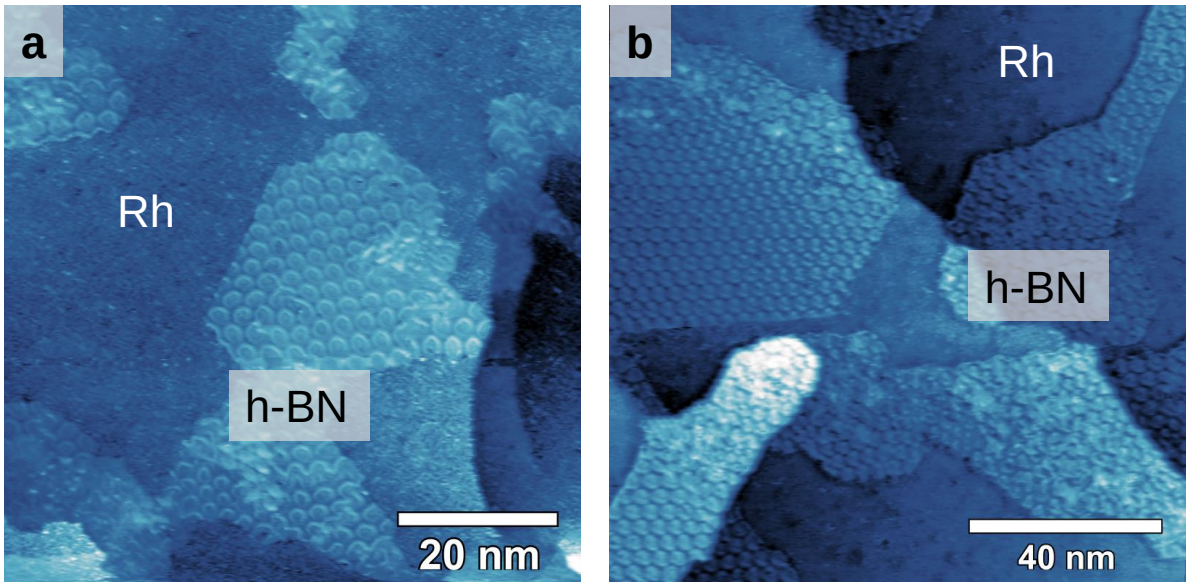

Figure 4.4: Synthesis process of hexamethyl borazine (HMB) on Rh(111): h-BN islands formed on Rh(111) after annealing at 1000 K on the sample kept at 800 K during the precursor deposition process. Tunneling parameters: (a) $V = -0.01V$, $I_t = -0.33\ nA$, (b) $V = -0.01\ V$, $I_t = -5.75\ nA$

To gain insight on that, additional growths were done with the surface previously heated above room temperature. A particularly interesting growth consisted of exposing the Rh(111) surface at 800 K to 1.4×10^{-6} *mbar* pressure of HMB. The growth under these conditions was chosen, since experimental evidences indicate that the first change in the previous samples happens around this temperature. STM images do not show signs of periodic structure, what makes sense because this temperature is outside of the growth temperature range for both materials (h-BN and Gr) on Rh(111). However depositing the molecules under this substrate condition could help to understand the growth kinetics. For instance, at RT the precursors and products bind to the surface and have less mobility to form more complex structures. After the deposition at 800 K, we performed an annealing at 900 K, having as result the formation of small islands, as shown in figure 4.3a. These islands are identified as being Gr, corroborated by the following results: (1) we have observed the expected moiré pattern of Gr on Rh(111) with bright protrusions in a dark surrounding (bright-atop contrast) with a periodicity of (3.07 ± 0.07) nm, in agreement with the reported values in the literature [120, 121], and (2) the LDOS measured by the STS technique evidences the characteristic V-shape curve of Gr [122], centered at the Fermi level (0 eV) as can be observed in the STS curve shown in figure 4.3b, which was acquired on the top of the moiré pattern. After annealing at 1000 K, the Gr islands disappeared from the surface and solely h-BN islands are formed (see

figure 4.4). As described above, carbon atoms vanish after thermal annealing at 1000 K, therefore, it is an important point to pay attention in our goal to grow BNC ternary alloy or hybrid structure of h-BN–Gr from a single precursor on the Rh(111) surface, since the growth temperature of the h-BN coincides with the dissolution temperature of carbon into the Rh bulk. It is worth emphasizing that under our experimental conditions, it was not possible to observe the Gr dissolve into the Rhodium beginning at 1053 K as reported by Dong *et al.* [110].

4.1.1 Synthesis of high quality h-BN

Taking these results into account, the high-temperature growth (HTG) [123, 124] method was adopted to verify if it is possible to synthesize an h-BN monolayer, similar to what has been done using other precursors without the presence of carbon atoms, for instance, borazine ($B_3N_3H_6$) [60, 109]. For this purpose, Rh(111) was maintained at 1050 K and exposed to a partial pressure of the precursor of 1.4×10^{-6} *mbar* for 3 min. In the sequence, the precursor was pumped out while the substrate was kept at the growth temperature for the next 30 min. These growth conditions were chosen based on previous studies [109] that suggest that high temperatures and low flow of borazine favor the formation of large domains of h-BN on Rh (111). The STM image in figure 4.5a and S3 show a single h-BN domain crossing the crystal steps as a "carpet". In addition, the perfect h-BN nanomesh structure free of defects can be observed in detail in figure 4.5b. In particular, the inset of figure 4.5b displays atomic resolution inside of the so-called "pore region" of the h-BN nanomesh. The nanomesh lattice parameter was found as (3.20 ± 0.03) nm, which is a characteristic value of h-BN on Rh(111) [60, 125], and corresponding with (13×13) unit cells of h-BN on top of (12×12) unit cells of Rh(111).

Table 4.1: Position (binding energy, BE), peak width (full width at half maximum, FWHM), and intensities for the different components contributing to N 1s and B 1s core level peaks for the h-BN/Rh(111) monolayer. The broadening value used was 0.54 eV.

Core Level	Component	BE position [eV]	FWHM [eV]	Area [cps · eV]
$N1s$	N_1	397.90	0.43	558.60
	N_2	398.60	0.43	349.00
$B1s$	B	190.40	0.42	240.10

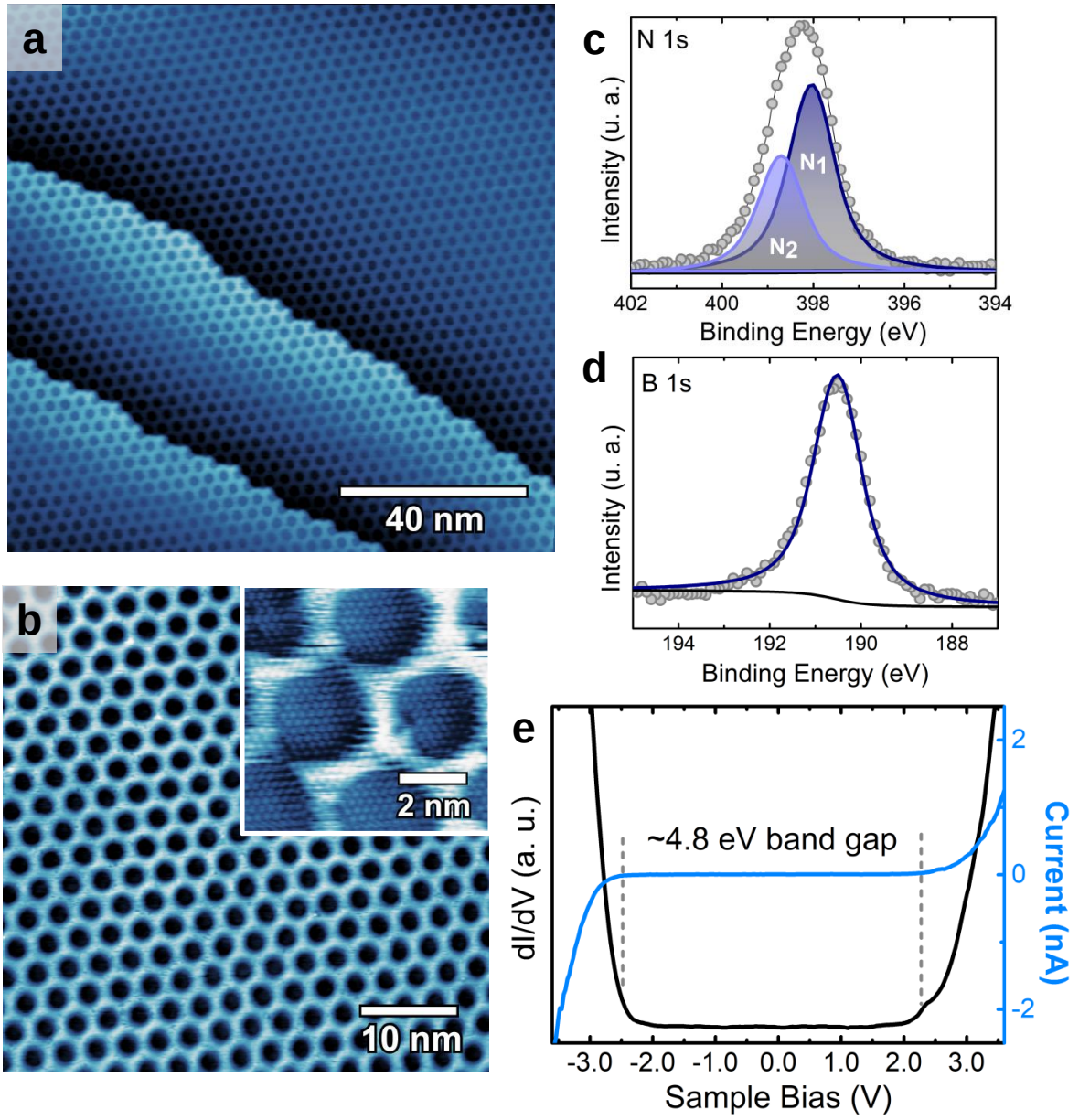

Figure 4.5: h-BN monolayer growth at 1050 K from HMB ($B_3N_3C_6H_{18}$) on Rh(111): (a) STM large scale image, where the monolayer continues over several underlying Rh(111) step edges without any visible domain boundaries (b) STM image of h-BN nanomesh, in the inset an atomic resolution image of pore region is displayed. X-ray photoemission spectra of (c) N 1s and (d) B 1s of h-BN monolayer, acquired at a grazing incidence angle of 60° from the surface normal. The intensity ratio N:B was determined as 1:1. (e) STS (current and differential conductance (dI/dV)) curves of h-BN show a non-conducting region of $\sim$ 4.8 eV. Tunneling parameters: (a) - (b) $V = -0.26\ V$, $I_t = -0.35\ nA$, and inset $V = -0.02\ V$, $I_t = -6.98\ nA$

Figures 4.5c-d show XPS spectra for N 1s and B 1s core level, respectively, obtained after the successful growth of the h-BN monolayer. The intensity ratio N:B was determined as 1:1, which is expected for a perfect h-BN layer. A careful fitting was performed (see table 4.1) for N 1s, resulting in the deconvolution of two chemical components N_1 at $397.90 \pm 0.05\ eV$ and N_2 shifted to higher binding energy $\sim$ 0.7 eV, and an intensity

ratio N_1 : N_2 of 2:1, which agree with other results [126]. These two nitrogen species are associated with the corrugation of h-BN on Rh (111). N_2 is more strongly bound and corresponding to atoms in the pore region, i.e. aligned with the Rh atoms; and N_1 refers to atoms aligned with hollow sites (wire region on the nanomesh) and have a weaker interaction with the substrate. Performing STS measurements on this sample, we obtained curves as the one shown in figure 4.5e, where a band gap value of about 4.8 eV has been determined by direct comparison of the I-V and dI/dV curves [34, 127, 128]. This value is in close agreement with previous studies of the electronic properties of h-BN grown on metals like Cu(111) [129, 130], and Ir(111) [103], where a band gap around 5.0 eV has been found. The band gap value reported for the h-BN monolayer on HOPG [131], as well as, the theoretical predicted for an isolated monolayer is $\sim$ 6.0 eV [132]. h-BN monolayers grown on metallic substrate normally present a band gap reduction, likely due to strong h-BN-substrate interface interaction [112].

4.2 Growth of h-BNC on Ir(111) surface

Due to the carbon dissolution into the Rh(111) substrate at the typical growth temperature (about 1000 K) of h-BN, this surface is not suitable to form hybrid structures using HMB as a single precursor. Hence, we decided to investigate the on surface synthesis on Ir(111) crystal which offers a broader range of growth temperatures for both h-BN and Gr which could also have a huge impact to promote the formation of hybrid materials such as h-BNC alloys. According to previous studies [111, 113–115], Gr usually starts to grow around to 870 K (depending on the source of carbon) and can remain on the surface without notable damages until about 1700 K on Ir(111), being difficult to form iridium carbide. On the other hand, the higher solubility of boron and desorption of nitrogen atoms as N_2 molecule at $\sim$1400 K suggest the low stability of h-BN above this temperature and its subsequent decomposition [104–106, 108, 111] when molecular precursor like borazine is deposited on Ir(111) at RT. However, for growths performed close to this temperature limit, h-BN islands on Ir(111) have shown large size with single orientation [105, 107]. Hence, in order to better understand the adsorption and reaction behavior of HMB on Ir(111) and based on the information discussed above, we performed three growth experiments at different synthesis temperature: 1270 K, 1370 K and 1470 K. Low temperature synthesis were not considered, since a similar

behavior to that exhibited on the Rh(111) surface was expected.

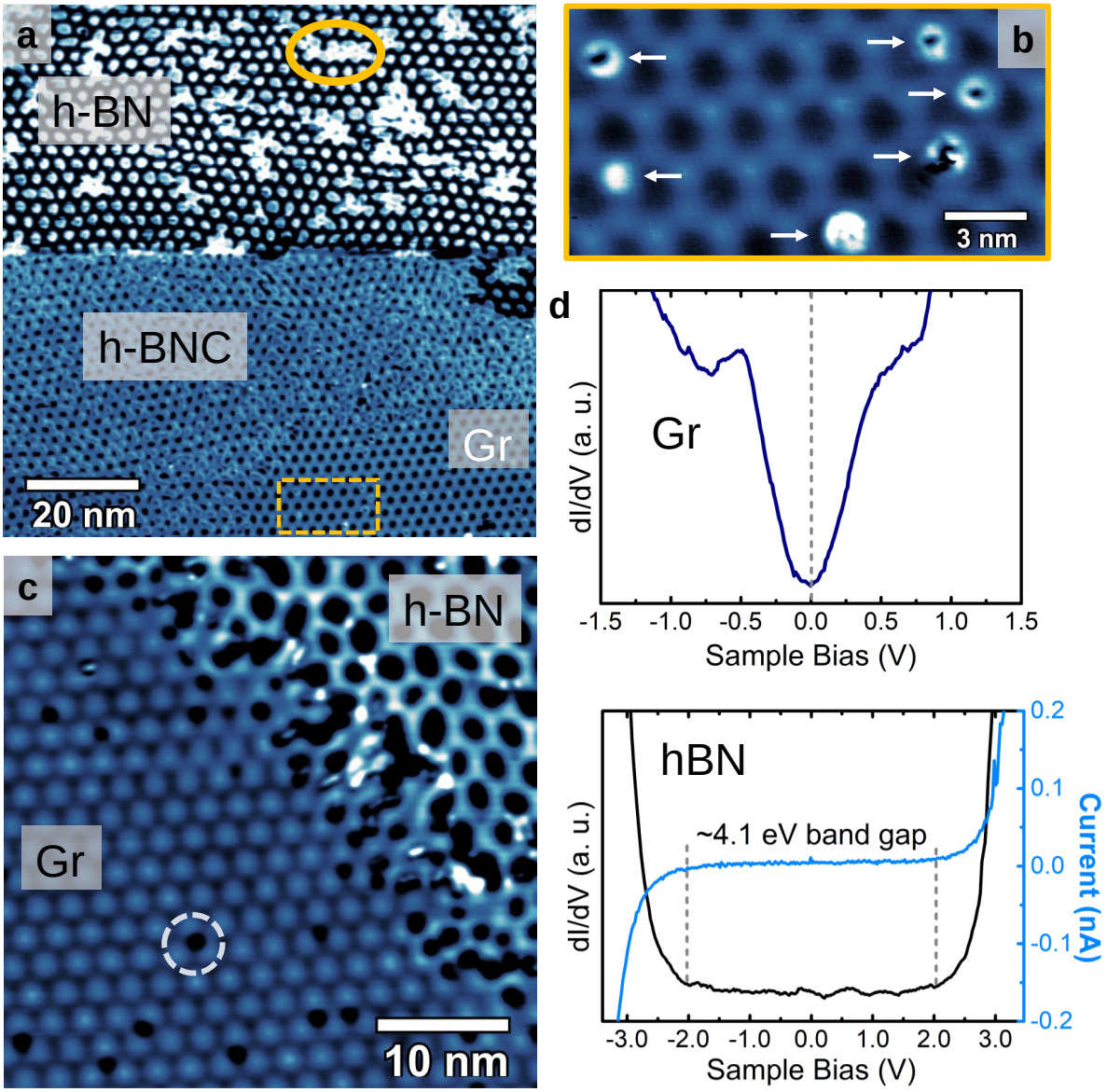

Figure 4.6: Hybrid structures growth from a single novel precursor HMB on Ir(111). (a) STM image of the sample grown at 1470 K evidencing coexisting of three structures present in the sample, where nanographene island are pointed out by a yellow circle into h-BN nanomesh. (b) Zoomed-in STM image of the Gr area indicated by the yellow rectangle in (a), where BN substitutional doping ("BN-nanodonuts")are indicated by white arrows into Gr lattice. (c) Boundary region between Gr and h-BN acquired on the sample synthesized at 1370 K. The black dots in the Gr area (white dashed circle) are also BN-nanoclusters. (d) STS curves acquired on the Gr and h-BN. Tunneling parameters: (a) and (b) $V = 1.09V$ and $I_t = 2.75\ nA$, (c) $V = -1.03\ V$ and $I_t = -0.31\ nA$.

Figure 4.6a shows a general picture of the sample synthesized at 1470 K. It is possible to distinguish unequivocally the co-existing of three areas with different materials. At the top part of the image, we recognize the characteristic feature of the h-BN on Ir(111), being highlighted in yellow some nano islands embedded within the h-BN moiré pattern, even though these bright structures cannot be atomically resolved in the image, they

exhibit clearly a distinct LDOS, presumably due to carbon atoms, i.e. Gr nano islands. At the bottom right part of the figure 4.6a, the Gr moiré pattern can be observed, which presents the well-known dark-atop contrast [133, 134]. In the zoomed-in image (figure 4.6b) of this region (in the yellow rectangle), white arrows indicate the substitutional doping, which are noticed as brighter ring structure. We propose that these specific features corresponding to the presence of BN dopant clusters ("h-BN nanodonut"), since it is expected that B and N atoms tend to form BN pair in stable Gr:BN structures according to theoretical calculations reported in the literature [27, 30, 135–137], where a high energy cost is found to form C–N and C–B bond as compared to that of a B–N bonds. In fact, for systems synthesized under conditions near to B:N$\sim$ 1 it is expected that BN segregates from Gr to form BN regions within the Gr lattice [28, 31]. In the center of the image (see figure 4.6a), we have a hexagonal mixed region that we have identified as BNC structure, which can be considered as an alloy of Gr and BN, or in another words, high-density of dopant "h-BN nanodonuts". A more detailed discussion about their conformation and local electronic properties will be given later.

Figure 4.6c displays a representative STM image of a lateral heterostructure focusing on the boundary region between Gr and h-BN acquired for the sample grown at 1370 K (see also further details in Figure S4). It is worth noting that both sp^2 structures exhibit an inverse contrast in relation to figure 4.6a, allowing us to see the substitutional doping, indicated with a white circle, as dark depressions inside the Gr superlattice. The nature of these superstructures were confirmed by FT (Fourier Transform) calculations of lattice parameter, as well as, by STS measurements. For Gr, the superstructure lattice parameter was determined as $2.47 \pm 0.01\ nm$, which is consistent with published results [113]. STS curves were acquired in areas that seem chemically symmetric and where the BN doping is not present or at least located relatively far away ($\sim 20 \times 20\ nm$) from the inspected region. A representative STS curve taken in an ATOP position on the moiré pattern is shown in figure 4.6d, revealing the V-shape characteristic of the Gr density of states symmetric in relation to the Fermi Level, indicated by the dotted line. The superstructure periodicity obtained for h-BN was $2.91 \pm 0.01\ nm$, which also corresponds to the reported values in literature for h-BN on Ir(111) [105, 108]. The STS result is shown in figure 4.6d, where a band gap of about 4.1 eV is obtained. This value is slightly smaller than the one found above for the h-BN on Rh(111), which could be associated

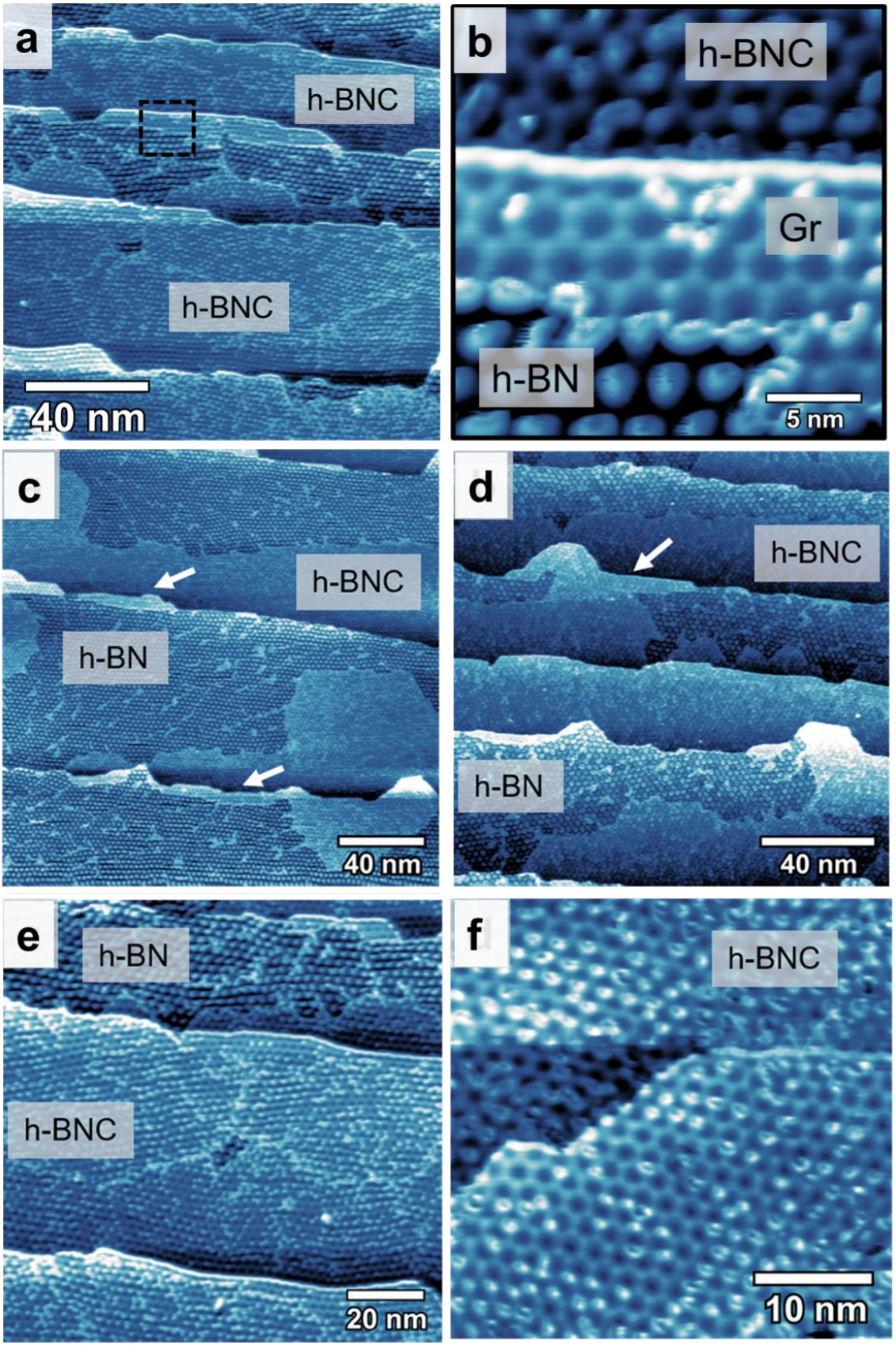

Figure 4.7: (a) Large scale STM image of the sample grown at 1270 K (b) Phase-segregated Gr nanoribbon between h-BNC and h-BN. (c)-(d) Gr-like regions as phase-segregated ribbons are indicated with white arrows. (e)-(f) STM image of h-BNC region, where the BN dopant clusters ("BN-nanodonuts") are clearly observed into the Gr structure. Tunneling parameters: (a) - (b) $V = -0.80\ V$, $I_t = -0.20\ nA$, (c) V=0.88 V and It=0.10 nA, (d) V=1.27 V and It=0.20 nA, (e) =-0.80 V and It=-0.19 nA, (f) V=1.37 V and It=0.24 nA.

to the fact that in this case we did not grow a large h-BN area free of defects. Q. Li and co-workers [129] have demonstrated that some structural defects like grain boundaries can reduce even more the bang gap in h-BN monolayers.

In contrast with two samples synthesized at higher temperatures (1470 K and 1370 K), the sample obtained at 1270 K did not show large pristine Gr areas, instead of that, extensive areas of h-BNC are formed, as depicted in a representative STM image in figure 4.7. Moreover, one observes some Gr-like regions as phase-segregated ribbons located at the boundary of domains. In the zoomed-in image (figure 4.7b) we recognized a strip of Gr, which has a width of $9.1 \pm 0.8\ nm$ and can describe as a nanoribbon (GNR) embedded between two different regions, h-BNC and h-BN.

According to these results, the h-BNC structure was observed for all growth conditions performed in this study at different temperatures. However large domains of the ternary alloy were identified exclusively at 1270 K. Moreover, in this case the BN substitutional doping, "h-BN nanodonut", shows a more regular size. In this context, we focused the study of this novel structure on the sample grown at the lowest temperature. Figure 4.8a displays large scan size STM image of h-BNC. In the inset image is shown a magnified view of the square-enclosed region, where it is pointed out a "h-BN nanodonut". The lattice parameter found for BNC super structure is (2.50 ± 0.05) nm, which indicates that the Gr moiré lattice parameter is preserved along the alloy. A close inspection of STM images reveals that BN doping clusters have a tendency to form in hcp-type and fcc-type region on Ir(111) [138], where the interaction of the Gr with the substrate is stronger. The same behavior of selective doping region can be also identified more clearly (black circular holes) in the other Gr contrast shown in figure 4.6c. Balog *et al.* [139] observed a similar tendency in the hydrogen adsorption on Gr/Ir(111) when this substrate was exposed to atomic hydrogen at very low dose. In figure 4.8b both the Gr honeycomb lattice and the moiré superstructure are evident. The lattice constant of Gr was determined by FT having as result 2.46 ± 0.06 Å. Under these specific measurement conditions, the BN cluster are imaged like holes into the lattice. In order to shed light on the atomic structure of the alloy and propose a geometry for BN motifs, we superimposed the honeycomb Gr lattice on the topographic image (figure 4.8b) resulting in figure 4.8c, where regions associated with the dopant are indicated with white arrows. A height profile along the marked line in figure 4.8b is shown in figure 4.8d, the full width at

half maximum (FWHM) was found as (0.49 ± 0.07) nm, which suggests that the dopant regions are constituted by at least $(BN)_8$ units arranged as can be seen in the figure 4.8e. For low concentration of BN, it is possible that a small amount of BN clusters are substituting in-planar the Gr lattice. A systematic investigation of the STM images demonstrate that these "h-BN nanodonuts" are extremely regular in shape and size, even if, in some regions they appear distorted due to the interconnection of neighbour "h-BN nanodonuts".

This experimental finding suggest that a optimal size for this nanocluster of BN dopant is obtained during the present synthesis. Ren *et al.* [21, 137] found that six-fold BN rings are the most favorable structure in BN-doped Gr when compared to other explored motifs like dimer or chains, this is supported by the fact that six-fold rings of BN are more suitable for π bonding. Fan *et al.* [140] also calculated the formation energies of BN clusters with different sizes, ranging from a single BN unit to $(BN)_{12}$, obtaining that domains of $(BN)_{12}$ are energetically more favorable than smaller clusters. Other theoretical studies based on the energetic and structural stability of different motif in this kind of 2D structures can be found in [32, 141]. Therefore, we consider all the theoretical prediction described in the mentioned references to support our interpretation for results in figure 4.8, where few BN units (at least 8) are forming clusters inside the Gr lattice. On the other hand, some studies [21, 137] have indicated that CVD growth technique are not suitable for synthesizing non-phase-separated BNC alloys. In fact, they recommend to use deposition techniques such as electron-beam-bombardment. The present work demonstrates that for the particular precursor used a h-BNC alloy can be successfully prepared by the CVD method.

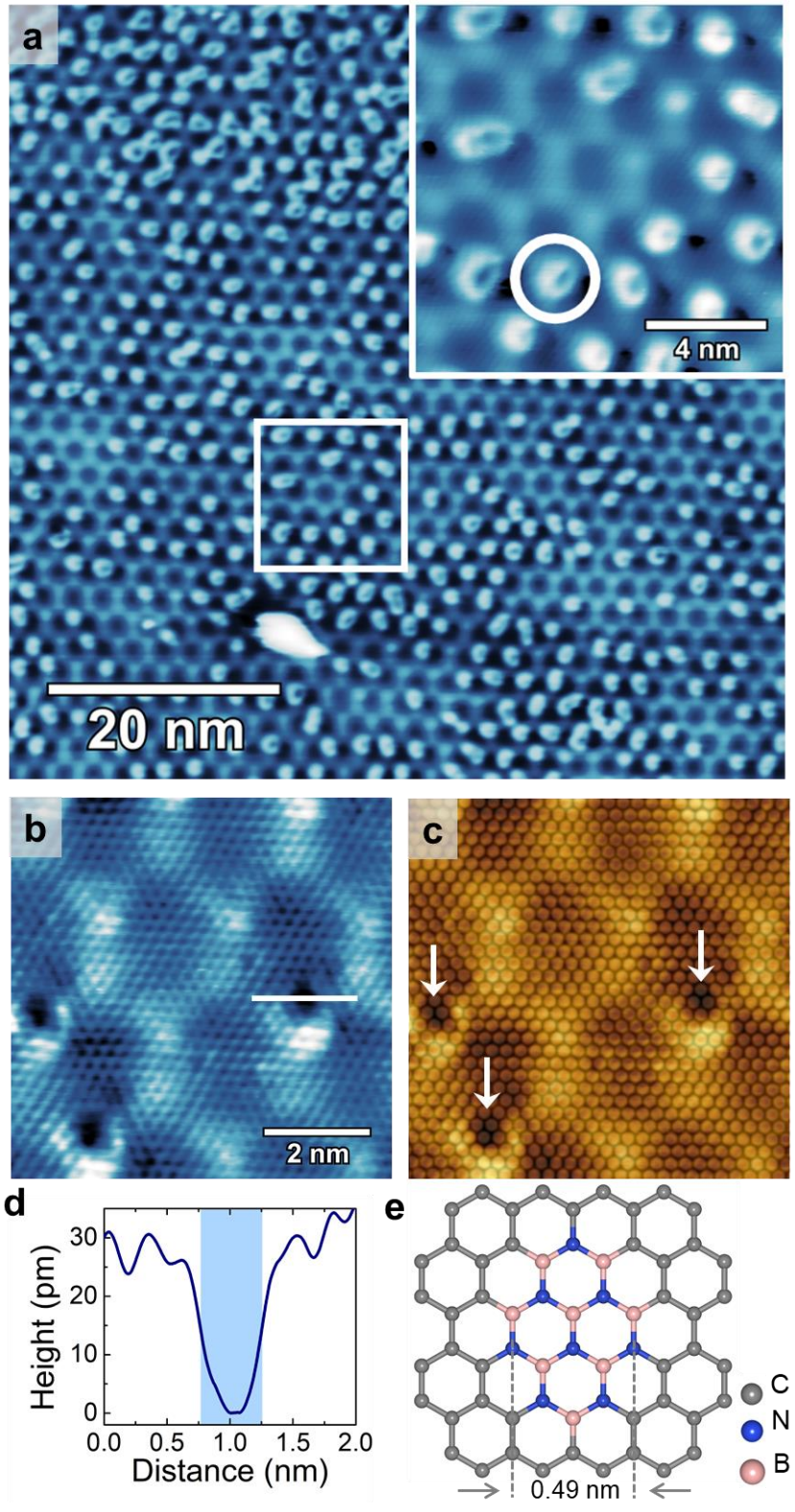

Figure 4.8: h-BNC conformational structure: (a) STM large scale image, with the inset highlighting the Gr structure doped by the "h-BN nanodonuts". (b) Atomic resolution image of the h-BNC, where it is evident the honeycomb structure of Gr. (c) Superimposed the honeycomb Gr structure on the topographic image in (b), white arrows indicating the BN domains. (d) Height profile along the BN cluster in (b), where the shaded area shows the FHWM of the profile. (e) Atomic model of the Gr doped with a small BN cluster. Tunneling parameters: (a) and inset $V = -1.00\ V$, $I_t = -0.20\ nA$, (b) $V = -0.80\ V$, $I_t = -0.25\ nA$

To further support our proposed geometry for the "h-BN nanodonuts", we simulated STM images based on the density functional theory (DFT) and the Tersoff-Hamann [142, 143] approach for height-constant mode. In the simulations presented here the Ir substrate was not included. Despite the importance of the interaction of Gr with the Ir(111) surface, as observed by the moiré superstructure in the experimental STM images, a weak interaction of Gr with the substrate justifies our approach [144]. Figure 4.9 shows the simulated STM images. Four "h-BN nanodonuts" models were tested for V_{bias} of -1 V and +1 V (sample bias). The BN structures that replace the C atoms in the Gr layer are $(BN)_3$ (Fig. 4.9(a-c)), B_6N_7 (Fig. 4.9(d-f)), $(BN)_8$ (Fig. 4.9(g-i)) and $(BN)_{12}$ (Fig. 4.9(j-l)). These models were chosen because they are the ones with the shape and size most consistent with the experimental results. The region within the "h-BN nanodonuts" has a low calculated STM electronic density (ρ_{STM}) for the sample bias investigated. However, for both -1 V and +1 V sample bias, there is a high ρ_{STM} in the region between the BN cluster and the C atoms, mainly for the B–C bonds, confirming the "donut" structure observed in the experimental images. The structures $(BN)_3$, B_6N_7 and $(BN)_{12}$ are more circularly symmetrical compared to the elongated shape of $(BN)_8$. Moreover, there is an asymmetry in the ρ_{STM} for the $(BN)_8$, with a high intensity on the side of the BN cluster with more B–C bonds. These features are compatible with the observed experimental results, as it is clearly seen in figures 4.6b and 4.9b, and corroborate with our proposed model for the "h-BN nanodonuts" as $(BN)_8$ clusters embedded in the Gr layer at very specific positions within the moiré superstructure. It is important to stress that such asymmetric shape in the STM images are not a measurement artifact, since we have confirmed these structures several times and in several samples by changing the scanning directions in the microscope.

To analyse the chemical state of the B, C, and N atoms, the N 1s, B 1s and C 1s core level XPS spectra obtained for the sample growth at 1270 K are shown in figure 4.10a. The experimental data exhibits slightly asymmetric peak shape along with large FWHM, which reveals the presence of multiple chemical states in each core level peak. We fitted the raw data using Voigt-like functions in the Gaussian limit, after subtracting a Shirley-type background. The experimental broadening, related to the Gaussian contribution has a FWHM fixed to $\sim$0.6 eV (which was previous determined). Moreover, the fitting was performed under the constraints of equal FWHM for the components of the same

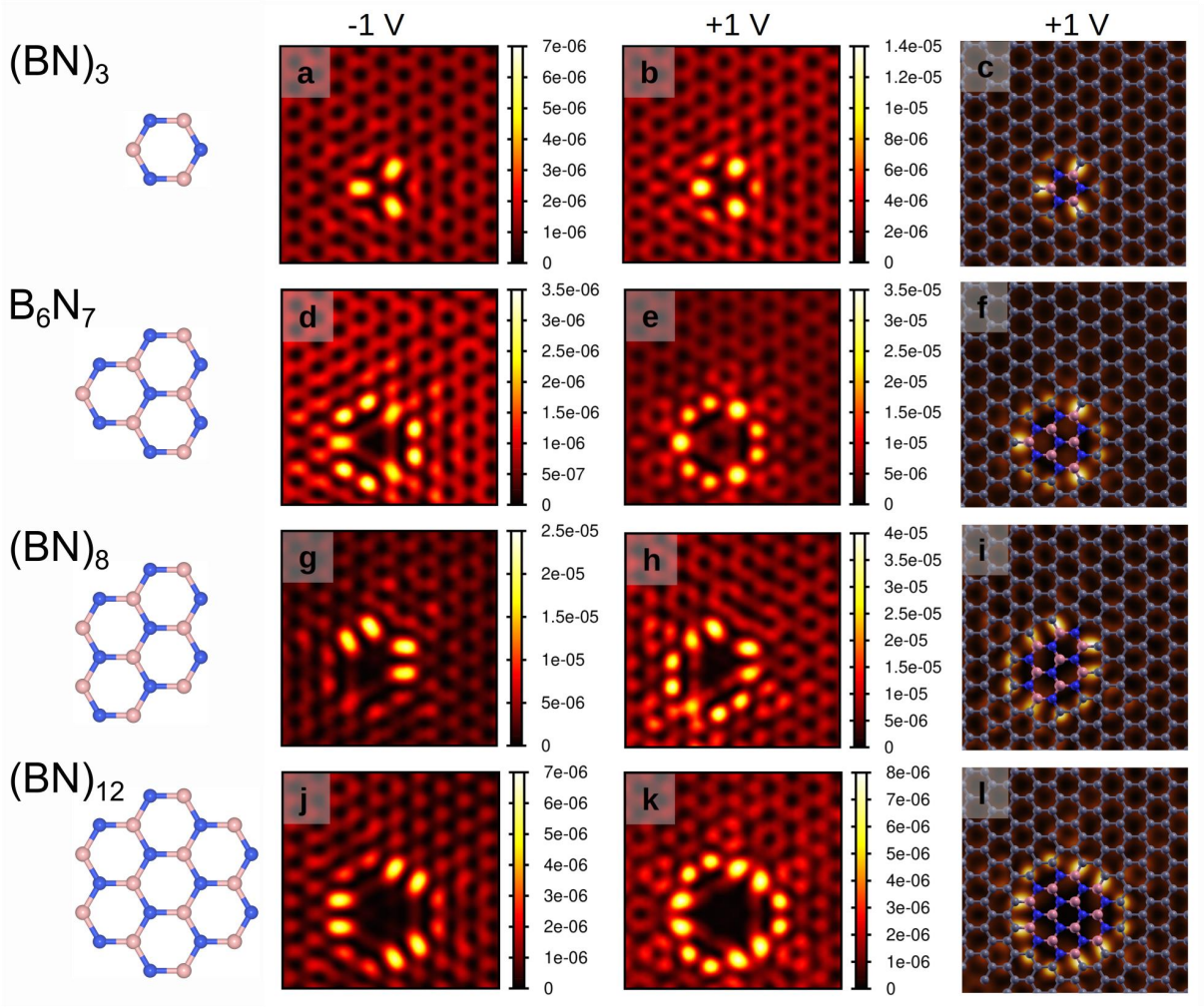

Figure 4.9: Simulated STM images (21 × 21 Å) representing the electronic density ρ_{STM} for clusters of BN embedded in a Gr layer. The left panels are for V_{bias} = -1 V. The center panels are for V_{bias} = +1 V. The right panels are for V_{bias} = +1 V with the structural model superimposed. The coloring of atomic species is as follows: N atoms in blue, B atoms in salmon, and C atoms in gray. The "h-BN nanodonuts" are: (a-c) $(BN)_3$, (d-f) B_6N_7, (g-i) $(BN)_8$ and (j-l) $(BN)_{12}$. ρ_{STM} is given in units of electrons/a.u.^{3}. Credit: Luis Herique de Lima

element (see table S2). N 1s core level was fitted with two peaks, a main peak (N_0) at $397.50 \pm 0.05\ eV$ and second weaker component (N_C) at $398.40 \pm 0.05\ eV$. Likewise, a multi-peak fitting was performed on the B 1s core level, obtaining the most intense component (B_0) at $190.10 \pm 0.05\ eV$ and the other one (B_C) at $189.60 \pm 0.05\ eV$. The position of the peaks identified as N_0 and B_0 are in excellent agreement with the reported values for h-BN on Ir(111) [103, 105]. The peak at higher binding energy on N 1s (N_C) is assigned to contributions from N–C bonds since C atoms are more electronegative than B, which implies an increase in the binding energy. For B 1s, B_C is located at a lower binding energy, considering again the electronegativity of C compare with N, this peak is associated with B–C bonds. For C 1s core level three peaks can be distinguished.

In addition, it was found a similar intensity ratio for N_C/N_0 and B_C/B_0 of 8:25 and 19:50 respectively. The dominant component, C_0 at $284.00 \pm 0.05\ eV$ is assigned to sp^2 hybridized C atoms in pristine Gr on Ir(111) [145, 146]. The small shoulder at lower binding energy ($283.10 \pm 0.05\ eV$) is attributed to C–B bounds, whereas the other peak at higher binding energy ($284.70 \pm 0.05\ eV$) is assigned to C–N bonds. The chemical analysis above gives support to the formation of h-BNC ternary alloy on Ir(111) surface and it is coherent with our proposed structure consisting of a Gr lattice doped with a small cluster of BN, where C–B and C–N bonds are located at the boundaries of the dopant, being found a relative concentration between C_B and C_N of $\sim$ 1:1. From XPS data it is also identified the formation of h-BN segregated from the alloy, as observed in the STM images shown in this work. It is clear that a rigorous chemical composition of the alloy is not achievable due to limitations of the XPS measurements, for instance the low photoemission cross sections for the core levels explored here, as well as the low-energy resolution provided by the non-monochromatic Mg K_α source. Moreover, there is one intrinsic difficulty to separate the BN contribution from h-BN segregated islands from the "h-BN nanodonuts" using XPS. We might overcome this problem by a careful statistical analysis of the BN:C concentration in the h-BNC by counting the BN clusters on the STM images.

Table 4.2: Position (binding energy, BE), peak width (full width at half maximum, FWHM), and intensities for the different components contributing to N 1s, B 1s and C 1s core level peaks for the sample grown at 1270 on Ir(111). The broadening value used was 0.54 eV.

Core Level	Component	BE position [eV]	FWHM [eV]	Area [cps · eV]
$C1s$	C_0	284.00	0.14	129.50
	C_B	283.10	0.15	20.50
	C_N	284.70	0.15	18.20
$N1s$	N_0	397.50	0.43	213.90
	N_C	398.4	0.43	68.50
$B1s$	B_0	190.10	0.42	156.20
	B_C	189.60	0.42	59.30

Figure 4.10b shows a representative STM image of h-BNC region. Based on our analysis and considering one area of $25 \times 25\ nm^2$, we estimated a BN concentration of about 17%. Since the sample did not grow homogeneously across the crystal, it is not possible to extend this concentration value for the whole sample. In this region, the LDOS by

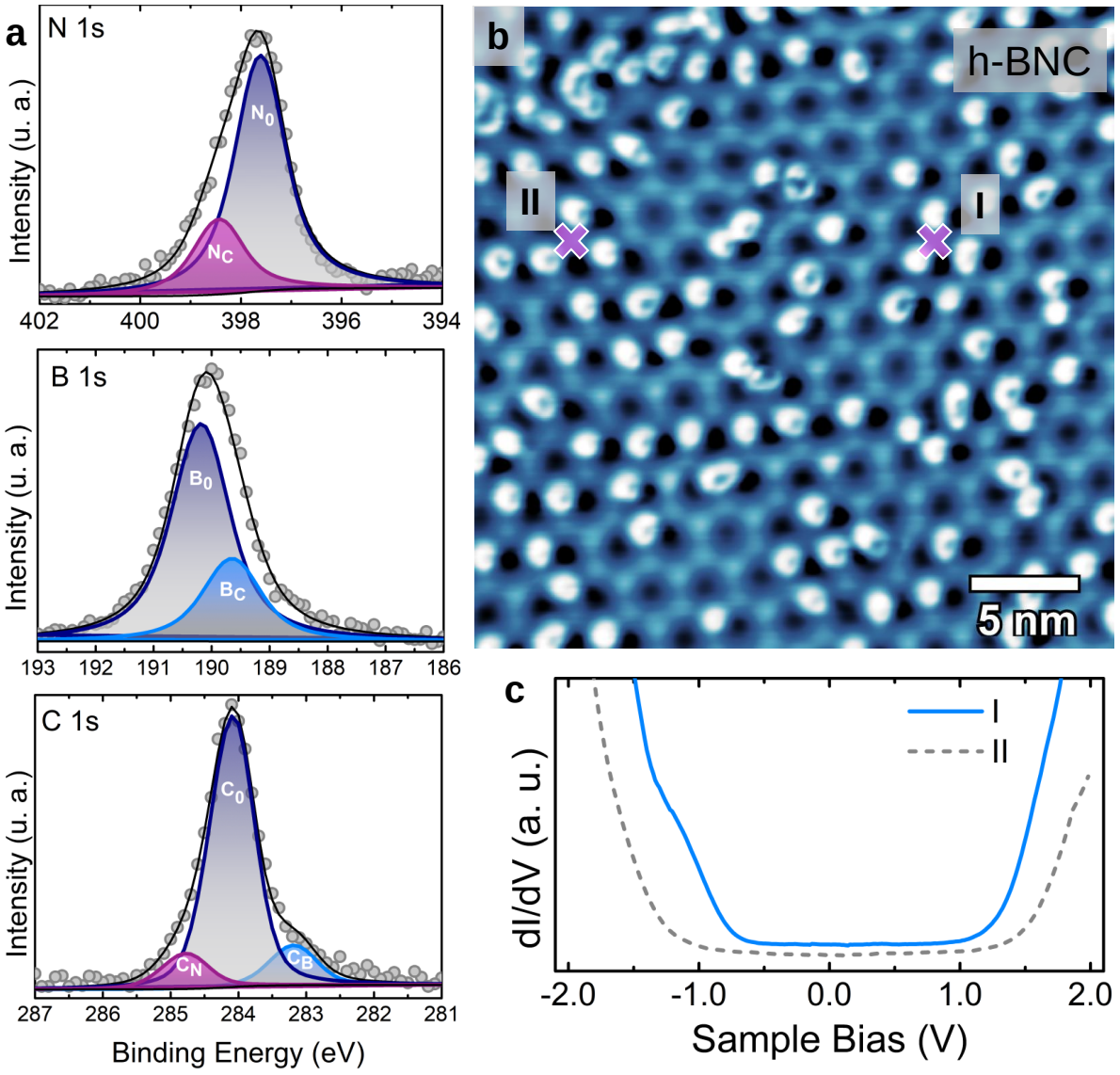

Figure 4.10: a) N 1s, B 1s, and C 1s X-ray photoemission spectra of the h-BNC monolayer prepared on Ir(111) at 1270 K. XPS spectra were acquired using Mg K_α at a grazing incidence angle of 60° from the surface normal. b) STM image of h-BNC alloy. c) STS curves taken on C regions surrounding by doped domains, indicated with the x. Tunneling parameters: $V = -1.10\ V$, $I_t = -0.24\ nA$

STS was examined given as more representative results the spectra displayed in figure 4.10c, these STS curves were acquired around the "h-BN nanodonuts". It is important to note that the spacial resolution and locality of STS make it one of the most suitable technique to explore the electronic structure of the h-BNC alloy characterized by a low BN segregation in the Gr lattice located into a highly heterogeneous sample, unlike other techniques such as angle-resolved photoemission spectroscopy (ARPES), which has been the most employed tool to investigate the band gap opening in Gr and given a global measurement of the band structure [5]. Otherwise, as predicted by theoretical calculations the introduction of BN domains in the carbon lattice breaks the potential

symmetry leading to the redistribution of charge near the Dirac points and the band gap opening. For the area shown in the figure 4.10b we have estimated a band gap between 1.4 and 1.6 eV, curve I and II respectively. Despite, band gap values for h-BNC structures determined by computational models depend on both the stoichiometry of the alloy and the concentration of BN and carbon atoms, our result is consistent with predictions [28, 140] made for some BNxCx-1 materials. In addition, these values are inside the band gap range determined for similar samples by means of optical spectroscopy [147, 148]. However, a careful study of the band gap opening and the determination of the band gap value for this structure is desired in further investigations, for instance employing low-temperature STS or nano-ARPES measurements [149, 150].

4.3 Conclusions

In this work we have used the unexplored precursor hexamethyl borazine (HMB) to successfully grown epitaxial h-BN, hybrid lateral junctions of h-BN and Gr, as well as the h-BNC alloys on Ir(111) by using conventional CVD methods. The combination of substrate and the correct temperature window plays an important role on growing h-BNC. In one hand, Gr can be efficiently grown on Rh(111) at low temperatures (∼900 K), while h-BN is formed only above 1000 K. However at such a high temperatures C strongly dissolves into the Rh bulk, thus the coexistence of h-BN and Gr is very difficult in such a substrate, remaining only perfect h-BN monolayer on Rh(111). On another hand, C has a very low dissolution into Ir(111) and Gr is efficiently formed at much higher temperatures (above 1200 K) being very stable until temperatures like 1700 K. Similarly h-BN starts to efficiently grow on Ir(111) at temperatures like 1100 K and remains stable up to temperatures ∼1400K. Therefore we have a large growth window to produce h-BN and Gr as well as induce the h-BNC alloy formation in the interval of 1200 K - 1500 K, where lower temperatures will promote h-BN and higher temperatures Gr. For all ranges of temperatures investigated in the present work we found the formation of h-BNC on Ir(111). Using atomic resolution STM images combined with DFT calculation we have demonstrated that h-BNC is formed by doping Gr with small BN nanoclusters. Theoretical predictions by Fan *et al.* [140] suggested that $(BN)_{12}$ clusters are energetically favored. The atomic resolved STM images revealed a predominance of an asymmetric density in the image constrast around

the BN nanoclusters (BN "nanodonuts") that DFT calculations associates to $(BN)_8$. Moreover, the BN-nanocluster is preferentially formed only in the fcc- and hcp-type regions of the Gr moiré pattern on Ir(111) as defined by N'Diaye *et al.* [138]. Therefore we might speculate that such a preferential "formation sites" would limit the density of BN-cluster on Gr, leading to an extra-control on the band gap value, which might be optimized on a fine tuning of the growth conditions and substrate, for instance, on Ir alloys.

Chapter 5

Hierarchical Synthesis of 1D and 2D Porphyrin MOFs on Ag(100)

In this chapter, we show the on-surface synthesis of organometallic molecular chains and porous networks from the free-base 5,10,15,20-tetrakis(4-bromophenyl)-porphyrin (H_2TBrPP) on Ag(100). Different molecular nanostructures could be hierarchically produced upon substrate temperature. For the first time, the so-called "inverted" conformation [87] was observed in molecular chains on Ag(100). This conformation was observed previously only on Cu(111) surface [151–155]. Moreover, we demonstrate the temperature selectivity between the two molecular conformations, "inverted" versus "saddle". The adsorption configuration of the H_2TBrPP molecules has been investigated on Ag(100) in a comprehensive multi-technique approach (experiment and theory) using scanning tunneling microscopy (STM) and X-ray photoelectron spectroscopy (XPS) as well as density functional theory (DFT). The numerical calculations were carried out by Prof. Duncan John Mowbray and Prof. Alejandro Pérez Paz.

5.1 On-surface self-assembly and organometallic motifs at RT

The absorption of H_2TBrPP onto clean Ag(100) surface at room temperature (RT) and submonolayer coverage was studied. After deposition, molecules adopt different configurations on the surface. Figure 5.1a shows short-range supramolecular self-assembly. Adjacent molecules adopt clearly two different orientations, which lead to define two overlapping ordered structures organized in an square unit cell with an internal angle of $\theta_a = \theta_b = (89 \pm 2)^\circ$ and lengths of $a_1 = a_2 = b_1 = b_2 = (2.36 \pm 0.05)\, nm$. Both lattices deviate by $(30 \pm 2)^\circ$ from the <110> high symmetry directions of the Ag(100) substrate. The main molecular axis is indicated by yellow lines in figure 5.1b, molecules labeled as I are rotated by 15° clockwise from <110>, while molecules labeled as II are at 90° of the first one. In halogenated molecular assemblies focused on close-packed (111) metal substrate [156, 157], the molecules usually are aligned with the surface crystallographic directions here the influence of the Ag(100) substrate symmetry is indicated by the deviation of porphyrins. The self-assembly is likely stabilized by means Br$\cdots$Br and Br$\cdots$H lateral interactions such as has been already reported for 2D halogen bonded networks using brominated functional groups [76, 158, 159].

Moreover, STM images (see figure 5.1 c-d) show triangular and square pores and other less frequent motifs such as hexagonal and pentagonal pores. Irregular structures are also observed on the sample. All these motifs are connected by Ag adatoms, which exhibit higher apparent height in the images. The coexistence of the self-assembled arrangement, found in lower proportion on the sample, and the different organometallic C–Ag–C networks suggests partial dehalogenation of the H_2TBrPP at RT. This is consistent with the previous bottom up synthesis using precursors containing C–Br bonds on Ag(100) [80, 159, 160], where almost complete debromination of the molecules under similar conditions were reported.

In order to gain insight into this matter, XPS measurements were performed after the STM measurement. The Br $3p_{3/2}$ core level spectrum is displayed at the top of the figure 5.2. The single peak is located at $181.73 \pm 0.05\ eV$. To correctly interpret our results, we performed additional XPS measurements at multilayer coverage to guarantee the presence of H_2TBrPP intact molecules, i.e., C–Br bonds. Figure 5.2 (bottom) clearly

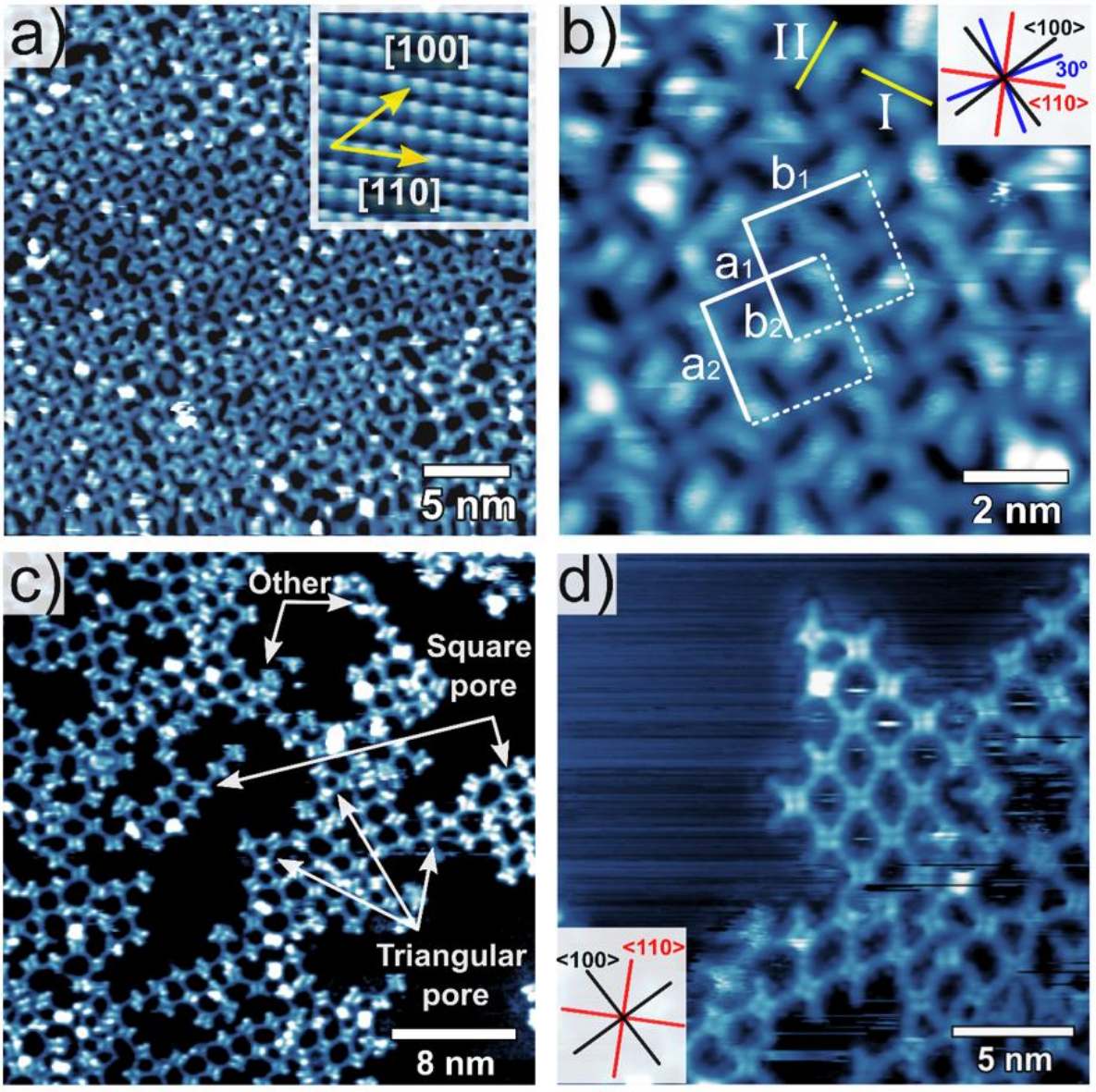

Figure 5.1: Self-assembled islands and surface-assisted synthesis of H_2TBrPP molecules on Ag(100) at RT. (a) Long-range and (b) close-up STM images of an island formed by halogenated porphyrins. Atomic resolution STM image of clean Ag(100) substrate is displayed in the inset image in (a), where the high symmetry directions of the crystal are indicated (details in the text). (c) Overview and (d) high-resolution STM image of different organometallic motifs formed from debrominated porphyrins at RT, emphasizing triangular and square pores. In (d) small dots around the molecular motif are identified as cleaved Br atoms.

shows the presence of two different brominated species: one at $181.70 \pm 0.05\ eV$ and another at $183.90 \pm 0.05\ eV$. The binding energy separation between these components is in perfect agreement with previous studies [80, 161], where the peak at higher binding energy is attributed to Br–C bonds, whereas the peak at lower binding energy is assigned to Br-Ag bonds.

In this manner, we confirm that the energy of the Br $3p_{3/2}$ at the submonolayer

regimen corresponds to the metal-bonded species, indicating that most of the molecules debrominate upon adsorption at RT and Br atoms remain on the surface. On the other hand, in our data, a photoemission signature for C–Br bonds is not perceptible, which does not rule out the presence of these bonds. It is feasible that due to the low debromination barrier of Ag(100) compared to other more densely packed and lower reactivity substrates such as Ag(111) and Au(111), XPS measurements promote the cleavage of C-Br bonds. Indeed, the tiny dots around adsorbates (figure 5.1d) are identified as Br adatoms [155]. As expected, these protrusions are absent for the self-assembled, forming by halogenated porphyrins.

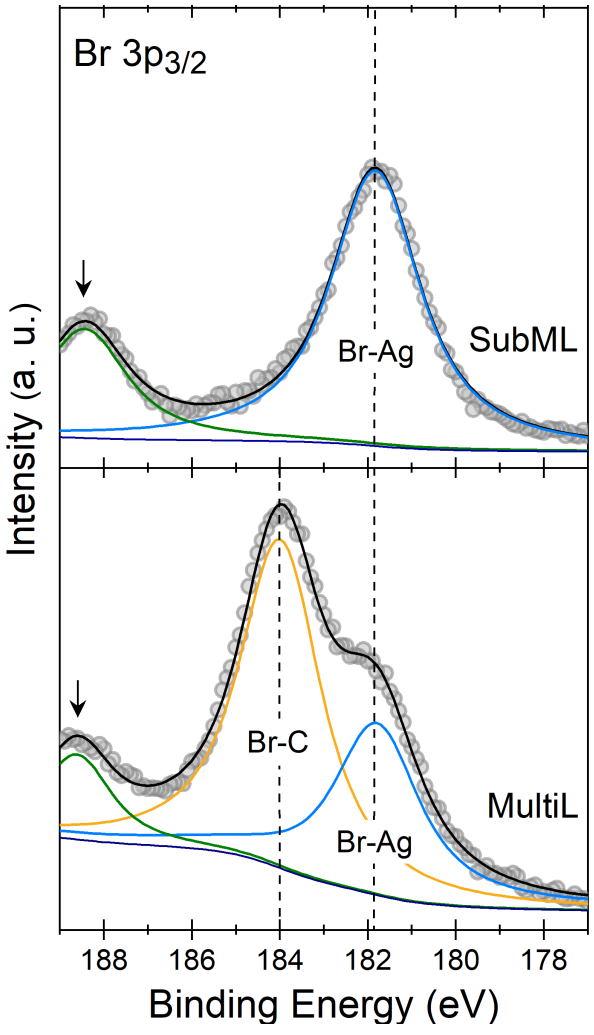

Figure 5.2: Br $3p_{3/2}$ core-level XPS spectrum for submonolayer (SubML) and multilayer (MultiL) H_2TBrPP deposition on Ag(100). The arrows designate the beginning of the Br $3p_{1/2}$ peak.

In order to continue exploring the reaction pathway on the surface, a new sample was prepared at RT, and subsequent annealings at 350 K for different intervals of time were carried out. Such as one can see in figure 5.3 all organometallic networks observed

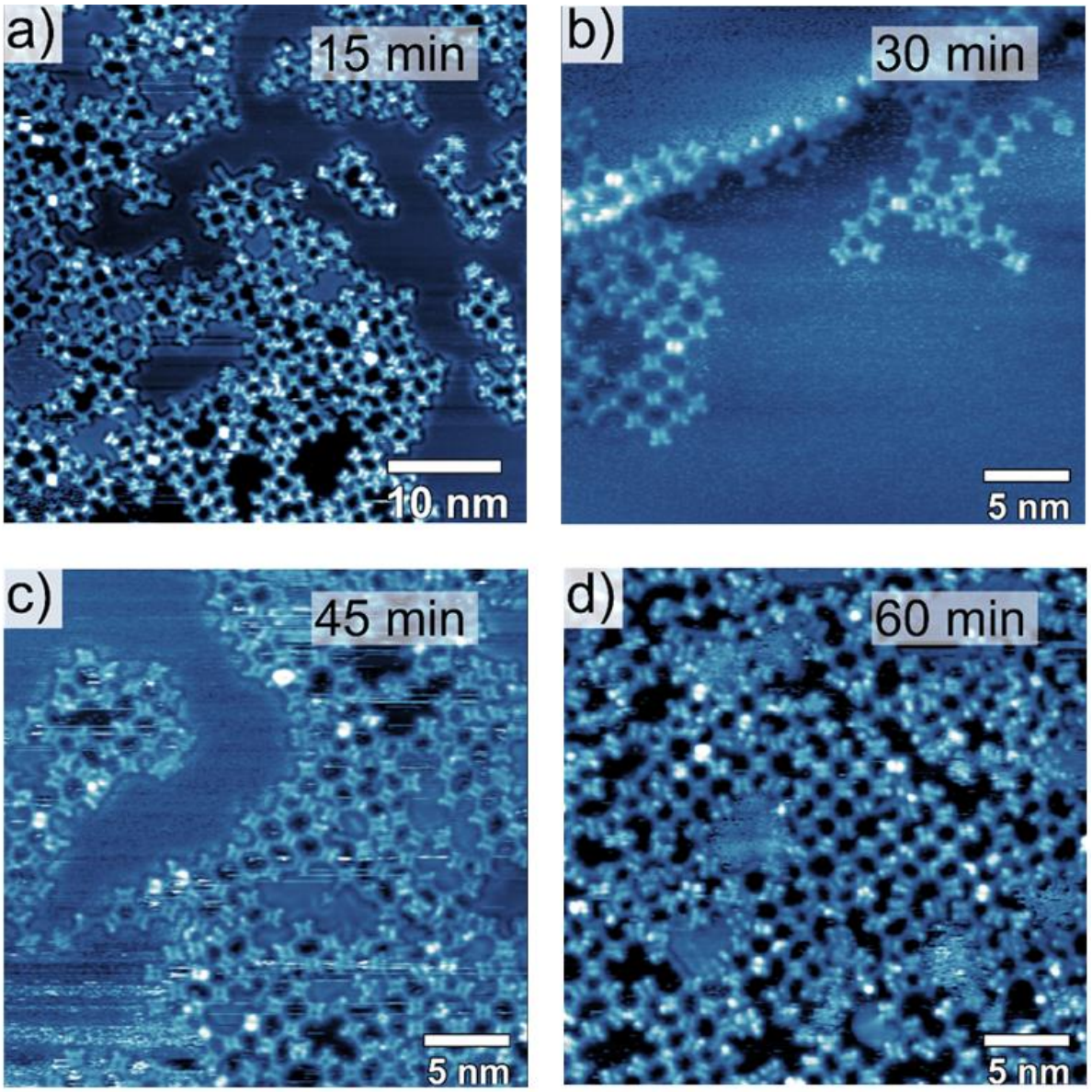

Figure 5.3: Representative STM images of the sample after thermal treatment at 350 K for (a) 15 min, (b) 30 min, (c) 45 min, and (d) 60 min. e) Normalized motif distribution for the polymerization process at RT and each subsequent annealing at 350 K for different intervals.Tunneling parameters: (a) $V = -1.20\ V$, $I_t = -1.95\ nA$, (b) $V = -0.80\ V$, $I_t = -0.35\ nA$, (c) $V = -1.25\ V$, $I_t = -0.21\ nA$, and (d) $V = -1.06\ V$, $I_t = -0.14\ nA$.

at RT are present on the substrate regardless of the exact thermal treatment. To quantify these motifs as function of the annealing conditions, over 30 STM images were statistically analyzed. The normalized distribution of each motif (including supramolecular arrangements) is depicted in figure 5.4. To reduce the influence of sample inhomogenity, STM images acquired in different sample areas were used. Based on the statistical analysis, the self-assembly is not observed after the first annealing at 350 K for 15 min, which shows the full debromination of the molecules [160]. However, a drastic influence of the temperature on the well-defined metal-coordinated polymers (C–Ag–C)

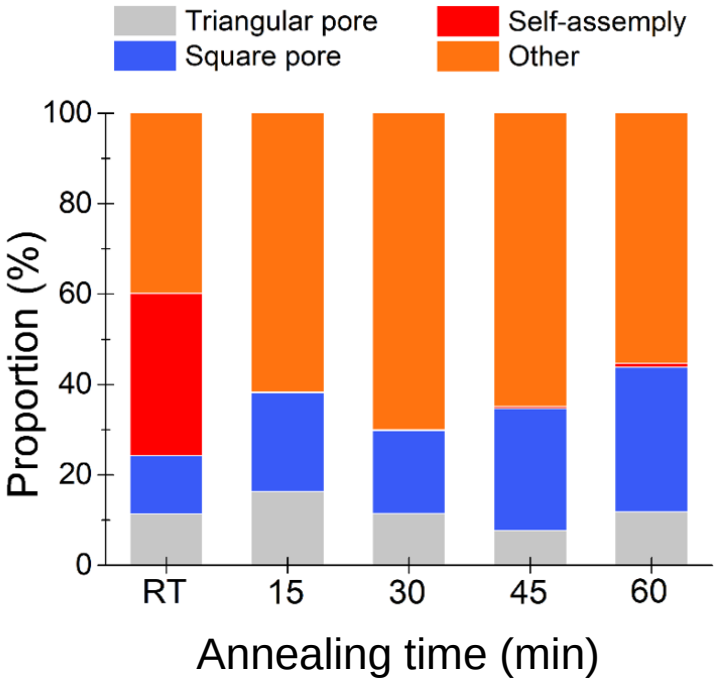

Figure 5.4: Normalized motif distribution for the polymerization process at RT and each subsequent annealing at 350 K for different intervals of time.

is not noticed, finding disordered motifs (named as other in figure 5.4) in the majority proportion for all thermal treatments.

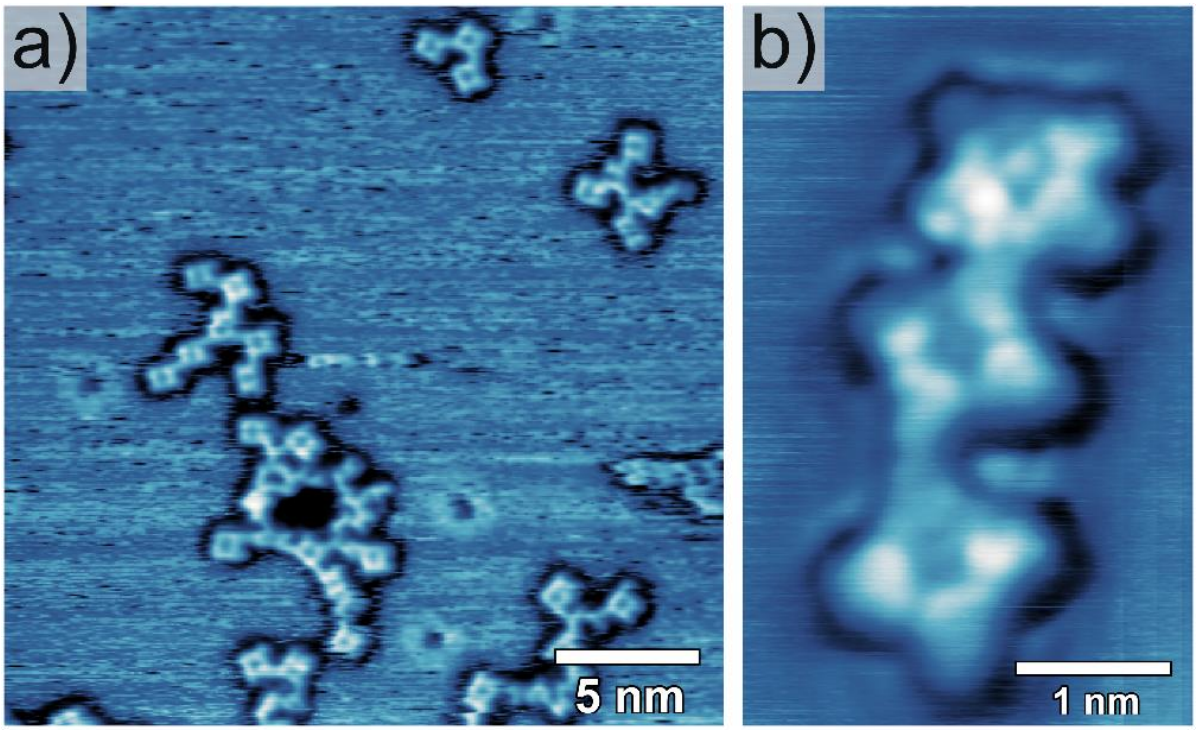

Figure 5.5: STM images of covalent coupling between the molecules promote by thermal annealing at 450 K for 10 min. Tunneling parameters: (a)-(b) $V = -0.80\ V$, $I_t = 0.35\ nA$.

On Ag(100), the formation of covalent structures via Ullmann coupling reaction has been reported after annealing at 550 K, for instance, using 1,3,5-tris(3-bromophenyl)benzene as a molecular precursor [160]. In order to avoid molecular degradation, we applied soft annealing at 400 K for 120 min. However, significant structural modifications were not induced on the sample. This result proves the organometallic structures' stability without achieving a covalent linking, which is a fundamental condition for future applications in electronic and sensor devices. On the other hand, as shown in figure 5.5, important changes were recognized after annealing at 450 K for 10 min, which consists of the demetalating C-Ag-C bonds into C-C bonds without preserving the 2D organometallic networks. This arrangement closely resembles the H_2TBrPP covalent assembly on Au(111) reported by Grill *et al.* [78].

5.2 On-surface synthesis of square pore networks and molecular chains controlled by substrate temperature

To date, few studies have concentrated their attention on the role of precursor depositions onto preheated substrates. Remarkable results reported by *Cirera et al.* [162] show the thermal selectivity between intra- and intermolecular coupling processes for tetra-aza-porphyrin derivatives on Au(111). Moreover, controlling the polymerization degree by tunning substrate temperature during deposition has been reported [18, 163–165]. To elucidate the influence of substrate temperature on the selectivity of reaction pathways in our system, H_2TBrPP were deposited on clean Ag(100) held at 350 K, 390 K, 450 K, and 510 K, being the initial coverage and sublimation rate comparable for all experiments. STM images (figures 5.6) reveal relevant morphological differences between the nanostructures. In particular, at 390 K and 450 K the synthesis of organometallic chains of molecules is promoted. This new motif is not observed from RT deposition followed by annealing treatments, which suggests that the substrate temperature is inducing a new synthesis path.

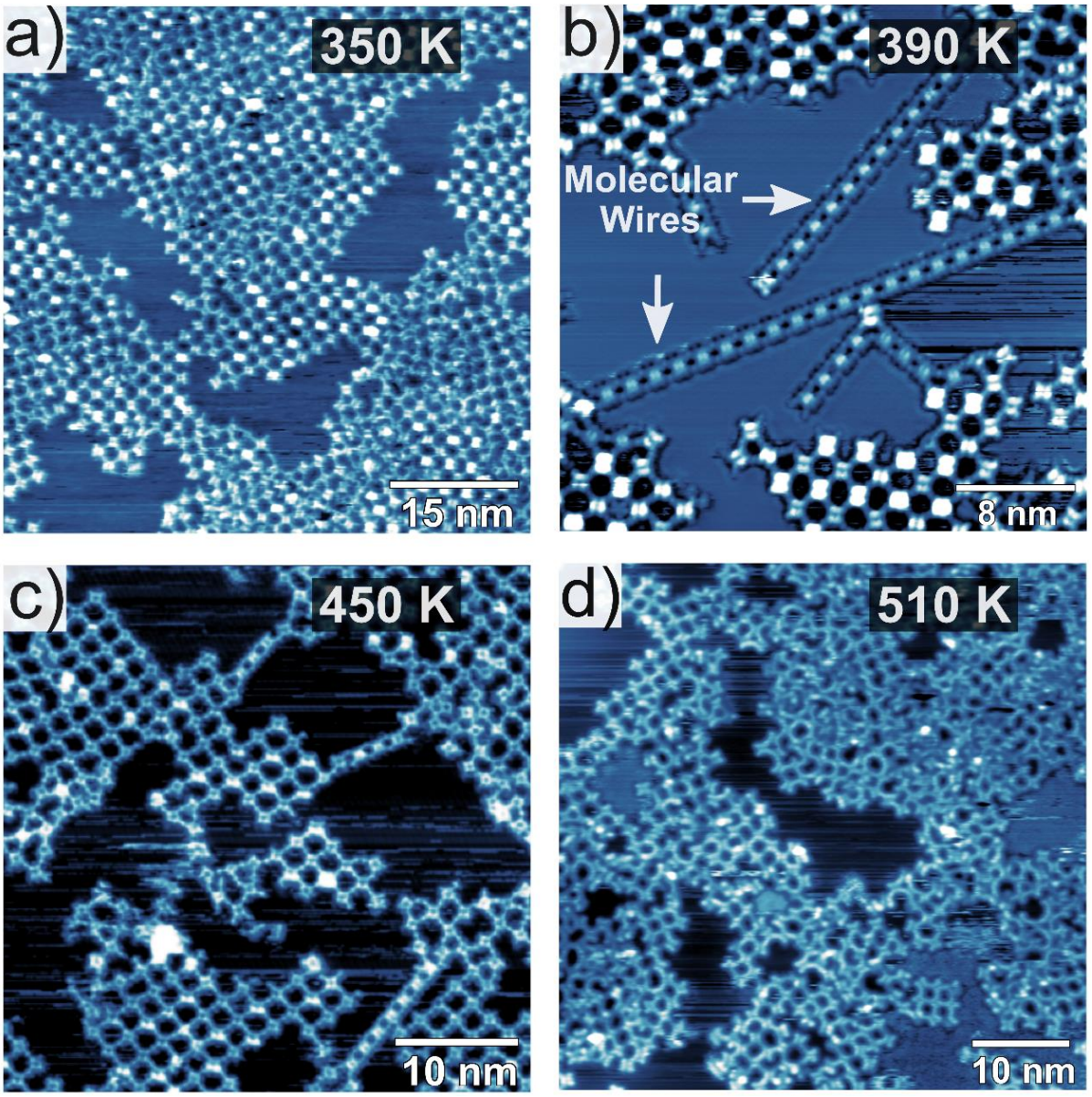

Figure 5.6: Surface-assisted synthesis of H_2TBrPP on preheated Ag(100) substrate. STM image acquired after molecular precursor deposition keeping the surface at (a) 350 K, (b) 390 K, (c) 450 K and (d) 510 K. (b) Coupling motif distribution as a function of substrate temperature deposition at RT, 350 K, 390 K, 450 K, and 510 K, exhibiting selectivity towards square pore networks at 450 K. Tunneling parameters: (a) $I_t = -0.45\ nA$, $V = -0.90\ V$, (b) $I_t = -0.50\ nA$, $V = -0.80\ V$, (c) $I_t = -0.45\ nA$, $V = -0.70\ V$, (d) $V = -1.20\ V$, $I_t = -0.25\ nA$.

In order to identify a temperature range for the selective network formation, a statistical analysis was carried out. The normalized motif distributions are represented in a histogram in figure 5.7. As one can observe, the probability of forming square pore networks increases notably when the polymerization happens at 450 K, indeed 73 % of the molecules counted for this growth condition are forming the square pore network, while for the other explored substrate temperatures, the probability of molecules forming square pore remains constant around 35 %. For higher surface temperatures, the growth

of well-defined organometallic structures is blocked. Additional STM images for synthesis at 390 K and 450 K are shown in figures 5.8 and 5.9, respectively.

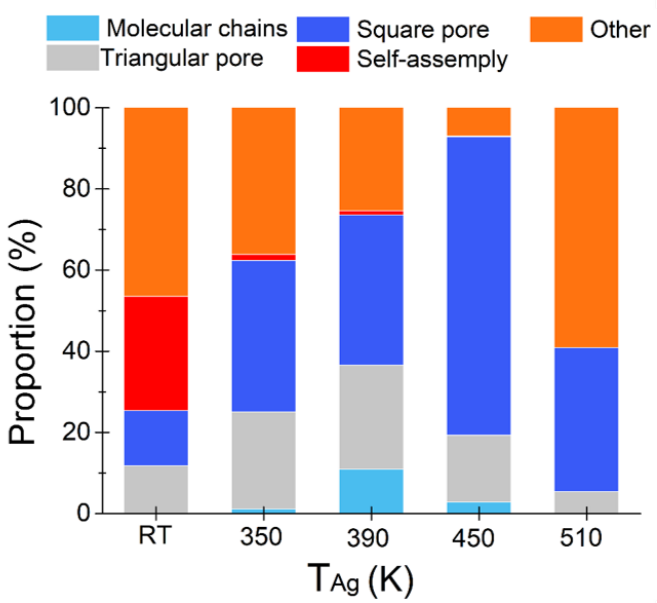

Figure 5.7: Coupling motif distribution as a function of substrate temperature deposition at RT, 350 K, 390 K, 450 K, and 510 K, exhibiting selectivity towards square pore networks at 450 K.

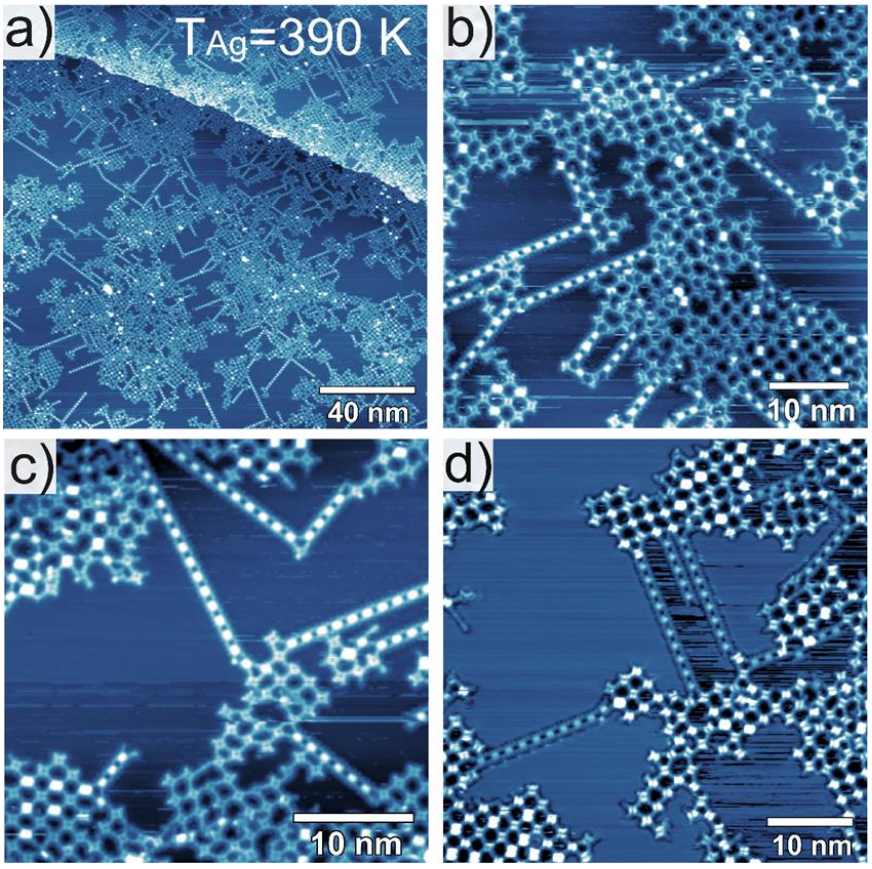

Figure 5.8: Supplementary STM images for the synthesis at 390 K. Tunneling parameters: (a) $V = -1.20\ V$, $I_t = -1.95\ nA$, (b) $V = -0.80\ V$, $I_t = -0.35\ nA$, (c) $V = -1.25\ V$, $I_t = -0.21\ nA$, (d) $V = -1.06\ V$, $I_t = -0.14\ nA$.

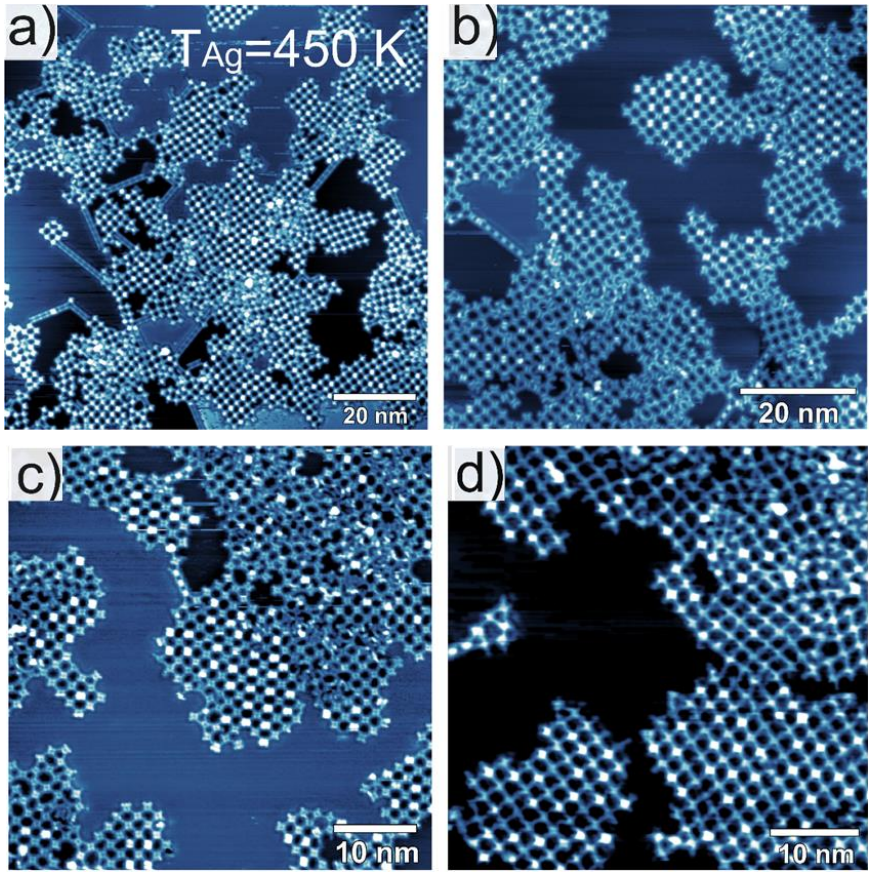

Figure 5.9: Supplementary STM images for the synthesis at 450 K. Tunneling parameters: (a) $V = -1.20\ V$, $I_t = -0.40\ nA$, (b) $V = -0.90\ V$, $I_t = -0.25\ nA$, (c) $V = 1.00\ V$, $I_t = 0.30\ nA$, and (d) $V = -1.1\ V$, $I_t = -0.45\ nA$.

5.2.1 Square pore network

Analysis about regular square porous networks (see figure 5.10a) obtained by holding the substrate at 450 K during deposition was carried out. By careful inspection of tens of these networks on different substrate areas, we determine the unit cell parameters as $c_1 = (1.92 \pm 0.03)\,nm$ and $c_2 = (1.90 \pm 0.03)\,nm$ with an internal angle of $(90 \pm 1)°$ (see figure 5.10b), noting that the array is aligned along <100> directions of the Ag surface. Fast Fourier transformation (FFT) pattern, shown in figure 5.10c, confirms the lattice parameters and supports the long-range order observed for this network. Moreover, in figure 5.10b, it is possible to see small bright protrusions identifying them as Ag adatoms linking porphyrins, which confirms the organometallic character of the network. Langelaar *et al.*[166] reported that Ag adatoms on an Ag(100) surface become mobile from 160 K. Thus, substrate temperatures above 300 K provide a sufficient amount of silver adatoms during the polymerization process.

Such as one can observe in figure 5.10d), the molecular appearance of debrominated porphyrins shows two bright protrusions with a central depression at negative bias voltages and four-fold symmetry contrast at positive bias voltages. We recognize that all molecules are slightly rotated relative to the surface plane and adopt the same intramolecular conformation, identifying it as a saddle shape adsorption geometry. This conformation is characterized by the moderate macrocycle deformation, in which the two opposite pyrrole rings with iminic nitrogens (=N-) are slight rotated to the surface plane, while the other two pyrrole rings with aminic (-NH-) are bent away from the surface plane [167–169]. Jarvis *et al.* [170] study the adsorption deformation of intact H_2TBrPP molecule on Cu(111) deposited at 77 K, finding that molecules in saddle shape conformation are physisorbed, which suggests only van der Waals interactions between the molecule and the substrate surface. The saddle shape deformation has been widely reported for several metal surface-adsorbed porphyrins [87, 157, 171] including 2H-tetraphenyl porphyrin (2H-TPP) on Ag(100) recently proposed by Baklanov *et al.* [172]. From several line profiles acquired, as it is shown in figure 5.10e), the average separation between the pyrrole groups was determined as $(0.57 \pm 0.03)nm$, this value matches the distance of two underlying Ag surface atoms along the <110> direction.

In order to complement our experimental results, the atomic structure of the adsorbed molecule on Ag(100) and the conformation of the square network have been studied by DFT. These calculations were performed, in collaboration, by Duncan John Mowbray, professor at Yachay Tech University in Urcuquí, Imbabura, Ecuador.

Results shown in figure 5.11 predict significantly more stable model molecules in saddle shape conformation orientated along the <100> direction on the Ag(100) surface sitting in hollow adsorption sites. Moreover, the molecules form a stable square pore network with square unit cells of 2.02 nm in length, which closely agrees with our experimental results.

In order to check the organometallic nature of the square pore network, additional DFT calculations for the energy barrier and energy gain for the formation of a C-C network starting from the C-Ag-C network of TPP were done. For this propose a model of two periodic rows of TPP with the edges hydrogenated was used, which allows to see the energy gain upon formation of the C-C bond. To find the transition state, i.e., the C-C bond length with the highest energy, a single Ag(100) layer model was used, and

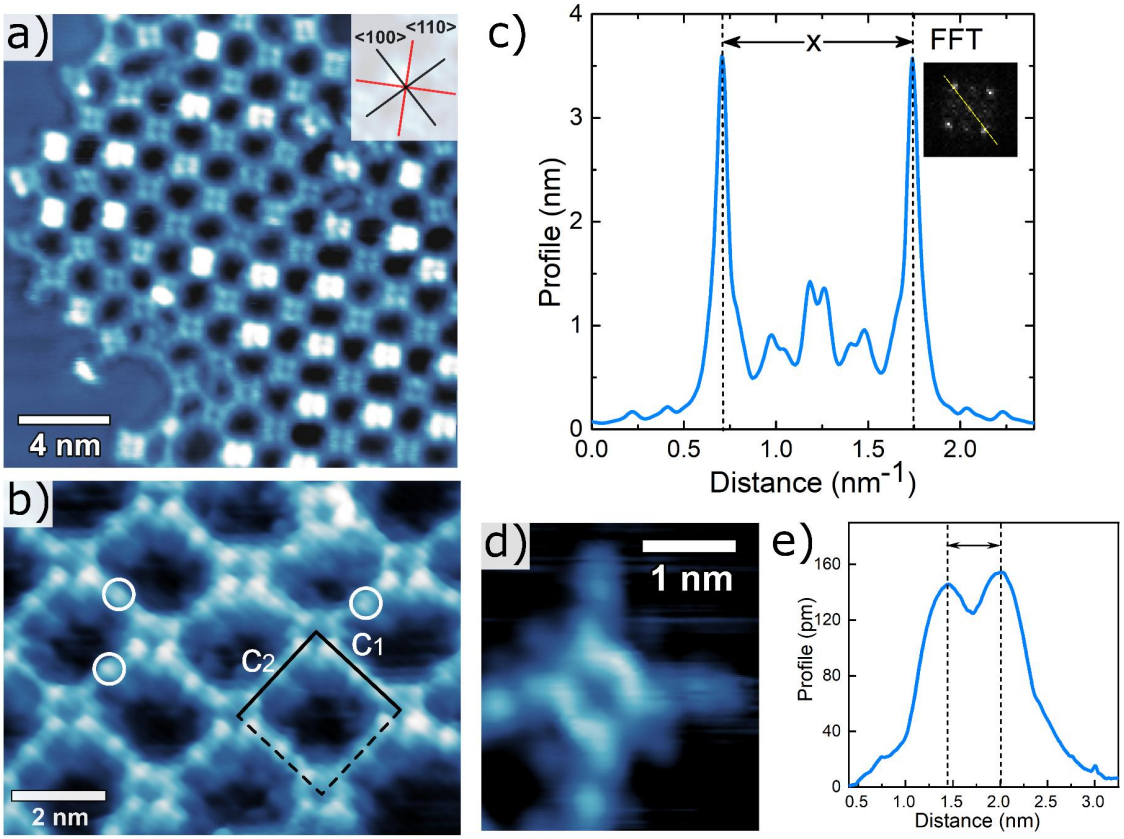

Figure 5.10: Square pore organometallic network. (a) STM image of long-range network. (b) A High-resolution STM 3D image in the perspective of the square pores highlighted the unit cell in black and the Ag adatoms in white circles. (c) FFT square pore network pattern. The distance between the top bright spots was found as $x = 1.04\ nm^{-1}$. In this way, the nanomesh periodicity was determined as $c = (x/2)^{-1}$, this is $c = 1.93\ nm$. (d) High-resolution STM image of the molecule exhibits saddle shape conformation. (e) Tens of scan profiles across the molecule were used to calculate the average distance between the pyrrole groups and its error, $(0.57 \pm 0.03)nm$, this value matches the distance between two underlying Ag surface atoms along the $< 110 >$ direction, which indicated the molecular alignment. Tunneling parameters: (a) $V = 1.20\ V$, $I_t = 0.12\ nA$, (b) $V = -0.78\ V$, $I_t = -5.28\ nA$.

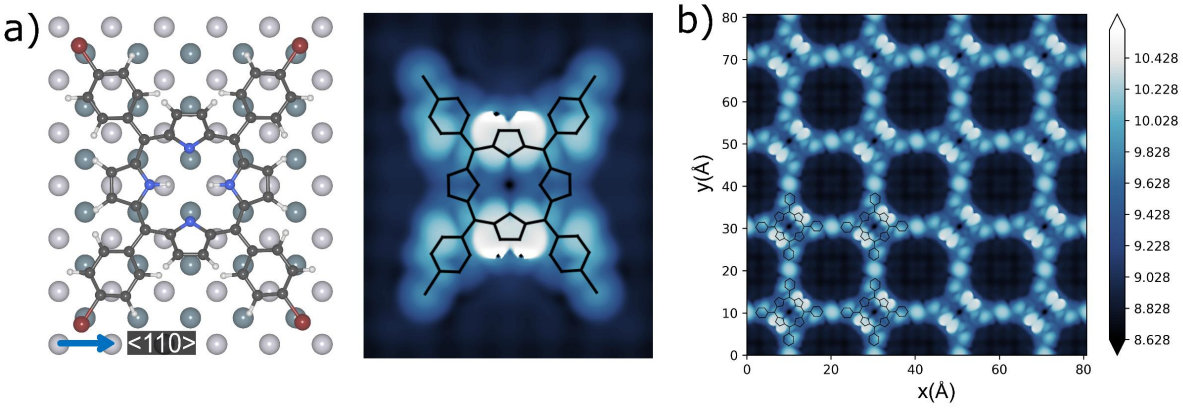

Figure 5.11: (a) Top view of optimized DFT-calculated H_2TBrPP adsorption in a saddle-shape configuration on Ag(100), together with the DFT simulated STM image. (b) DFT simulated image of the Ag-coordinated (C–Ag–C) square pore network. Credit: Duncan John Mowbray.

it is assumed a similar bond length would give the transition state with a three layer Ag(100) slab. The results are summarized in figure 5.12. The results shown that the

three layer slab model should be sufficient to describe what happens experimentally on the Ag(100) surface, suggesting that once the TPP network with Ag adatoms is formed, removing these atoms is a highly energetic process, hence the system becomes kinetically trapped. This would be related to the rapid distribution of any heat/kinetic energy when the network is formed into the silver substrate. However, if the number of silver layers is reduced e.g., using an Ag(100) monolayer on top of an insulating surface such as silicon substrate, the barrier for removing the Ag adatoms is greatly reduced (0.4 eV vs. 1.4 eV), so that the formation of the organic overlayer becomes reasonable at sufficient temperature. From the STM simulated images it is possible to see that where the C-C bond is formed in the network, the benzenes are significantly tilted and show up with quite bright regions, whereas for the C-Ag-C structure the benzene groups are relatively dark. These results clearly suggest both energetically and via STM simulation that the network contains organometallic bonds (C-Ag-C). For the growth of a potentially pure organic network, it is suggests carrying out the on surface synthesis on a single layer of Ag(100) on top of an insulating substrate.

5.2.2 Molecular chains

An STM image of the surface after deposition at 390 K is presented in figure 5.13a, which corresponds to the more favorable growth conditions for the formation of the debrominated porphyrin chains. Notably, the chains do not align with the substrate's main crystallographic directions. We analyzed hundreds of chains to determine the chain orientations and histogrammed the results in figure 5.13b. We found that these structures tend to grow the majority at 30° and 60° from <110> and <100> directions. This result contrasts with what was reported for cyano-functionalized porphyrins chains on Cu(111), where all molecules are aligned along one of the three <110> azimuths, that is, the densely-packed Cu rows of the Cu(111) surface [87].

In figures 5.6 and 5.13a the difference in adsorbate-substrate interactions between molecules in the pore networks and the chains is clear since molecules in both structures reveal completely different adsorption conformations. As shown in figure 5.13a, molecules forming pore motifs adopt saddle shape conformation on Ag(100). In the case of the chains, molecules exhibit an elongated rectangular shape characterized by two bright central protrusions. These features coincide with the strongly distorted model, so-called

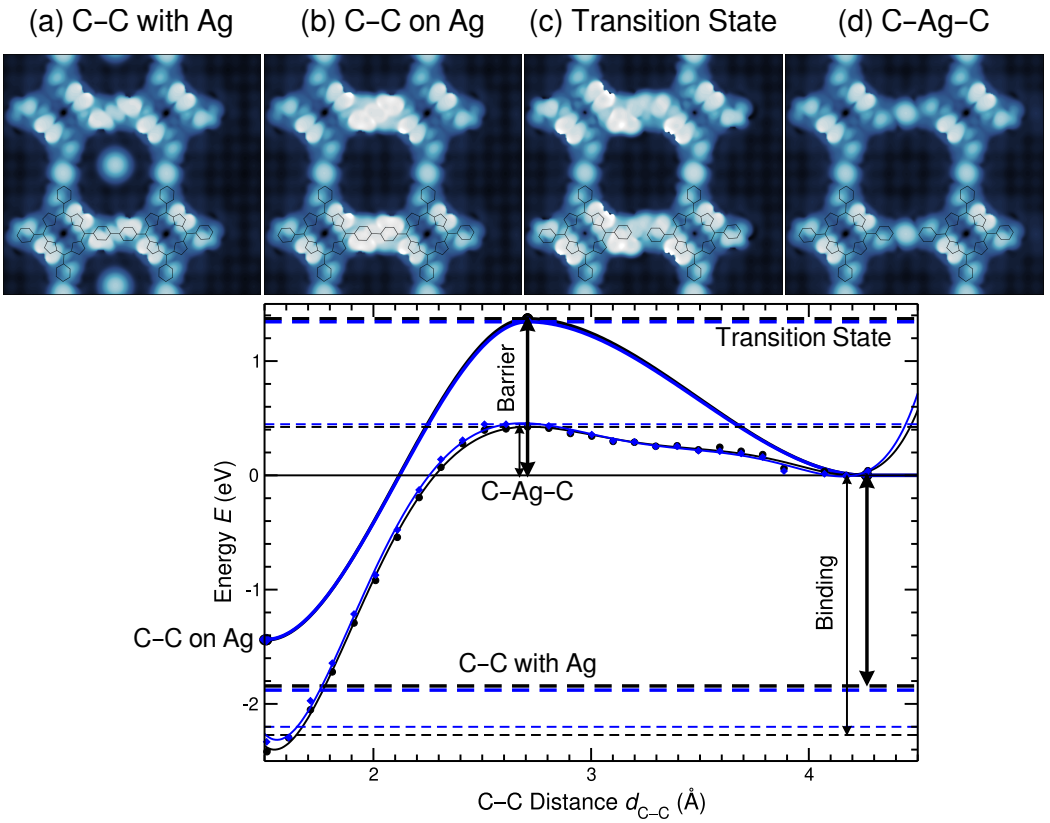

Figure 5.12: STM simulation of TPP network on Ag(100) with (a) C-C organic bond with coadsorbed Ag adatom, (b) C-C organic bond above Ag adatom, (c) transition state between C-C organic and C-Ag-C organometallic bonds, (d) C-Ag-C organometallic bond. e) Energies E in eV relative to the organometallic network versus C-C separation d_{C-C} (in $\mathring{A}$) on a three-layer (thick lines) and single-layer (thin lines) Ag(100) neutral (black) or charged by -1e (blue) surface.

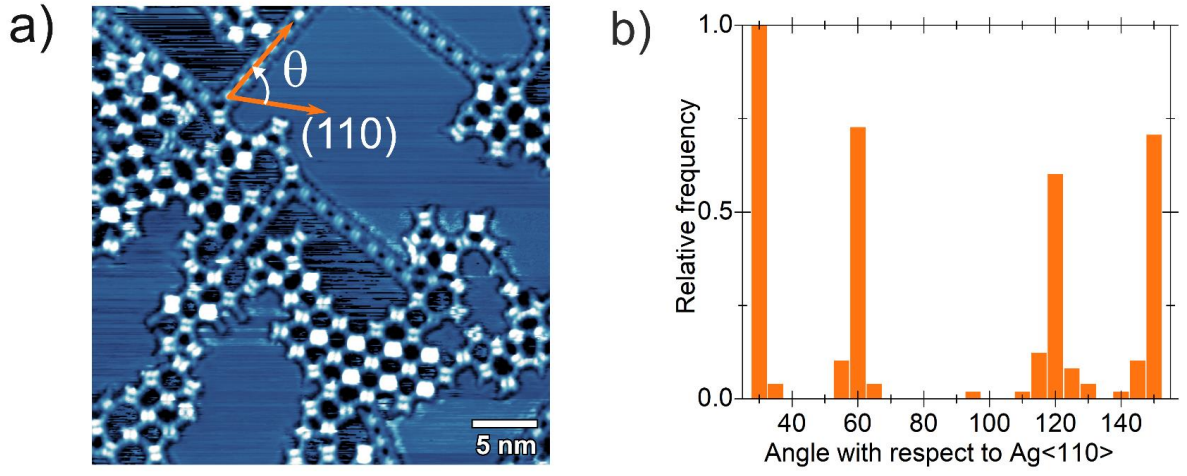

Figure 5.13: Single-step synthesis of molecular chains. (a) Overview of the sample prepared at 390 K. The image is denoted as θ the angle forming between the ¡110¿ direction and the chains. (b) The orientation of 177 chains with respect to $< 110 >$ crystallographic direction was determined and represented in a histogram. The bar width is 5°. Tunneling parameters: (a) $V = 0.80\ V$, $I_t = 0.26\ nA$.

inverted conformation, which has been proposed for several porphyrins on Cu(111) [87, 151–153, 155, 173], where two iminic pyrrole groups are rotated quasi-perpendicular to the surface, and the iminic N atoms are pointing toward the surface, specifically over bridge sites between two adjacent Cu atoms of the surface.

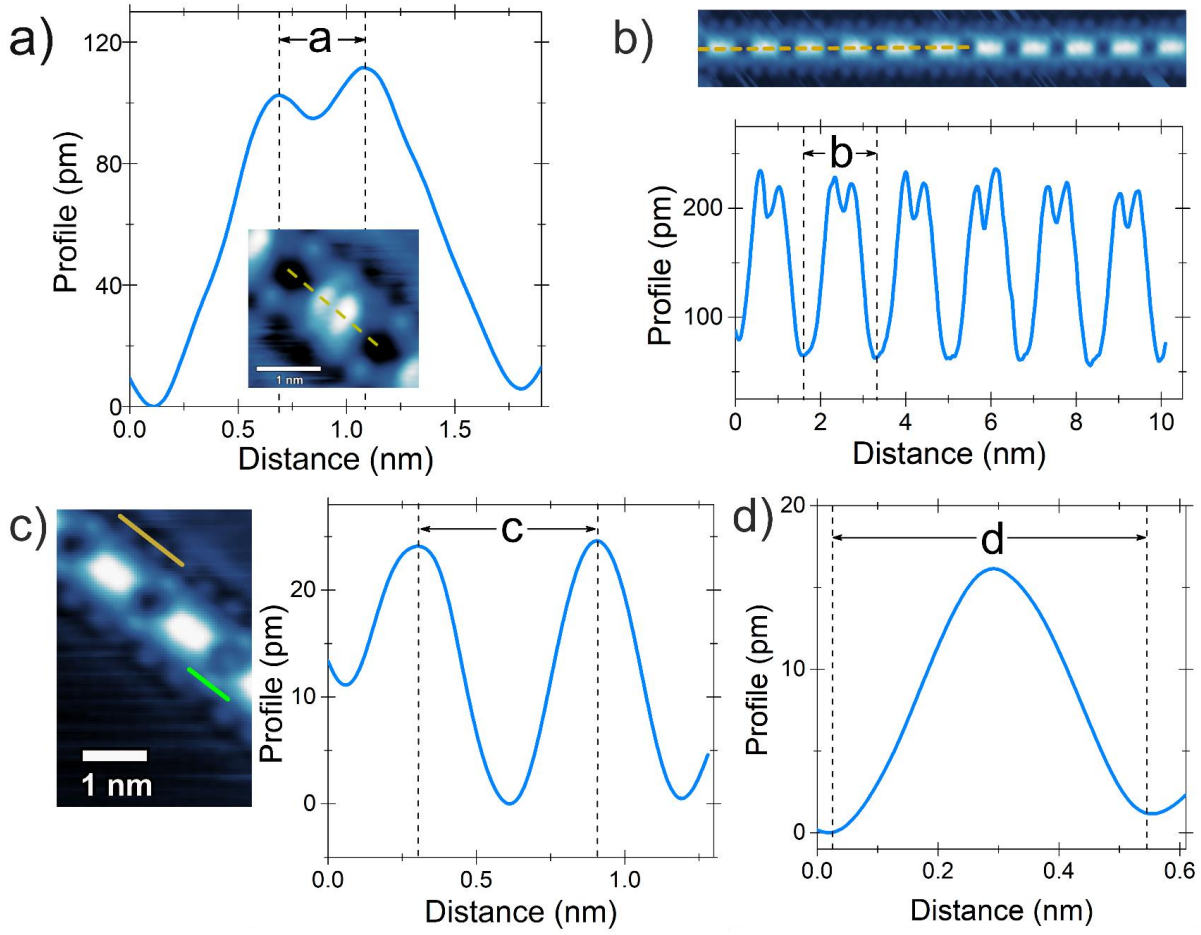

Figure 5.14: (a) The average distance between the two iminic pyrrole groups ($a = 0.39 \pm 0.02\,nm$) was determined from several line profiles corresponding to the yellow line in the inset STM image. (b) Periodicity of the molecules into the chains ($b = 1.67 \pm 0.02\,nm$). (c) From profiles taken as the orange line in the STM image, the distance between extra-legs was determined as $c = 0.63 \pm 0.02\,nm$. Similarly, (d) the Ag-ad size was estimated as $d = 0.54 \pm 0.04\,nm$.

In order to shed light on the iminic N atoms adsorption sites on Ag(100), the average distance between the two bright central ovals in the molecule was determined. Figure 5.14a shows a typical scan profile along the chain propagation direction on the surface. From statistical analysis of several molecules, we found that the average distance between the pyrrole protrusions is $a = 0.39 \pm 0.02\,nm$. Similarly, the periodicity of the chains was determined as $b = 1.67 \pm 0.02\,nm$ (see figure 5.14b). Another interesting aspect of the chains is the two pairs of protrusions that appear on opposite sides of the molecule, as seen in figure 5.14c. Ceccatto dos Santos *et al.* [155] observed similar features on

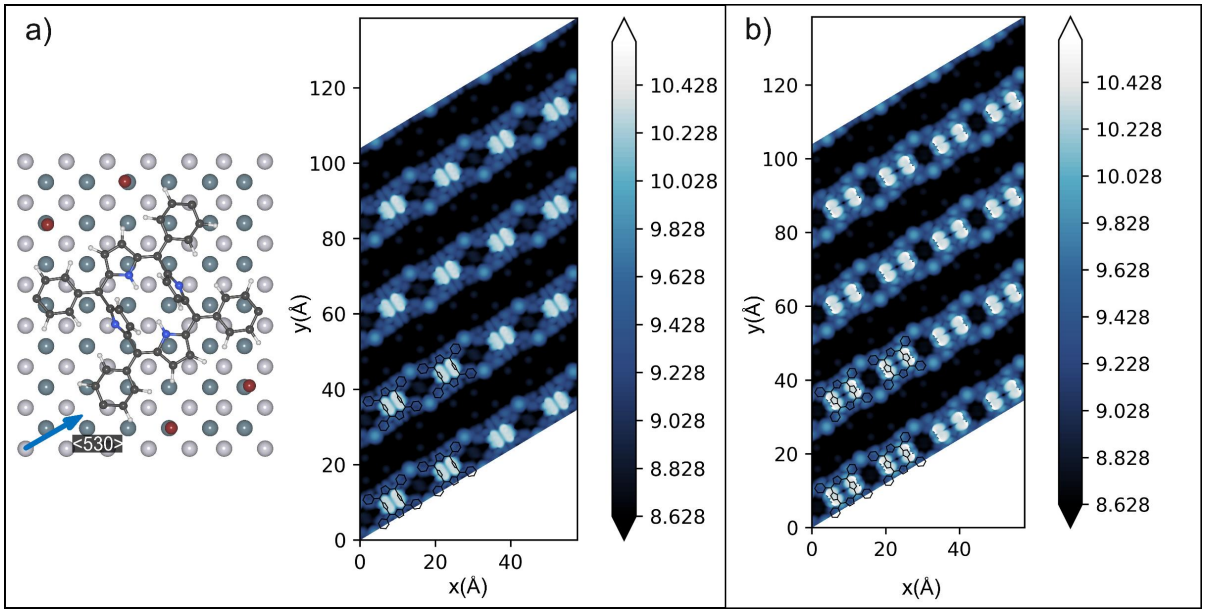

Figure 5.15: DFT calculation of the molecular chains in inverted and saddle conformation.

Cu(111). They identified these additional features, named "extra-legs", as bromine adatoms, finding that the distance between the halogens corresponds to the separation of the nearest neighbor along the $< 1\bar{1}0 >$ direction of Cu(111). In our case, the average distance between these protrusions was determined as $c = 0.63 \pm 0.02\,nm$. In addition, the average size of the Ag-adatom was determined as $d = 0.54 \pm 0.04\,nm$ (see figure 5.14d).

Figure 5.15 shows the STM simulated images of the molecular chains completely relaxed along $\langle 530 \rangle$ direction on Ag(100) in "fully inverted" and saddle shape configurations with four Br adatoms adsorbed nearby the chain on hollow sites (see figure 5.15a and b respectively). It was found that the inverted configuration is 0.117 eV, more stable than the saddle configuration, with the four Br atoms adsorbed nearby in the hollow site. The Br atoms gain 39 meV per atom relative to Br adsorbed on the hollow site without an adjacent 2AgTPP chain. Similarly, without the Br atoms, the inverted chain is 0.142 eV, more stable than the saddle chain. Moreover, in the fully inverted configuration, the top C atoms are now separated by 0.39 nm, whereas the Br atoms are separated by 0.63 nm, which perfectly agrees with our experimental results expressed by a and c from figure 5.14.

5.3 Conclusions

In this work, we investigated the synthesis of a square pore network from Br4TPP porphyrin. For that purpose, we carefully selected as substrate Ag(100), a surface with a square lattice. Due to the substrate reactivity and low debromination barrier, organometallic motifs were already formed at RT. These motifs include triangular, hexagonal, and pentagonal porous and disorder structures. Looking for alternatives to selectively promote the growth of square pores, we studied the critical role of substrate temperature during the deposition of the precursor. For 450 K, 70 % of the molecules on the surface are forming a square pore network, while for the other temperatures explored, the number of molecules in this configuration remains almost constant. In this way, we found the optimal conditions to selectively induce the synthesis of these structures.

From the STM data, we identified additional motifs that were not observed for deposition at RT or after annealing. The synthesis of these molecular chains is favorable at 390 K. The conformation of the molecule inside the chain is recognized as an inverted structure; the typical adsorption conformation reported on Cu(111). On the other hand, molecules in the square lattice and other motifs exhibit the usual saddle shape conformation.

From our best knowledge, this is the first time that porphyrins are observed in an inverted structure and saddle shape on Ag(100). We can understand the coexistence of these two absorption geometries in terms of the adsorption sites and the orientations of the molecules in relation to the main crystallographic directions of Ag(100). Energetically, these two conformation are potential minima separated by a reasonable energy barrier. Molecules can only overcome the barrier when isolated molecules arrives on “hot surface”. In this sense, molecules that undergoes to porous network are trapped in the first potential minima (saddle shape) and can not be promoted to chains (inverted structure) even with annealing. Such a energetic trap is related to the C–Ag–C energy formation barrier (i.e., saddle shape has a deeper minimum). In short, depositing at lower temperatures, molecules are always populating the first and deeper minimum (saddle shape) since it can not overcome the potential barrier to the second and smaller mimimum (inverted).

Chapter 6

Synthesis of N-doped pore chains on Cu(111) and Ag(100)

On-surface synthesis as a bottom-up strategy holds great potential for atomically precise fabrication of carbon nanostructures. Doped graphene nanoribbons (GNRs) with heteroatoms are an ideal strategy to tune their electronic structure. In this frame, we present a systematic study of on-surface synthesis of GNRs from a nitrogen-doped and bromine-terminated molecules, 2,7,11,16-tetrabromotetrabenzo[a,c,h,j]- phenazine (2TBTBP). The critical role of the catalytic metal surface was studied by exploring two different substrates, Cu(111) and Ag(100). According to the geometry of the precursor, we expected covalent porous chains oriented at 30° with respect to the graphene's high-symmetry directions, which leads to an armchair termination. The width of the armchair GNRs is defined by the number of dimer lines across the ribbons, which in this case corresponds to 9 dimmers, as illustrated in figure 6.1.

This chapter describes the synthesis of porous nitrogen-doped GNRs. In order to understand the mechanisms of formation of the different molecular structures, we identify the types of chemical bonds involved and the role of the surface as a promoting agent of polymerization reactions. In addition, we characterize the electronic properties of these

1D porous structures.

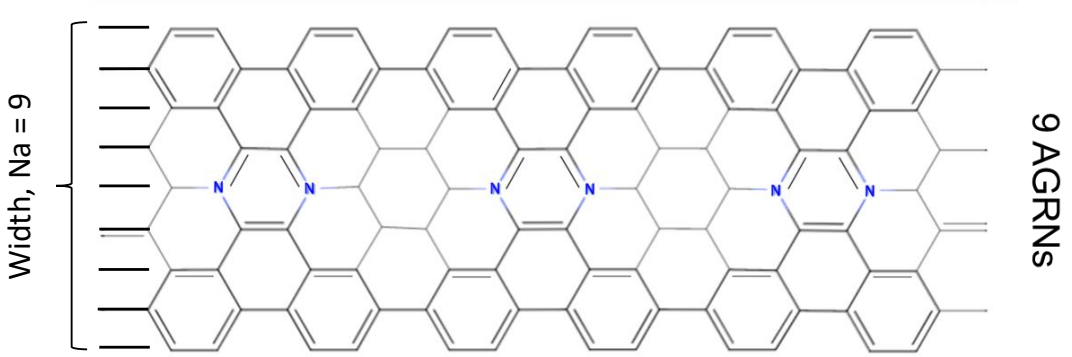

Figure 6.1: Illustration of the 9 armchair graphene nanoribbon porous and doped with N atoms. The light-gray bonds correspond to the no present structure on the GNRs.

6.1 Synthesis of N-doped GNRs on Cu(111) via Ullmann coupling reaction

The molecules were deposited on a clean Cu(111) substrate held at RT for 3 min. STM image in figure 6.2a reveals low surface coverage. The synthesis of new nanostructures on surface demands original building blocks. The dehalogenation process is a decisive stage for the Ullmann coupling reaction, which produces reactive sites that subsequently undergo bonding formation. The strong influence of the Cu(111) on the reaction steps sequence is evident in figure 6.2b, which shows an already formed irregular chain. According to the features on the image, we identify the coordination of the molecules via Cu-adatoms, i.e., C–Cu–C bonds. This suggests the cleavage of the C–Br bond at RT. In addition, whites arrows indicates sites where the metal-organic coordination is missing. Due to the position of Br atoms on 2TBTBP, diverse structures are present on the surface. Besides linear chains, zigzags chains as seen in the figure 6.2c, leaving unbound reactive sites. Figure 6.2d displays a regular chain consisting of 5 monomers. The image makes it possible to clearly distinguish the pore formed between the molecules, the Cu adatoms, and the contrast difference between the nitrogen-doped central benzene and the undoped ones. The contrast difference between C and N atoms in the STM images could be associated with the larger electronegativity of N atoms compared to C atoms. Therefore, N atoms tend closer to the substrate than C atoms [174]. Circular protrusions observed on the edges of the chains are identified as Br atoms (see figure

6.2b,d), similar to previous study on Cu(111), where the bromide (Br–Cu) assembled along with the organometallic structures after the dehalogenation process [155, 175].

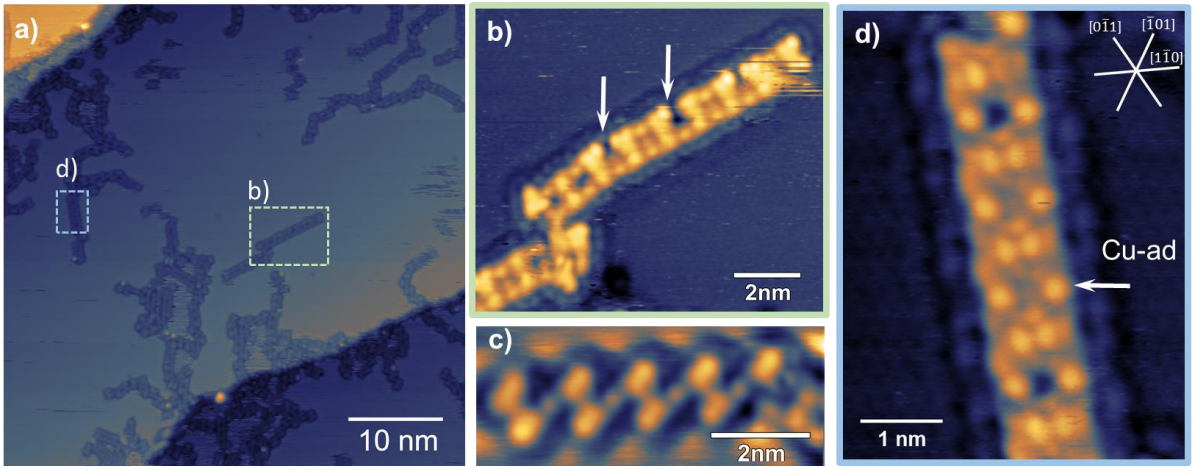

Figure 6.2: STM images in constant current mode acquired after deposition of molecules at RT for 3 min. (a) Overview of the sample. (b) Zoom in on the rectangular region (green) marked in (a). The white arrows indicate the absence of some organometallic bonds in the chain. (c) STM image of a connected zigzag chain. (d) High-resolution images of the region highlighted by the blue rectangle in (a). Tunneling parameters: (a) $V = -1.20\ V$, $I_t = -0.23\ nA$, (b) $V = -0.67\ V$, $I_t = -2.44\ nA$, (c) $V = -1.44\ V$, $I_t = -0.25\ nA$, and (d) $V = -0.26\ V$, $I_t = -0.21\ nA$.

Therefore, neighboring monomers coordinated by Cu ad-atoms form organometallic chains at RT. STM data does not reveal long-range chains, likely because the Br atoms left after the debrominated process are chemisorbed to Cu atoms at the surface in the vicinity of the molecule, hindering the molecular diffusion necessary to reach the long-range order. Teeter *et al.* [176] reported the synthesis of the chevron GNRs on Cu(111) from 10-10'-dibromo-9-9'-bianthracene (DBBA) molecule after annealing at 523 K. Following a similar approach, we performed subsequent heat treatments on our sample. Instead of promoting covalent bonds, molecules desorbed from the surface.

To promote the diffusion of the precursor and Cu ad-atoms, which could induce the formation of more extended one-dimensional organometallic structures, the role of the substrate temperature during the sublimation of the molecules was studied. Therefore, 2TBTBP molecules were deposited on Cu(111) held at 400 K, 450 K, and 500 K. For all experiments at temperature above RT, the sublimation rate and deposition time are comparable. Most representative STM images for deposition at RT and 400 K are shown in figure 6.3. For both conditions irregular organometallic structures are observed on Cu(111).

Figure 6.4 displays results obtained after precursor deposition keeping the substrate at

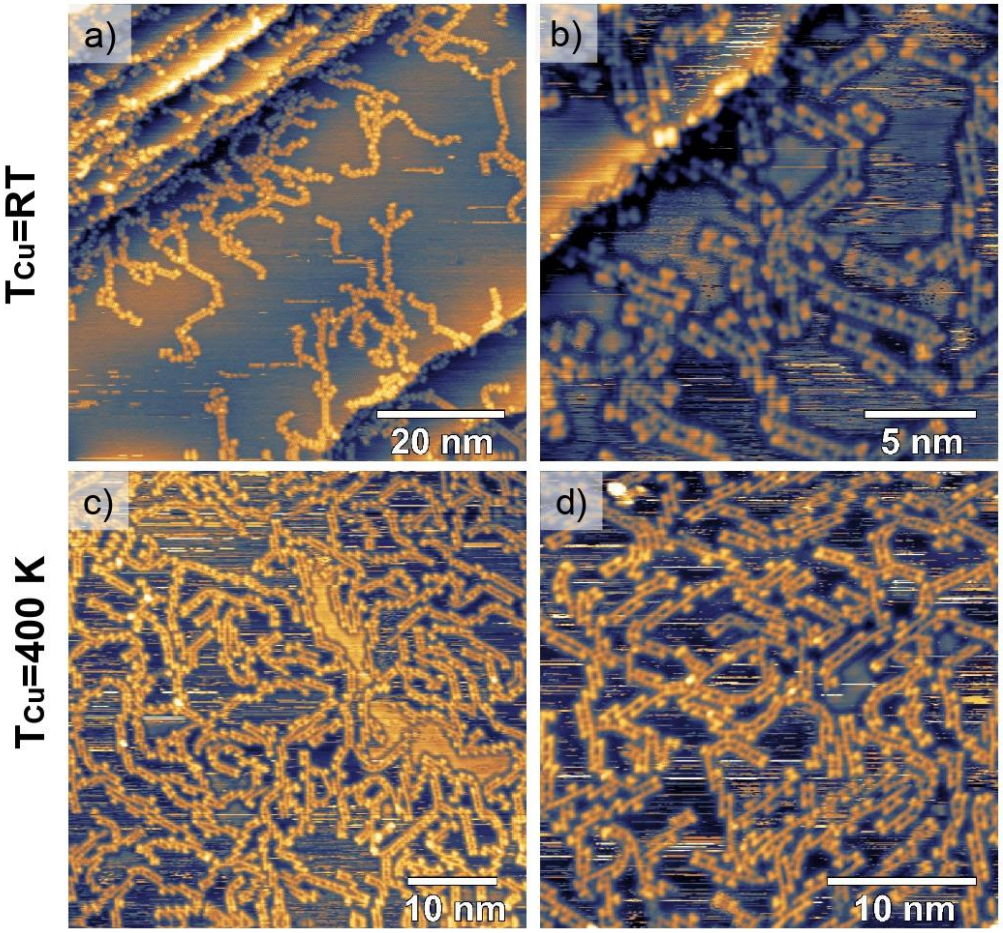

Figure 6.3: STM images in constant current mode acquired after deposition of molecules (temperature into the crucible 550 K) on Cu(111) substrate maintained at (a)-(b) RT during 9 min and (c)-(d) 400 K during 30 min. Tunneling parameters: (a) $V = 1.31\ V$, $I_t = 0.24\ nA$, (b) $V = -1.40\ V$, $I_t = -0.25\ nA$, (c) $V = -1.31\ V$, $I_t = -0.24\ nA$, and (d) $V = -1.31\ V$, $I_t = -0.24\ nA$.

450 K. Molecules formed one-dimensional (1D) structures. One can see short chains with bright ends. The intramolecular spacing between bright molecules $a = (8.5 \pm 0.3)\ \mathring{A}$ is slightly shorter compared to the intramolecular distance for the metalled chains $b = (10.9 \pm 0.3)\ \mathring{A}$ (see figure 6.4b-c)). This suggests that bright molecules are covalently bonding. From high-resolution STM images, in figure 6.4b-c, it is clearly distinguishes different features related to unmetalled and metalled chains. For the first one, the pore formed between molecules shows an ellipsoidal geometry together with the flattening of the molecule. The bright protrusions associated to Cu adatom are observed for the other one. After carefully inspecting the sample, C–C bonds constituted for more than two molecules were rarely observed. In figure 6.4b, the end of one chain is pointed out by a black arrow. We identified the bright feature as one molecule, which exhibits a planar adsorption structure similar to what is seen for C–C dimers. This is peculiar because next to the molecule Cu adatoms are observed.

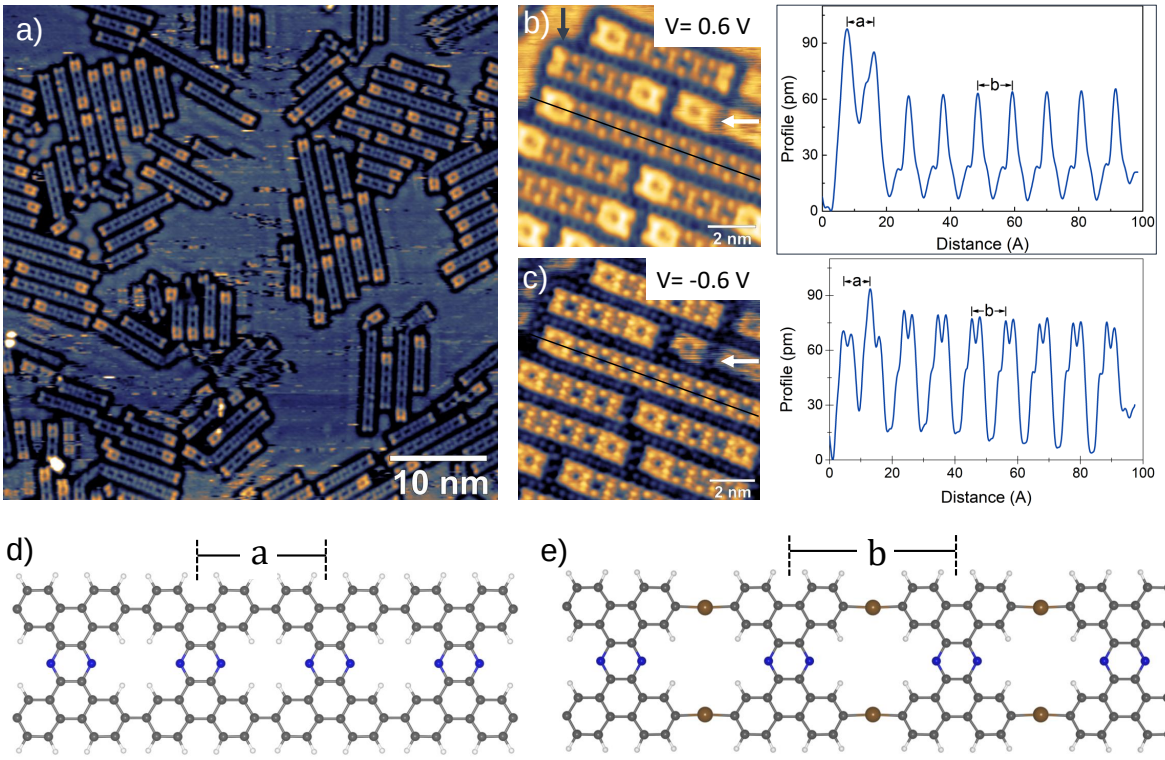

Figure 6.4: (a) STM overview image in constant current mode acquired after deposition of molecules on Cu(111) substrate hold at 450 K during 30 min and post annealing at the same temperate for 1 h. STM images of the same region acquired with different sample bias polarity (b) 0.6 V and (c) -0.6 V. Next to the images, profiles took along the chain are plotted. Illustration of (d) the C–C chains, and (e) metallated chains. The intramolecular spacing is indicated as a and b. Tunneling parameters: (a) $V = -1.20\ V$, $I_t = -0.32\ nA$, (b) $V = 0.6\ V$, $I_t = 0.42\ nA$, and (c) $V = -0.6\ V$, $I_t = -0.42\ nA$

Next to the longer chains, streaky patterns were observed in STM data. For instance, in figure 6.4c-d is pointed out by white arrows. This pattern is identified as mobile molecules forming a covalent dimer. Additional data in figure 6.5 shows the same area imaged three consecutive times using identical tunneling parameters. Despite the typical thermal drift, it is clear that organometallic and mixed chains are stably adsorbed. Likely, the molecules are anchored to the surface due to the coordination with the Cu adatoms. On the other hand, the diffusion of the covalent chains is noticed, such as in the white rectangle in the figure 6.5, where chains are adsorbed for a specific time but tend to hop to nearby adsorption sites. In particular, figure 6.5b shows two dimers spatially separate. The following image (figure 6.5c) acquired after 45.3 s displays a new covalent ribbon constituted by four units (three pours). These results suggest that C–C coupling is achieved between these two dimers. According to our observations, this diffusion is independent of the size of the chain. The high mobility of the covalent chains prevents accurate determination of coverage. In addition, diffusive noise around the structures is observed in the figure 6.5, Bohringer *et al.* [177] correlate this noise with mobile

molecules crossing multiple times below the scanning tip.

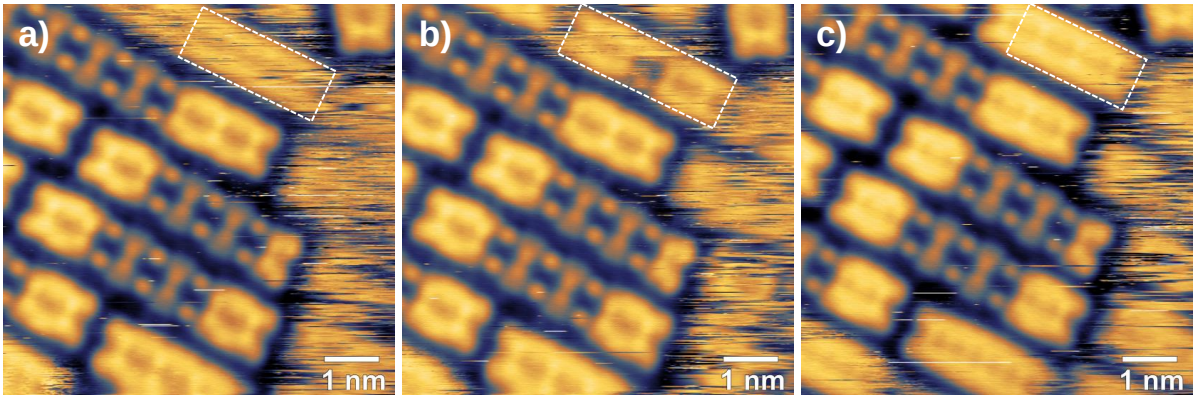

Figure 6.5: STM images taken in sequence for the deposition hold the Cu(111) at 450 K for 30 min, and after 24 h of the synthesis. The coordinates of the center of the image, bias voltage and tunneling current are the identical for each image. The acquisition time for each image was 45.26 s. White rectangle remarks a mobile covalent chain. Tunneling parameters: $V = 1.16\ V$, $I_t = 0.23\ nA$.

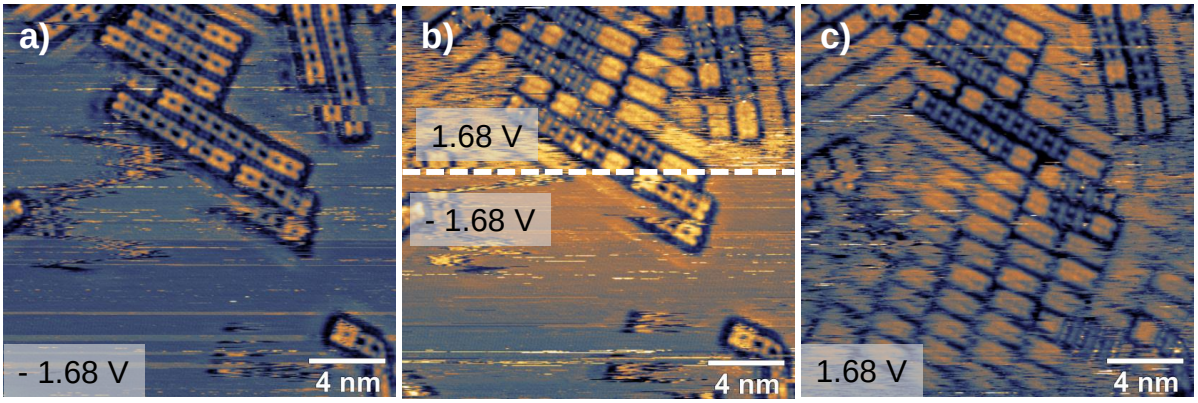

Figure 6.6: STM images taken in sequence for the deposition hold the Cu(111) at 450 K for 30 min, and after 24 h of the synthesis. The acquisition time for each image was 78.82 s. Switching from negative (a) to positive bias (c). (b) The STM image shows the transition between the polarity after a single scan line indicated by a white dash line. Tunneling parameters: $I_t = 2.47\ nA$.

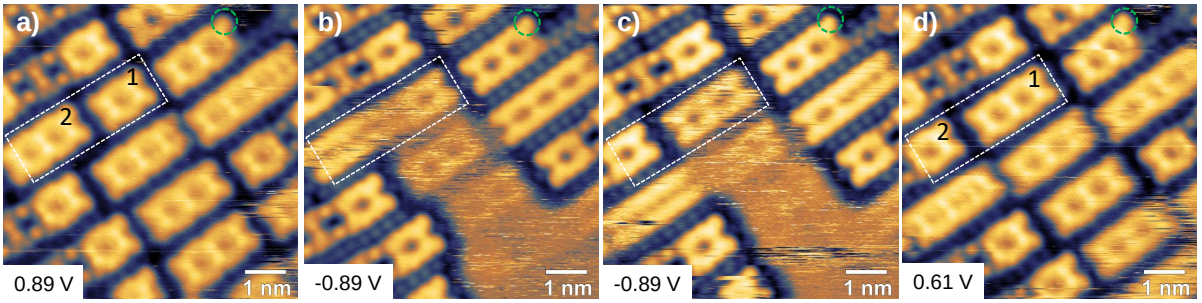

Figure 6.7: STM images taken in sequence for the deposition hold the Cu(111) at 450 K for 30 min, and after 24 h of the synthesis. The acquisition time for each image was 37.99 s. The green circle shows a particular feature of the stably adsorbed covalent dimer. Tunneling parameters: (a) $V = 0.89\ V$, $I_t = 0.34\ nA$, (b)-(c) $V = -0.89\ V$, $I_t = -0.34\ nA$, and (c) $V = 0.61\ V$, $I_t = 0.34\ nA$.

The dependence of the covalent phase mobile on the bias voltage polarity is shown in

figure 6.6. The images taken in the same scanned area under different sample bias voltage polarities demonstrate that covalent chains are better observed with positive bias compared to negative bias voltage. Switching from negative to positive (see figure 6.6b), short covalent chains are imaged on the surface. However, C–C dimers at the end of organometallic chains are imaged independently of the tunneling parameters.

Figure 6.7 reveals the "spontaneous" cleavage and new covalent bond formation on Cu(111). The white rectangle in figure 6.7 highlights a dimer (label as 1) next to a trimer (label as 2). Another dimer in the same direction is stable on the surface, and a green circle spotlights a particular feature, verifying this stability. The following two images (b-c) acquired at negative bias do not clearly show these covalent structures. In the fourth image (d), taken at positive bias, the covalent chains are observed again, emphasizing the inversion of the chains. This event leads us to propose the spontaneous breaking and covalent formation after deposition at 450 K and measuring at RT. The precise physical mechanism involved (tip-induced reaction, tip-inducing catalytic reactions mediated by Cu-adatoms, etc.) needs further experimental and theoretical investigation.

The local density of states (LDOS) was explored by STS measurements, which the differential tunneling conductance dI/dV is recorded at constant STM tip height. Figure 6.8 shows the dI/dV spectrum measured close to the position of the heteroatom dopant on the organometallic chain; such is indicated by the green dot in the inset STM image and compared to the acquired on the clean metal substrate. In agreement with previous studies [178, 179], the Cu(111) surface states are manifested as a step-like feature shifted to negative energies in the dI/dV spectrum, this correspond to the low band edge, or E_0 of the surface state electrons [180]. The typical values reported for E_0 is around 0.4 V, which is consisted with our result. The dI/dV spectrum acquired at the position marked by the green dot in the STM image revels two peaks at -1.41 V and -1.80 V. In addition, on the positive sample bias side, we estimated the onset at $\sim$1.0 V. These results allow us to estimate a band gap about 2.4 V, which demonstrates the semiconductor character of the organometallic chains.

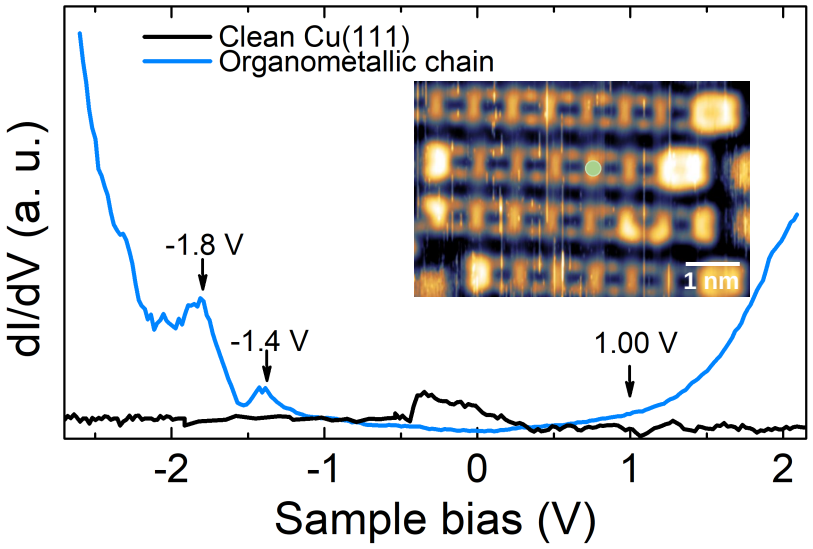

Figure 6.8: dI/dV spectra taken on clean Cu(11) (black curve) and the N atom position on the organometallic chain (blue curve), this position is marked by a green circle, as shown in the inset STM image. Tunneling parameters: $V = 1.12\ V$, $I_t = 0.30\ nA$.

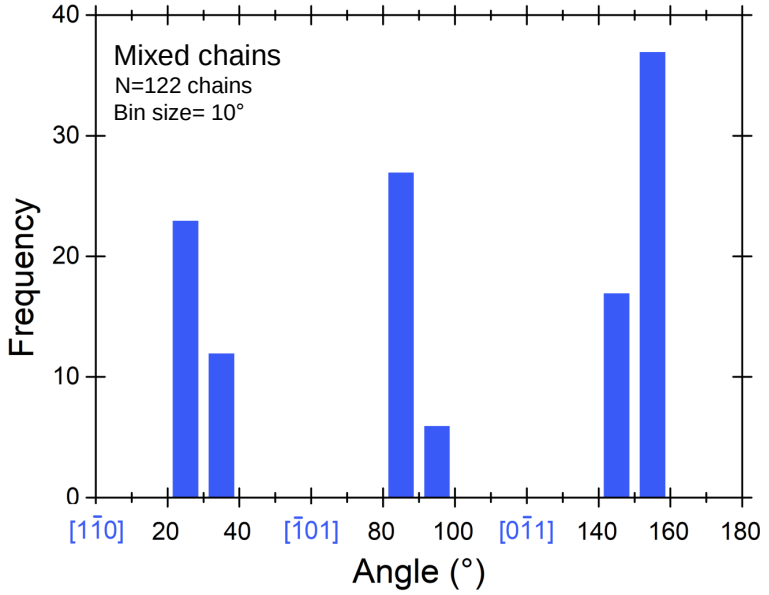

Figure 6.9: Orientation of the organometallic chains with C–C ends. From atomic resolution images of the substrate the main crystallographic directions of the crystal were determined. Considering these directions, the orientation of the mixed chains was found out and plot in the present histogram.

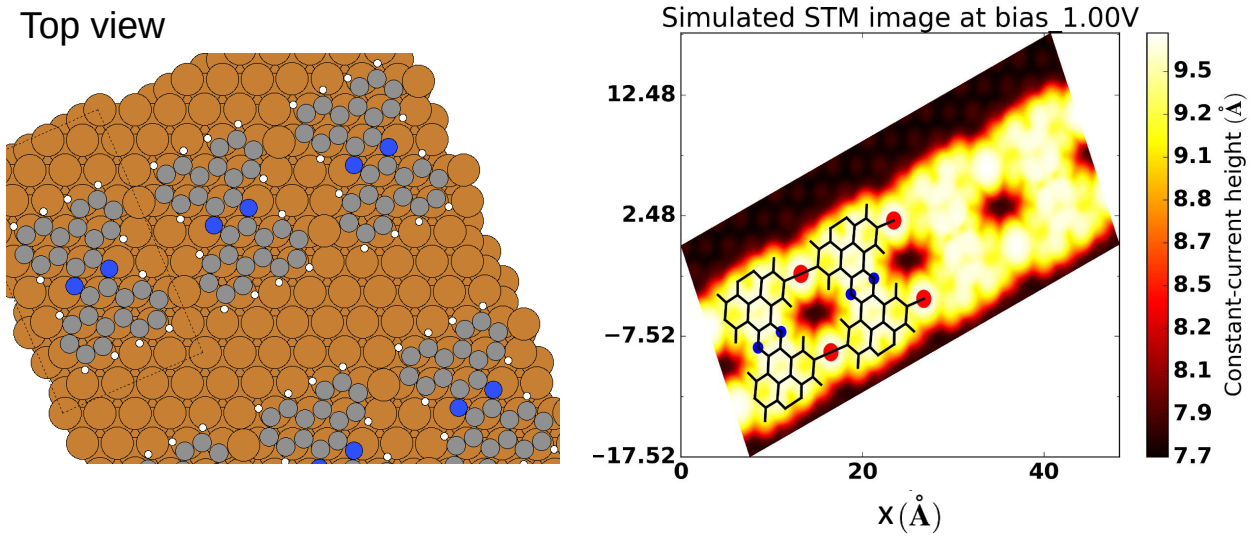

Figure 6.10: Top view of the organometallic chains and its STM simulation image based on DFT calculations, the last one is in agreement with our data. The bias voltages used is $V = 1.00\ V$. The theoretical calculations did not take into account Br adatoms adjacent to the molecule.

According to the intramolecular separation for organometallic chains, the precursor is not commensurate with Cu(111). Therefore, chains are expected to be aligned at an angle relative to the principal axis of the substrate. Consequently, the orientation of the organometallic chains with C–C ends was investigated. For that purpose, from Cu(111) atomic resolution images, the main crystallographic directions of the substrate were identified. After analyzing 122 chains, we found that molecules are aligned, forming $(25 \pm 2)°$ relative to Cu(111) main directions, such as is shown in figure 6.9.

In order to support the experimental findings for the organometallic chains, STM simulations were performed. Figure 6.10 shows the top view of the relaxed metallated chain on Cu(111), next to the simulated STM image at 1.00 V bias voltage. The periodic distance Cu-Cu along the chain is $b_T = 11.14\ \mathring{A}$, falls well within our error bar ($b = (10.9 \pm 0.3)\ \mathring{A}$). The angle relative to the principal axis is about $\sim 23°$, also in perfect agreement with our experimental value.

At 500 K, the quantity of 2TBTBP on the surface of Cu(111) decreased considerably compared to the previous experiments performed on similar molecular flux, this findings could indicate precursor desorption at this temperature. The molecular diffusion across steps edges is reduced, in particular full covalent chains are formed in this places. This fact suggest the physisorption of the GNRs on Cu(111). Nevertheless, covalent structures coexist at the surface with the organometallic intermediates chains. The edge of the

covalent chain synthesized at this temperature corresponds to the well known armchair graphene nanoribbon (9-AGNR) [181]. Inside the pore four C dangling bonds terminated by H atoms are presented, together two N atoms, such as is illustrated in figure 6.11.

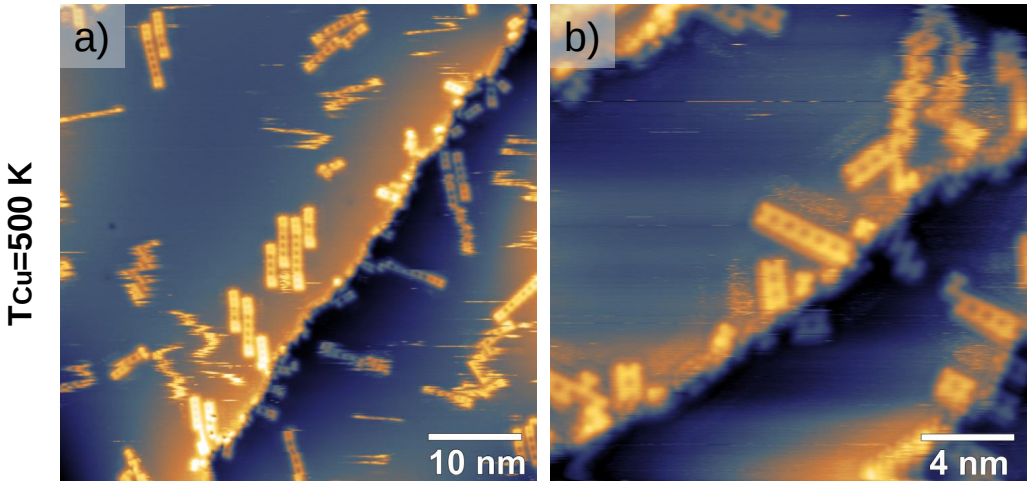

Figure 6.11: STM images in constant current mode acquired after deposition of molecules on Cu(111) substrate maintained at 500 K. Tunneling parameters: $V = 1.12\ V$, $I_t = 0.30\ nA$.

6.2 Synthesis of N-doped GNRs on Ag(100) via Ullmann coupling reaction

A previous study carried out by Pawlak *et al.* [182] shows the successful synthesis of N-doped GNRs from 2TBTBP on Ag(111) by Ullmann coupling reaction. They observed the formation of porous N-GNRs and metastable organometallic one-dimensional complexes. In their work, it is reported a band gap of about 2.2 V, which demonstrate the semiconductor character of the covalent chains. Here, we choose Ag(100) as a metal surface.

Based on previous results obtained using brominated precursors on Cu(111) and Ag(100) substrates during my Ph.D., we avoided investigating the behavior of the precursor deposited at RT on the Ag(100) substrate. Nonetheless, the role of substrate temperature has been carefully studied. Specifically, three growths were made, keeping the substrate at 450 K, 500 K, and 550 K.

Figure 6.12 depicts a representative STM image of the sample synthesized at 450 K. The precursor's debromination and the growth of long organometallic chains are stimulated at this temperature, as shown in figure 6.12b. Based on atomic resolution images of

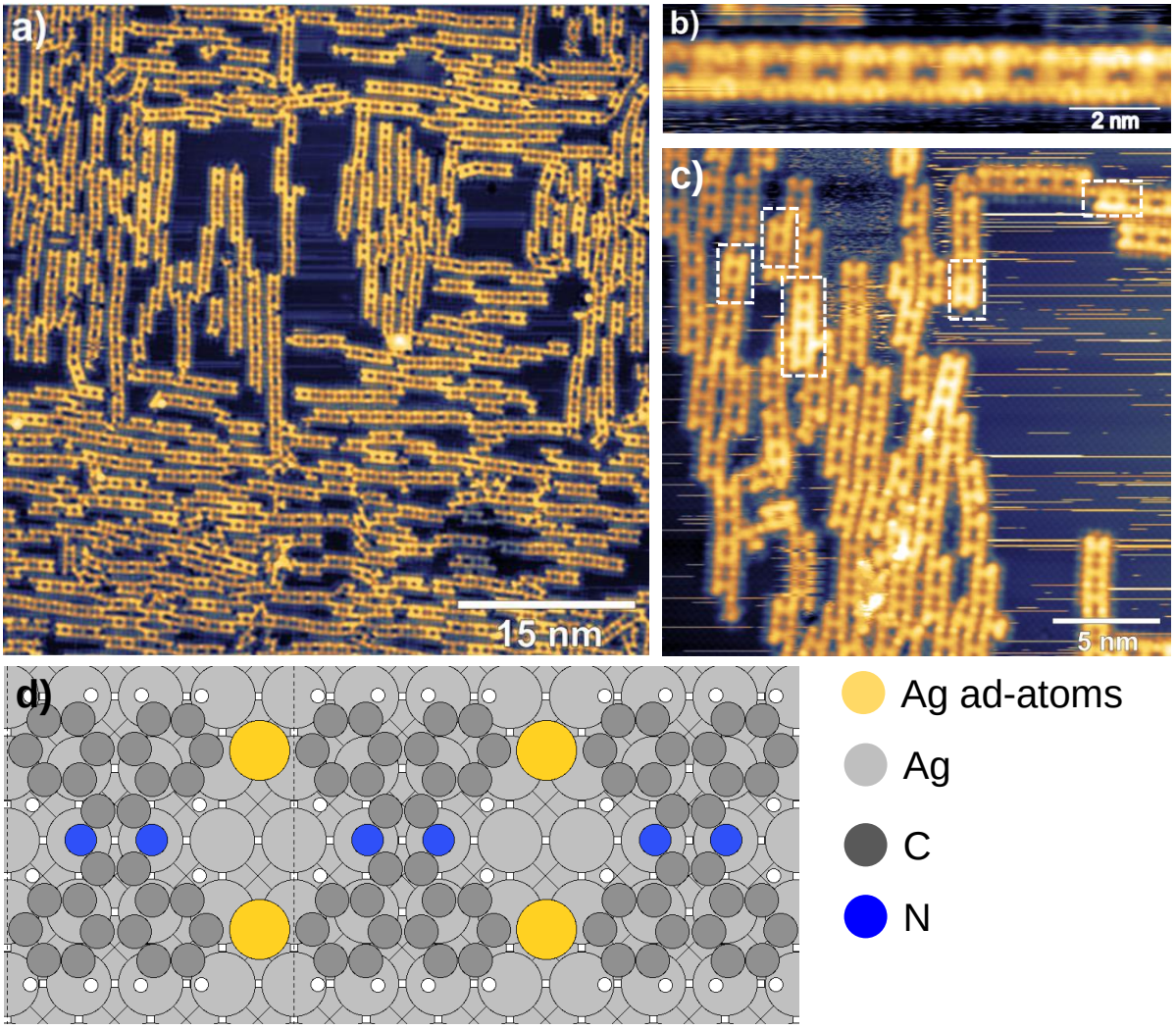

Figure 6.12: (a) Large STM image of the sample after depositing the molecules on the substrate preheated to 450 K. (b) An organometallic chain consisting of 10 monomers, which is growing along ⟨100⟩ Ag axis. (c) High-resolution image of the sample showing the present of some covalent bonds between pair of molecules. (d) Top view of the organometallic chains. The theoretical calculations did not take into account Br adatoms adjacent to the molecule. Tunneling parameters: (a) $V = -1.16\ V$, $I_t = -.69\ nA$, (b) $V = -1.73\ V$, $I_t = -0.81\ nA$, and (c) $V = -1.63\ V$, $I_t = -0.81\ nA$.

the substrate, we identified that the chains are aligned along the main crystallographic directions ⟨100⟩ and ⟨010⟩ of the crystal, which makes sense since the monomer is perfectly commensurate with the side of the square: $8.7\ \mathring{A}/2.9\ \mathring{A} = 3$. From analyzing tens of chains, the average intermolecular separation is found as $(11.4 \pm 0.2)\ \mathring{A}$. Some organometallic chains are decorating by bright and flat features. These features have been identified as molecules covalently bonded (see white rectangles in figure 6.12c), similar to what happened on Cu(111) at the same temperature. Unlike the result obtained on Cu(111), where dimmers are placed at the termination of the C–Cu–C, on Ag(100), dimmers and trimmers do not follow a specific position pattern. Figure 6.12d shows calculations of C–Ag–C chains along ⟨100⟩ direction of Ag(100), being the nitrogen atom

in atop position. The periodic length of 11.5 $\AA$ with C–Ag bonds of 2.136 $\AA$ is predicted by the DFT in perfect agreement with the value obtained from the STM data.

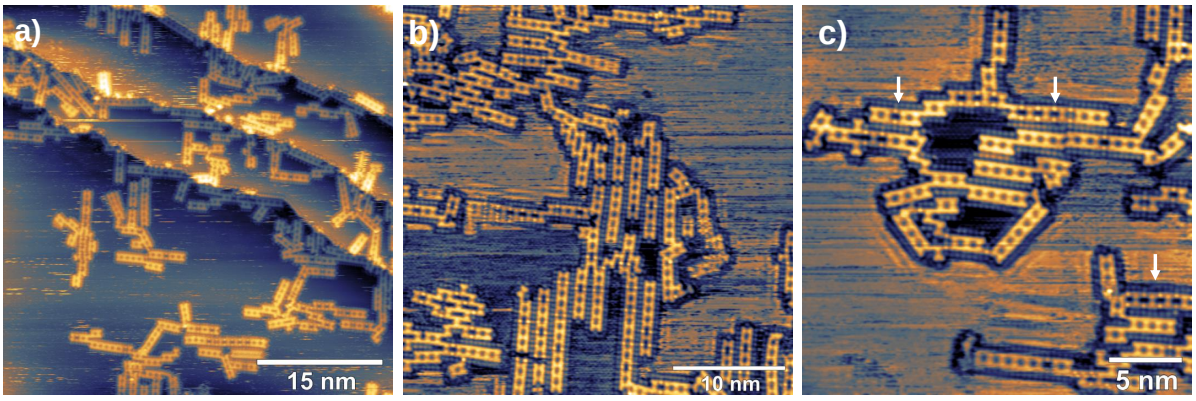

Figure 6.13: (a) Large and (b)-(c) high-resolution STM images in constant current mode acquired after deposition of molecules on Ag(100) substrate maintained at 500 K. Mixed chains, mostly covalent, are observed. White arrows point out C–Ag–C coordination. Tunneling parameters: (a) $V = -1.03\ V$, $I_t = -0.58\ nA$ (b) $V = -0.32\ V$, $I_t = -0.45\ nA$, and (c) $V = -0.75\ V$, $I_t = 1.25\ nA$.

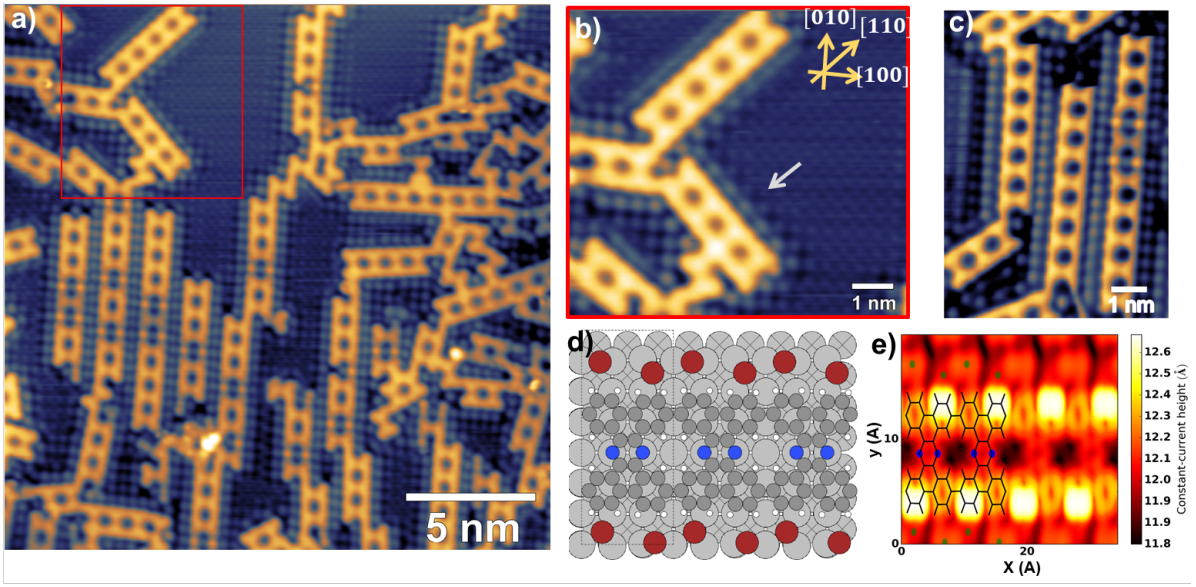

Figure 6.14: (a) STM image of the sample after depositing the molecules on the substrate preheated to 550 K. (b) High resolution STM image where covalent chains can be observed, the position of the Br adatoms is clearly different to the case of mixed wires observed in (c). Covalent wire theoretical model d) STM simulation of covalent wire, using a bias voltage of $V = -1.2\ V$

Figure 6.13 displayed results obtained after deposited the precursor hold the Ag(100) at 500 K. At this temperature, mixed covalent - organometallic chains are synthesized. From the data, it is notice a larger fraction of covalently bonded molecules. In figure 6.13c white arrows indicate C–Ag–C coordination inside the chains.

Figure 6.14 shows the results obtained at 550 K. In this case, mixed chains were found along the same directions of completely organometallic chains. On the other hand,

mostly covalent chains were observed along the ⟨110⟩ direction, as can be seen in detail in figure 6.14b. This is an interesting observation because the monomer has an optimal length of 8.7 $\mathring{A}$, therefore it is not commensurate with the diagonal of the unit square cell (4.1 $\mathring{A}$). Consequently, it is plausible that during the demetallates process some C–C chains reorient easily.

6.3 Conclusions

We have systematically studied on two noble metal substrates of the on-surface reactions and the resulting nanostructures from 2TBTBP, a precursor constituted by phenyl groups functionalized by nitrogen atoms and bromine terminations.

Ullmann coupling reaction in Cu(111) leads to the formation of organometallic motifs at RT, which implies the debromination of the monomer at this temperature. Well-defined C–Cu–C chains were synthesized at 450 K. The terminations of the chains present bright and flat features that we identified as covalent dimmers, which demonstrate the simultaneous activations of the intermediate metallated state and the C–C coupling. A careful study of the resulting nanostructures on Cu(111) in the function of the sample bias was carried out. STM data acquired at a positive and low negative bias ($< -0.20V$) showed complete covalent chains; these are GNRs, usually conformed by four molecules. Both chains coordinated by Cu adatoms and GNRs are aligned at $(25 \pm 2)^\circ$ relatives to substrate main directions. For this orientation, the monomer is entirely commensurable to the surface. From several STM images taken sequentially, we detected the mobile behavior of the GNRs, and occasionally recognized the formation and breaking of the C–C bonds. This result allows us to conclude that the covalent structures are essentially physisorbed at RT (temperature maintained during measurement). In addition, at higher temperatures (500 K), GNRs are observed exclusively around the edges of the steps, typically reported for physisorbed structures. Talirz et al. reported the synthesis AGNRs with a width of 9 C atoms on Au(111), with an electronic band gap of 1.4 eV. In our case, we explored the LDOS of the organometallic chains, less mobile than GNRs at RT, by STS measurements. dI/dV spectra acquired on the N position revels the semiconductor character of these 1D structures.

On Ag(100), deposition keeping the surface at 450 K leads to the coordination of C

radicals with Ag adatoms, forming 1D organometallic chains orientated along ⟨100⟩ and ⟨010⟩ crystallographic directions. At higher temperatures, the formation of C—C coupling is successfully promoted, being possible to image stable structures at RT. However, long ribbons are not obtained. This can be associated with the Br atoms around the chains, which limits the diffusion of the molecules.

Hence, 2TBTBP leads to well-defined GNRs on Cu(111) and Ag(100). However, stable covalent structures are obtained just on Ag(100). In principle, we could explain it by: (1) C-Ag bonds are weaker than C-Cu bonds, which allows to easier demetalate organosilver than organocopper, and (2) the size of the monomer, which is entirely commensurable with the main crystallographic orientations of the Ag(100), being necessary an angle for the Cu(111), which could generate stress on the structure, inhibiting the C–C coupling between covalent dimmers.

Chapter 7

Conclusions and perspective

In this thesis, we presented the successful CVD growth of h-BNC using a new precursor (hexamethylborazine). We demonstrated the role of substrate and temperature on the growth and segregation of the materials (h-BN, Gr, h-BNC) using Rh(111) and Ir(111). The electronic and atomic structures of the obtained monolayer h-BNC were investigated in detail using a comprehensive multiple surface science technique approaches involving XPS, STM, STS, and with a support by DFT calculations. Atomic resolution STM images combined with DFT calculation allowed us to precisely describe how Gr is doped with h-BN clusters. These clusters produce a ring-like structure in the STM images that we named as "h-BN nanodonuts". From our best knowledge, for the first time, we could unambiguously demonstrate that h-BNC is formed by a Gr matrix doped with $(BN)_8$ units as theoretically predicted by Fan *et al.* In addition, we identified that BN clusters sits only in fcc- and hcp-type regions in the particular case of Gr/Ir(111), which limits their concentration and plays an important role on the control of the opening band gap in Gr.

In addition, we study the on-surface synthesis of nanoporous organometallic structures on Ag(100). In particular, a square pore network is obtained from bromine free-base

tetra-phenyl porphyrins (Br4TPP). XPS reveals that the majority of the molecules debrominate upon adsorption at RT, which leads to the formation of C-Ag-C structure via Ullmann coupling reactions. STM and density functional theory (DFT) calculations provide insights into the organometallic structure, identifying the network alignment along <100> directions of the Ag(100) surface, whereas the adsorbates main axis, defined by the pair of the anionic nitrogen atoms, is rotated 90° with respect to these directions. Moreover, the intra-molecular conformation of the debrominated porphyrins has been identified as saddle-shape adsorption geometry. Beside square pores, additional C-Ag-C motifs were observed on the surface, in particular molecular chains absorbed in inverted conformation appeared on the surface in special growth conditions. We investigated the influence of the substrate temperature during molecular deposition on the selectivity of reaction pathways, being found the more favorable parameters for growing pore and chain motifs, in this way it is possible to control the synthesis by substrate temperature.

Furthermore, a surface-assisted Ullmann coupling reaction successfully synthesized well-defined nitrogen-doped porous graphene nanoribbons on Ag(100) and Cu(111). Depending on the growth conditions, 1D organometallic chains are also present on the surfaces. We carried out a detailed study about the influence of the surface substrate temperature during molecular deposition. On Cu(111), short and mobile covalent chains not aligned with the main crystallographic directions of the substrate were obtained. On the other hand, on Ag(100), more extended and stable covalent chains were observed.

Perspectives

We propose to continue investigating the physical properties and functionalities of h-BNC monolayers in order to understand the electronic structure of the graphene-hBN interface. Recently, Kim *et al.* [183] demonstrated the blue-emitting photo-luminescence from 1D heterojunctions of h-BN and graphene in 2D in-plane heterostructures. This result is attributed to localized energy states formed at the disordered boundaries. In this respect, the successful transfer of h-BNC to other substrates that allow its characterization by Transmission Electron Microscopy (TEM) and Photoluminescence Spectroscopy (PL) is requested.

Moreover, 2D metal-organic frameworks are versatile hybrid materials characterized by their porosity, chemical tunability, and high electrical conductivity related to the

delocalization of π electrons. The new square pore organo-metallic network synthesized here represented a rich platform for new physics, considering the possibility of exploring other linker atoms and the on-surface porphyrins metalation, for instance, with magnetic atoms. The principal candidates for this experiment are *3d* transition metals, in particular Cr and Mn since they have partly occupied d subshells, which provides different spin states, leading to formation of 2D spin-systems.

From our research, we learned that synthesizing GNRs from 2TBTBP on Ag(100) is more favorable and stable than on Cu(111). This result could be a consequence of the commensurability of the precursor with the substrate. From that, the study of new substrates such as Ag(110) and Au(100) or Au(110) in order to create longer and fully aligned chains is suggests. Moreover, the surface crystal lattice parameter engineering using Vegard's Law, for example with $Cu_xAu_{(1-x)}$ or $Cu_xAg_{(1-x)}$ alloys such as Cu_3Au, could be other option to have nanoribbons and metallic substrate commensurable.

Bibliography

[1] K. S. Novoselov et al. "Electric Field Effect in Atomically Thin Carbon Films". In: *Science* 306.5696 (2004), pp. 666–669. DOI: 10.1126/science.1102896. eprint: https://www.science.org/doi/pdf/10.1126/science.1102896.

[2] A. K. Geim and K. S. Novoselov. "The rise of graphene". In: *Nature Materials* 6.3 (Mar. 2007), pp. 183–191. DOI: 10.1038/nmat1849.

[3] A. H. Castro Neto et al. "The electronic properties of graphene". In: *Rev. Mod. Phys.* 81 (1 Jan. 2009), pp. 109–162. DOI: 10.1103/RevModPhys.81.109.

[4] K. I. Bolotin et al. "Temperature-Dependent Transport in Suspended Graphene". In: *Phys. Rev. Lett.* 101 (9 Aug. 2008), p. 096802. DOI: 10.1103/PhysRevLett.101.096802.

[5] X. Xu et al. "Interfacial engineering in graphene bandgap". In: *Chem. Soc. Rev.* 47 (9 2018), pp. 3059–3099. DOI: 10.1039/C7CS00836H.

[6] L. Talirz, P. Ruffieux, and R. Fasel. "On-Surface Synthesis of Atomically Precise Graphene Nanoribbons". In: *Advanced Materials* 28.29 (2016), pp. 6222–6231. DOI: https://doi.org/10.1002/adma.201505738. eprint: https://onlinelibrary.wiley.com/doi/pdf/10.1002/adma.201505738.

[7] C.-K. Chang et al. "Band Gap Engineering of Chemical Vapor Deposited Graphene by in Situ BN Doping". In: *ACS Nano* 7.2 (2013). PMID: 23273110, pp. 1333–1341. DOI: 10.1021/nn3049158. eprint: https://doi.org/10.1021/nn3049158.

[8] R. Lv et al. "Nitrogen-doped graphene: beyond single substitution and enhanced molecular sensing." In: *Sci Rep.* 2 (2012). PMID: 22905317, p. 586. DOI: 10.1038/srep00586. eprint: https://doi.org/1PMID:22905317.

[9] D. Y. Usachov et al. "Epitaxial B-Graphene: Large-Scale Growth and Atomic Structure". In: *ACS Nano* 9.7 (2015). PMID: 26121999, pp. 7314–7322. DOI: 10.1021/acsnano.5b02322. eprint: https://doi.org/10.1021/acsnano.5b02322.

[10] Y. He et al. "Fusing tetrapyrroles to graphene edges by surface-assisted covalent coupling". In: *Nature Chemistry* 9.1 (Aug. 2016), pp. 33–38. DOI: 10.1038/nchem.2600.

[11] C. Berger et al. "Ultrathin Epitaxial Graphite: 2D Electron Gas Properties and a Route toward Graphene-based Nanoelectronics". In: *The Journal of Physical Chemistry B* 108.52 (2004), pp. 19912–19916. DOI: 10.1021/jp040650f. eprint: https://doi.org/10.1021/jp040650f.

[12] J. Cai et al. "Atomically precise bottom-up fabrication of graphene nanoribbons". In: *Nature* 466.7305 (July 2010), pp. 470–473. DOI: 10.1038/nature09211.

[13] P. Ruffieux et al. "On-surface synthesis of graphene nanoribbons with zigzag edge topology". In: *Nature* 531(7595) (2016). PMID: 27008967, pp. 489–92. DOI: 10.1038/nature1715. eprint: https://doi.org/10.1038/nature1715.

[14] X.-Y. Wang et al. "Bottom-Up Synthesis of Heteroatom-Doped Chiral Graphene Nanoribbons". In: *Journal of the American Chemical Society* 140.29 (2018). PMID: 29990420, pp. 9104–9107. DOI: 10.1021/jacs.8b06210. eprint: https://doi.org/10.1021/jacs.8b06210.

[15] M. Bieri et al. "Porous graphenes: two-dimensional polymer synthesis with atomic precision". In: *Chem. Commun.* (45 2009), pp. 6919–6921. DOI: 10.1039/B915190G.

[16] J. Bai et al. "Graphene nanomesh". In: *Nature Nanotechnology* 5.3 (Feb. 2010), pp. 190–194. DOI: 10.1038/nnano.2010.8.

[17] L. Grill and S. Hecht. "Covalent on-surface polymerization". In: *Nature Chemistry* 12.2 (Jan. 2020), pp. 115–130. DOI: 10.1038/s41557-019-0392-9.

[18] Q. Fan et al. "Surface-Assisted Organic Synthesis of Hyperbenzene Nanotroughs". In: *Angewandte Chemie International Edition* 52.17 (2013), pp. 4668–4672. DOI: https://doi.org/10.1002/anie.201300610. eprint: https://onlinelibrary.wiley.com/doi/pdf/10.1002/anie.201300610.

[19] R. Nascimento et al. "Band Gaps of BN-Doped Graphene: Fluctuations, Trends, and Bounds". In: *The Journal of Physical Chemistry C* 119.9 (2015), pp. 5055–5061. DOI: 10.1021/jp5101347. eprint: https://doi.org/10.1021/jp5101347.

[20] M. R. Uddin et al. "Carbon-rich hexagonal (BN)C alloys". In: *Journal of Applied Physics* 117.21 (2015), p. 215703. DOI: 10.1063/1.4921931. eprint: https://doi.org/10.1063/1.4921931.

[21] X.-Y. Ren et al. "Non-phase-separated 2D B–C–N alloys via molecule-like carbon doping in 2D BN: atomic structures and optoelectronic properties". In: *Phys. Chem. Chem. Phys.* 20 (35 2018), pp. 23106–23111. DOI: 10.1039/C8CP03028F.

[22] L. Ci et al. "Atomic layers of hybridized boron nitride and graphene domains". In: *Nature Mater* 9 (2010), pp. 430–435. DOI: https://doi.org/10.1038/nmat2711.

[23] S. Nappini et al. "Formation of a Quasi-Free-Standing Single Layer of Graphene and Hexagonal Boron Nitride on Pt(111) by a Single Molecular Precursor". In: *Advanced Functional Materials* 26.7 (2016), pp. 1120–1126. DOI: 10.1002/adfm.201503591. eprint: https://onlinelibrary.wiley.com/doi/pdf/10.1002/adfm.201503591.

[24] F. Leardini et al. "Chemical vapor deposition growth of boron–carbon–nitrogen layers from methylamine borane thermolysis products". In: *Nanotechnology* 29.2 (Dec. 2017), p. 025603. DOI: 10.1088/1361-6528/aa9c07.

[25] R. Y. Tay et al. "Trimethylamine Borane: A New Single-Source Precursor for Monolayer h-BN Single Crystals and h-BCN Thin Films". In: *Chemistry of Materials* 28.7 (2016), pp. 2180–2190. DOI: 10.1021/acs.chemmater.6b00114. eprint: https://doi.org/10.1021/acs.chemmater.6b00114.

[26] K. A. Bokai et al. "Hybrid h-BN–Graphene Monolayer with B–C Boundaries on a Lattice-Matched Surface". In: *Chemistry of Materials* 32.3 (2020), pp. 1172–1181. DOI: 10.1021/acs.chemmater.9b04207. eprint: https://doi.org/10.1021/acs.chemmater.9b04207.

[27] M. Zhang et al. "Two-dimensional boron–nitrogen–carbon monolayers with tunable direct band gaps". In: *Nanoscale* 7 (28 2015), pp. 12023–12029. DOI: 10.1039/C5NR03344F.

[28] I. Guilhon et al. "Optical absorbance and band-gap engineering of $(BN)_{1-x}(C_2)_x$ two-dimensional alloys: Phase separation and composition fluctuation effects". In: *Phys. Rev. B* 95 (3 Jan. 2017), p. 035407. DOI: 10.1103/PhysRevB.95.035407.

[29] R. D'Souza, S. Mukherjee, and T. Saha-Dasgupta. "Influence of interface geometry on phase stability and bandgap engineering in boron nitride substituted graphene: A combined first-principles and Monte Carlo study". In: *Journal of*

Alloys and Compounds 708 (2017), pp. 437–443. DOI: https://doi.org/10.1016/j.jallcom.2017.03.006.

[30] A. Jamróz and J. A. Majewski. "Morphology, Ordering, Stability, and Electronic Structure of Carbon-Doped Hexagonal Boron Nitride". In: *physica status solidi (b)* 256.6 (2019), p. 1800554. DOI: 10.1002/pssb.201800554. eprint: https://onlinelibrary.wiley.com/doi/pdf/10.1002/pssb.201800554.

[31] J. da Rocha Martins and H. Chacham. "Disorder and Segregation in BCN Graphene-Type Layers and Nanotubes: Tuning the Band Gap". In: *ACS Nano* 5.1 (2011). PMID: 21186786, pp. 385–393. DOI: 10.1021/nn101809j. eprint: https://doi.org/10.1021/nn101809j.

[32] Azevedo, S. "Energetic and electronic structure of BC2N compounds". In: *Eur. Phys. J. B* 44.2 (2005), pp. 203–207. DOI: 10.1140/epjb/e2005-00115-6.

[33] S. Beniwal et al. "Graphene-like Boron–Carbon–Nitrogen Monolayers". In: *ACS Nano* 11.3 (2017). PMID: 28165713, pp. 2486–2493. DOI: 10.1021/acsnano.6b08136. eprint: https://doi.org/10.1021/acsnano.6b08136.

[34] C. Zhang et al. "Direct Imaging of Band Profile in Single Layer MoS2 on Graphite: Quasiparticle Energy Gap, Metallic Edge States, and Edge Band Bending". In: *Nano Letters* 14.5 (2014). PMID: 24783945, pp. 2443–2447. DOI: 10.1021/nl501133c. eprint: https://doi.org/10.1021/nl501133c.

[35] S. Kawai et al. "Atomically controlled substitutional boron-doping of graphene nanoribbons". In: *Nature Communications* 6.1 (Aug. 2015). DOI: 10.1038/ncomms9098.

[36] T. Radsar, H. Khalesi, and V. Ghods. "Graphene nanoribbon field effect transistors analysis and applications". In: *Superlattices and Microstructures* 153 (2021), p. 106869. DOI: https://doi.org/10.1016/j.spmi.2021.106869.

[37] T. G. Pedersen et al. "Graphene Antidot Lattices: Designed Defects and Spin Qubits". In: *Phys. Rev. Lett.* 100 (13 Apr. 2008), p. 136804. DOI: 10.1103/PhysRevLett.100.136804.

[38] Q. Sun et al. "On-surface aryl–aryl coupling via selective C–H activation". In: *Chem. Commun.* 50 (80 2014), pp. 11825–11828. DOI: 10.1039/C4CC05482B.

[39] A. Wiengarten et al. "Surface-assisted Dehydrogenative Homocoupling of Porphine Molecules". In: *Journal of the American Chemical Society* 136.26 (2014).

PMID: 24955656, pp. 9346–9354. DOI: 10.1021/ja501680n. eprint: https://doi.org/10.1021/ja501680n.

[40] H.-Y. Gao et al. "Glaser Coupling at Metal Surfaces". In: *Angewandte Chemie International Edition* 52.14 (2013), pp. 4024–4028. DOI: https://doi.org/10.1002/anie.201208597. eprint: https://onlinelibrary.wiley.com/doi/pdf/10.1002/anie.201208597.

[41] J. Liu et al. "Lattice-Directed Formation of Covalent and Organometallic Molecular Wires by Terminal Alkynes on Ag Surfaces". In: *ACS Nano* 9.6 (2015). PMID: 25990647, pp. 6305–6314. DOI: 10.1021/acsnano.5b01803. eprint: https://doi.org/10.1021/acsnano.5b01803.

[42] H.-Y. Gao et al. "Decarboxylative Polymerization of 2,6-Naphthalenedicarboxylic Acid at Surfaces". In: *Journal of the American Chemical Society* 136.27 (2014). PMID: 24937642, pp. 9658–9663. DOI: 10.1021/ja5033875. eprint: https://doi.org/10.1021/ja5033875.

[43] J. Cai et al. "Atomically precise bottom-up fabrication of graphene nanoribbons". In: *Nature* 466 (2010), pp. 470–473. DOI: 10.1038/nature09211. eprint: https://doi.org/10.1038/nature09211.

[44] S. Stolz et al. "Reversible Dehalogenation in On-Surface Aryl–Aryl Coupling". In: *Angewandte Chemie International Edition* 59.33 (2020), pp. 14106–14110. DOI: https://doi.org/10.1002/anie.202005443. eprint: https://onlinelibrary.wiley.com/doi/pdf/10.1002/anie.202005443.

[45] M. Ammon, T. Sander, and S. Maier. "On-Surface Synthesis of Porous Carbon Nanoribbons from Polymer Chains". In: *Journal of the American Chemical Society* 139.37 (2017). PMID: 28820266, pp. 12976–12984. DOI: 10.1021/jacs.7b04783. eprint: https://doi.org/10.1021/jacs.7b04783.

[46] R. Pawlak et al. "Bottom-up Synthesis of Nitrogen-Doped Porous Graphene Nanoribbons". In: *Journal of the American Chemical Society* 142.29 (2020). PMID: 32589029, pp. 12568–12573. DOI: 10.1021/jacs.0c03946. eprint: https://doi.org/10.1021/jacs.0c03946.

[47] A. Basagni et al. "Tunable Band Alignment with Unperturbed Carrier Mobility of On-Surface Synthesized Organic Semiconducting Wires". In: *ACS Nano* 10.2 (2016). PMID: 26841052, pp. 2644–2651. DOI: 10.1021/acsnano.5b07683. eprint: https://doi.org/10.1021/acsnano.5b07683.

[48] W. Li et al. "High temperature ferromagnetism in -conjugated two-dimensional metal–organic frameworks". In: *Chem. Sci.* 8 (4 2017), pp. 2859–2867. DOI: 10.1039/C6SC05080H.

[49] V. Posligua et al. "Engineering the electronic and optical properties of 2D porphyrin-paddlewheel metal-organic frameworks". In: *Journal of Physics Energy* 3.3 (2021). https://doi.org/10.1088/2515-7655/abeab4, p. 034005. DOI: 10.1088/2515-7655/abeab4.

[50] J. S. Lindsey. "Synthetic Routes to meso-Patterned Porphyrins". In: *Accounts of Chemical Research* 43.2 (2010). PMID: 19863076, pp. 300–311. DOI: 10.1021/ar900212t. eprint: https://doi.org/10.1021/ar900212t.

[51] J. M. Gottfried. "Surface chemistry of porphyrins and phthalocyanines". In: *Surface Science Reports* 70.3 (2015), pp. 259–379. DOI: https://doi.org/10.1016/j.surfrep.2015.04.001.

[52] W. Auwärter et al. "Porphyrins at interfaces". In: *Nature Chemistry* 7 (2015), pp. 105–120. DOI: 10.1038/nchem.2159. eprint: https://doi.org/10.1038/nchem.2159.

[53] T. Lin et al. "Self-assembly of metal–organic coordination networks using on-surface synthesized ligands". In: *Chem. Commun.* 50 (97 2014), pp. 15327–15329. DOI: 10.1039/C4CC07604D.

[54] W. Li et al. "High temperature ferromagnetism in -conjugated two-dimensional metal–organic frameworks". In: *Chem. Sci.* 8 (4 2017), pp. 2859–2867. DOI: 10.1039/C6SC05080H.

[55] J. Tuček et al. "Emerging chemical strategies for imprinting magnetism in graphene and related 2D materials for spintronic and biomedical applications". In: *Chem. Soc. Rev.* 47 (11 2018), pp. 3899–3990. DOI: 10.1039/C7CS00288B.

[56] P. R. Wallace. "The Band Theory of Graphite". In: *Phys. Rev.* 71 (9 May 1947), pp. 622–634. DOI: 10.1103/PhysRev.71.622.

[57] P. Zhao et al. "Self-Limiting Chemical Vapor Deposition Growth of Monolayer Graphene from Ethanol". In: *The Journal of Physical Chemistry C* 117.20 (2013), pp. 10755–10763. DOI: 10.1021/jp400996s. eprint: https://doi.org/10.1021/jp400996s.

[58] X. Chen, L. Zhang, and S. Chen. "Large area CVD growth of graphene". In: *Synthetic Metals* 210 (2015). Reviews of Current Advances in Graphene Science

and Technology, pp. 95–108. DOI: https://doi.org/10.1016/j.synthmet.2015.07.005.

[59] C. Backes et al. "Production and processing of graphene and related materials". English. In: *2D materials* 7.2 (2020). DOI: 10.1088/2053-1583/ab1e0a.

[60] M. Corso et al. "Boron Nitride Nanomesh". In: *Science* 303.5655 (2004), pp. 217–220. DOI: 10.1126/science.1091979. eprint: https://science.sciencemag.org/content/303/5655/217.full.pdf.

[61] Q. Dubout et al. "Giant apparent lattice distortions in STM images of corrugated spsup2/sup-hybridised monolayers". In: *New Journal of Physics* 18.10 (Oct. 2016), p. 103027. DOI: 10.1088/1367-2630/18/10/103027.

[62] L. H. de Lima, T. Greber, and M. Muntwiler. "The true corrugation of a h-BN nanomesh layer". In: *2D Materials* 7.3 (Apr. 2020), p. 035006. DOI: 10.1088/2053-1583/ab81ae.

[63] D. Usachov et al. "Nitrogen-Doped Graphene: Efficient Growth, Structure, and Electronic Properties". In: *Nano Letters* 11.12 (2011). PMID: 22077830, pp. 5401–5407. DOI: 10.1021/nl2031037. eprint: https://doi.org/10.1021/nl2031037.

[64] M. Cattelan et al. "Microscopic View on a Chemical Vapor Deposition Route to Boron-Doped Graphene Nanostructures". In: *Chemistry of Materials* 25.9 (2013), pp. 1490–1495. DOI: 10.1021/cm302819b. eprint: https://doi.org/10.1021/cm302819b.

[65] J. Lu et al. "Order–disorder transition in a two-dimensional boron–carbon–nitride alloy". In: *Nat Commun* 4 (2013), p. 2681. DOI: https://doi.org/10.1038/ncomms3681.

[66] D. R. Cooper et al. "Experimental Review of Graphene". In: *ISRN Condensed Matter Physics* 2012 (2012), p. 501686. DOI: 10.5402/2012/501686.

[67] R. W. Lynch and H. G. Drickamer. "Effect of High Pressure on the Lattice Parameters of Diamond, Graphite, and Hexagonal Boron Nitride". In: *The Journal of Chemical Physics* 44.1 (1966), pp. 181–184. DOI: 10.1063/1.1726442. eprint: https://doi.org/10.1063/1.1726442.

[68] R. J. P. Román et al. "Band gap measurements of monolayer h-BN and insights into carbon-related point defects". In: *2D Materials* 8.4 (July 2021), p. 044001. DOI: 10.1088/2053-1583/ac0d9c.

[69] G. Fiori et al. "Lateral Graphene–hBCN Heterostructures as a Platform for Fully Two-Dimensional Transistors". In: *ACS Nano* 6.3 (2012). PMID: 22372431, pp. 2642–2648. DOI: 10.1021/nn300019b. eprint: https://doi.org/10.1021/nn300019b.

[70] D. Alcaraz Iranzo et al. "Probing the ultimate plasmon confinement limits with a van der Waals heterostructure". In: *Science* 360.6386 (2018), pp. 291–295. DOI: 10.1126/science.aar8438. eprint: https://science.sciencemag.org/content/360/6386/291.full.pdf.

[71] M. Li et al. "Graphene with Atomic-Level In-Plane Decoration of h-BN Domains for Efficient Photocatalysis". In: *Chemistry of Materials* 29.7 (2017), pp. 2769–2776. DOI: 10.1021/acs.chemmater.6b04622. eprint: https://doi.org/10.1021/acs.chemmater.6b04622.

[72] S. Chen et al. "Carbon doping of hexagonal boron nitride porous materials toward CO2 capture". In: *J. Mater. Chem. A* 6 (4 2018), pp. 1832–1839. DOI: 10.1039/C7TA08515J.

[73] S. Wang et al. "Band gap-Tunable Porous Borocarbonitride Nanosheets for High Energy-Density Supercapacitors". In: *ACS Applied Materials & Interfaces* 10.23 (2018). PMID: 29775049, pp. 19588–19597. DOI: 10.1021/acsami.8b02317. eprint: https://doi.org/10.1021/acsami.8b02317.

[74] Y. Gao et al. "Toward Single-Layer Uniform Hexagonal Boron Nitride–Graphene Patchworks with Zigzag Linking Edges". In: *Nano Letters* 13.7 (2013). PMID: 23758663, pp. 3439–3443. DOI: 10.1021/nl4021123. eprint: https://doi.org/10.1021/nl4021123.

[75] Y. Gong et al. "Direct chemical conversion of graphene to boron- and nitrogen- and carbon-containing atomic layers". In: *Nature Communications* 5 (2014), p. 3193. DOI: 10.1038/ncomms4193.

[76] R. Gutzler et al. "Halogen bonds as stabilizing interactions in a chiral self-assembled molecular monolayer". In: *Chem. Commun.* 47 (33 2011), pp. 9453–9455. DOI: 10.1039/C1CC13114A.

[77] S. Clair and D. G. de Oteyza. "Controlling a Chemical Coupling Reaction on a Surface: Tools and Strategies for On-Surface Synthesis". In: *Chemical Reviews* 119.7 (2019). PMID: 30875199, pp. 4717–4776. DOI: 10.1021/acs.chemrev.8b00601. eprint: https://doi.org/10.1021/acs.chemrev.8b00601.

[78] L. Grill et al. "Nano-architectures by covalent assembly of molecular building blocks". In: *Nature Nanotechnology* 2 (2007), pp. 687–691. DOI: 10.1038/nnano.2007.346. eprint: https://doi.org/10.1038/nnano.2007.346.

[79] O. Ourdjini et al. "Substrate-mediated ordering and defect analysis of a surface covalent organic framework". In: *Phys. Rev. B* 84 (12 Sept. 2011), p. 125421. DOI: 10.1103/PhysRevB.84.125421.

[80] C. Moreno et al. "Critical Role of Phenyl Substitution and Catalytic Substrate in the Surface-Assisted Polymerization of Dibromobianthracene Derivatives". In: *Chemistry of Materials* 31.2 (2019), pp. 331–341. DOI: 10.1021/acs.chemmater.8b03094. eprint: https://doi.org/10.1021/acs.chemmater.8b03094.

[81] E. Rabinowitch. "Spectra of Porphyrins and Chlorophyll". In: *Rev. Mod. Phys.* 16 (3-4 July 1944), pp. 226–235. DOI: 10.1103/RevModPhys.16.226.

[82] H. L. Bonkovsky et al. "Porphyrin and Heme Metabolism and the Porphyrias". In: *Comprehensive Physiology*. John Wiley Sons, Ltd, 2013, pp. 365–401. DOI: https://doi.org/10.1002/cphy.c120006. eprint: https://onlinelibrary.wiley.com/doi/pdf/10.1002/cphy.c120006.

[83] P. Zucca et al. "Biomimetic metalloporphines and metalloporphyrins as potential tools for delignification: Molecular mechanisms and application perspectives". In: *Journal of Molecular Catalysis A: Chemical* 388-389 (2014). Special Issue on Biomass Catalysis, pp. 2–34. DOI: https://doi.org/10.1016/j.molcata.2013.09.010.

[84] R. H. Friend et al. "Electroluminescence in conjugated polymers". In: *Nature* 397.6715 (Jan. 1999), pp. 121–128. DOI: 10.1038/16393.

[85] W. Wu, Y. Liu, and D. Zhu. "-Conjugated molecules with fused rings for organic field-effect transistors: design, synthesis and applications". In: *Chem. Soc. Rev.* 39 (5 2010), pp. 1489–1502. DOI: 10.1039/B813123F.

[86] D. S. Hecht et al. "Bioinspired Detection of Light Using a Porphyrin-Sensitized Single-Wall Nanotube Field Effect Transistor". In: *Nano Letters* 6.9 (2006). PMID: 16968021, pp. 2031–2036. DOI: 10.1021/nl061231s. eprint: https://doi.org/10.1021/nl061231s.

[87] M. Lepper et al. "Adsorption Behavior of a Cyano-Functionalized Porphyrin on Cu(111) and Ag(111): From Molecular Wires to Ordered Supramolecular Two-Dimensional Aggregates". In: *The Journal of Physical Chemistry C* 121.47 (2017),

pp. 26361–26371. DOI: 10.1021/acs.jpcc.7b08382. eprint: https://doi.org/10.1021/acs.jpcc.7b08382.

[88] A. Taylor. "Practical surface analysis, 2nd edn., vol I, auger and X-ray photoelectron spectroscopy. Edited by D. Briggs & M. P. Seah, John Wiley, New York, 1990, 657 pp., price: £86.50. ISBN 0471 92081 9". In: *Journal of Chemical Technology & Biotechnology* 53.2 (1992), pp. 215–215. DOI: https://doi.org/10.1002/jctb.280530219. eprint: https://onlinelibrary.wiley.com/doi/pdf/10.1002/jctb.280530219.

[89] K. Oura et al. "Surface Analysis II. Electron Spectroscopy Methods". In: *Surface Science*. Springer, 2003, pp. 77–108.

[90] W. Egelhoff. "Core-level binding-energy shifts at surfaces and in solids". In: *Surface Science Reports* 6.6 (1987), pp. 253–415. DOI: https://doi.org/10.1016/0167-5729(87)90007-0.

[91] J. VICKERMAN. "The principal techniques." In: *Surface analysis*. Wiley, 2009.

[92] J. M. Lannon Jr and C. D. Stinespring. "Auger Electron Spectroscopy in Analysis of Surfaces". In: *Encyclopedia of Analytical Chemistry*. John Wiley Sons, Ltd, 2006. DOI: https://doi.org/10.1002/9780470027318.a2503. eprint: https://onlinelibrary.wiley.com/doi/pdf/10.1002/9780470027318.a2503.

[93] D. M. Hercules and S. H. Hercules. "Analytical chemistry of surfaces. Part II. Electron spectroscopy". In: *Journal of Chemical Education* 61.6 (1984), p. 483. DOI: 10.1021/ed061p483. eprint: https://doi.org/10.1021/ed061p483.

[94] A. Damascelli, Z. Hussain, and Z.-X. Shen. "Angle-resolved photoemission studies of the cuprate superconductors". In: *Rev. Mod. Phys.* 75 (2 Apr. 2003), pp. 473–541. DOI: 10.1103/RevModPhys.75.473.

[95] D. A. Shirley. "High-Resolution X-Ray Photoemission Spectrum of the Valence Bands of Gold". In: *Phys. Rev. B* 5 (12 June 1972), pp. 4709–4714. DOI: 10.1103/PhysRevB.5.4709.

[96] G. H. Major et al. "Practical guide for curve fitting in x-ray photoelectron spectroscopy". In: *Journal of Vacuum Science & Technology A* 38.6 (2020), p. 061203. DOI: 10.1116/6.0000377. eprint: https://doi.org/10.1116/6.0000377.

[97] R. Wiesendanger. *Scanning Probe Microscopy and Spectroscopy: Methods and Applications*. Cambridge University Press, 1994. DOI: 10.1017/CBO9780511524356.

[98] C. J. Chen. *Introduction to Scanning Tunneling Microscopy: Second Edition*. Oxford, 2007. DOI: 10.1093/acprof:oso/9780199211500.001.0001.

[99] I. Horcas et al. "WSXM: A software for scanning probe microscopy and a tool for nanotechnology". In: *Review of Scientific Instruments* 78.1 (2007), p. 013705. DOI: 10.1063/1.2432410. eprint: https://doi.org/10.1063/1.2432410.

[100] D. Nečas and P. Klapetek. "Gwyddion: an open-source software for SPM data analysis". In: *Open Physics* 10.1 (2012), pp. 181–188. DOI: https://doi.org/10.2478/s11534-011-0096-2.

[101] W. Liu et al. "Two-Dimensional Polymer Synthesized via Solid-State Polymerization for High-Performance Supercapacitors". In: *ACS Nano* 12.1 (2018). PMID: 29244482, pp. 852–860. DOI: 10.1021/acsnano.7b08354. eprint: https://doi.org/10.1021/acsnano.7b08354.

[102] G. Castro, J. Küppers, and Y. Ivashchenko. "Sputtering of CoSi(100) and CoSi2(100) single crystal surfaces". In: *Applications of Surface Science* 16.3 (1983), pp. 453–462. DOI: https://doi.org/10.1016/0378-5963(83)90086-7.

[103] M. Liu et al. "Quasi-Freestanding Monolayer Heterostructure of Graphene and Hexagonal Boron Nitride on Ir(111) with a Zigzag Boundary". In: *Nano Letters* 14.11 (2014). PMID: 25268563, pp. 6342–6347. DOI: 10.1021/nl502780u. eprint: https://doi.org/10.1021/nl502780u.

[104] M. Petrović et al. "Microanalysis of single-layer hexagonal boron nitride islands on Ir(111)". In: *Applied Surface Science* 420 (2017), pp. 504–510. DOI: https://doi.org/10.1016/j.apsusc.2017.05.155.

[105] F. H. Farwick zum Hagen et al. "Structure and Growth of Hexagonal Boron Nitride on Ir(111)". In: *ACS Nano* 10.12 (2016). PMID: 28024332, pp. 11012–11026. DOI: 10.1021/acsnano.6b05819. eprint: https://doi.org/10.1021/acsnano.6b05819.

[106] F. Orlando et al. "Epitaxial Growth of Hexagonal Boron Nitride on Ir(111)". In: *The Journal of Physical Chemistry C* 116.1 (2012), pp. 157–164. DOI: 10.1021/jp207571n. eprint: https://doi.org/10.1021/jp207571n.

[107] F. Orlando et al. "Epitaxial Growth of a Single-Domain Hexagonal Boron Nitride Monolayer". In: *ACS Nano* 8.12 (2014). PMID: 25389799, pp. 12063–12070. DOI: 10.1021/nn5058968. eprint: https://doi.org/10.1021/nn5058968.

[108] F. Schulz et al. "Epitaxial hexagonal boron nitride on Ir(111): A work function template". In: *Phys. Rev. B* 89 (23 June 2014), p. 235429. DOI: 10.1103/PhysRevB.89.235429.

[109] G. Dong et al. "How Boron Nitride Forms a Regular Nanomesh on Rh(111)". In: *Phys. Rev. Lett.* 104 (9 Mar. 2010), p. 096102. DOI: 10.1103/PhysRevLett.104.096102.

[110] G. C. Dong et al. "Graphene formation on metal surfaces investigated by in-situ scanning tunneling microscopy". In: *New Journal of Physics* 14.5 (May 2012), p. 053033. DOI: 10.1088/1367-2630/14/5/053033.

[111] D. Usachov et al. "Experimental and computational insight into the properties of the lattice-mismatched structures: Monolayers of *h*-BN and graphene on Ir(111)". In: *Phys. Rev. B* 86 (15 Oct. 2012), p. 155151. DOI: 10.1103/PhysRevB.86.155151.

[112] Y. Qi et al. "Strong Adlayer–Substrate Interactions "Break" the Patching Growth of h-BN onto Graphene on Re(0001)". In: *ACS Nano* 11.2 (2017). PMID: 28110522, pp. 1807–1815. DOI: 10.1021/acsnano.6b07773. eprint: https://doi.org/10.1021/acsnano.6b07773.

[113] A. T. N'Diaye et al. "Structure of epitaxial graphene on Ir(111)". In: *New Journal of Physics* 10.4 (Apr. 2008), p. 043033. DOI: 10.1088/1367-2630/10/4/043033.

[114] H. Hattab et al. "Growth temperature dependent graphene alignment on Ir(111)". In: *Applied Physics Letters* 98.14 (2011), p. 141903. DOI: 10.1063/1.3548546. eprint: https://doi.org/10.1063/1.3548546.

[115] C. Busse et al. "Graphene on Ir(111): Physisorption with Chemical Modulation". In: *Phys. Rev. Lett.* 107 (3 July 2011), p. 036101. DOI: 10.1103/PhysRevLett.107.036101.

[116] W. J. Arnoult and R. B. McLellan. "The solubility of carbon in rhodium ruthenium, iridium and rhenium". In: *Scripta Metallurgica* 6.10 (1972), pp. 1013–1018. DOI: https://doi.org/10.1016/0036-9748(72)90163-9.

[117] M. Liu et al. "Single and Polycrystalline Graphene on Rh(111) Following Different Growth Mechanisms". In: *Small* 9.8 (2013), pp. 1360–1366. DOI: 10.1002/smll.201202962. eprint: https://onlinelibrary.wiley.com/doi/pdf/10.1002/smll.201202962.

[118] A. Celis et al. "Growth, morphology and electronic properties of epitaxial graphene on vicinal Ir(332) surface". In: *Nanotechnology* 31.28 (Apr. 2020), p. 285601. DOI: 10.1088/1361-6528/ab866a.

[119] S. Günther et al. "High-Temperature Scanning Tunneling Microscopy Study of the Ordering Transition of an Amorphous Carbon Layer into Graphene on Ruthenium(0001)". In: *ACS Nano* 7.1 (2013). PMID: 23214506, pp. 154–164. DOI: 10.1021/nn303468j. eprint: https://doi.org/10.1021/nn303468j.

[120] M. Sicot et al. "Nucleation and growth of nickel nanoclusters on graphene Moire on Rh(111)". In: *Applied Physics Letters* 96 (Mar. 2010). DOI: 10.1063/1.3341176.

[121] E. N. Voloshina et al. "Graphene on Rh(111): Scanning tunneling and atomic force microscopies studies". In: *Applied Physics Letters* 100.24 (2012), p. 241606. DOI: 10.1063/1.4729549. eprint: https://doi.org/10.1063/1.4729549.

[122] M. Yang et al. "Metal-graphene interfaces in epitaxial and bulk systems: A review". In: *Progress in Materials Science* 110 (2020), p. 100652. DOI: https://doi.org/10.1016/j.pmatsci.2020.100652.

[123] O. Kordina et al. "High temperature chemical vapor deposition of SiC". In: *Applied Physics Letters* 69.10 (1996), pp. 1456–1458. DOI: 10.1063/1.117613. eprint: https://doi.org/10.1063/1.117613.

[124] A. Ellison et al. "High temperature CVD growth of SiC". In: *Materials Science and Engineering: B* 61-62 (1999), pp. 113–120. DOI: https://doi.org/10.1016/S0921-5107(98)00482-6.

[125] R. Laskowski et al. "Single-Layer Model of the Hexagonal Boron Nitride Nanomesh on the Rh(111) Surface". In: *Phys. Rev. Lett.* 98 (10 Mar. 2007), p. 106802. DOI: 10.1103/PhysRevLett.98.106802.

[126] A. Preobrajenski et al. "Monolayer h-BN on lattice-mismatched metal surfaces: On the formation of the nanomesh". In: *Chemical Physics Letters* 446.1 (2007), pp. 119–123. DOI: https://doi.org/10.1016/j.cplett.2007.08.028.

[127] X. Liu et al. "Point Defects and Grain Boundaries in Rotationally Commensurate MoS2 on Epitaxial Graphene". In: *The Journal of Physical Chemistry C* 120.37 (2016), pp. 20798–20805. DOI: 10.1021/acs.jpcc.6b02073. eprint: https://doi.org/10.1021/acs.jpcc.6b02073.

[128] A. Bruix et al. "Single-layer MoS_2 on Au(111): Band gap renormalization and substrate interaction". In: *Phys. Rev. B* 93 (16 Apr. 2016), p. 165422. DOI: 10.1103/PhysRevB.93.165422.

[129] Q. Li et al. "Grain Boundary Structures and Electronic Properties of Hexagonal Boron Nitride on Cu(111)". In: *Nano Letters* 15.9 (2015). PMID: 26244850, pp. 5804–5810. DOI: 10.1021/acs.nanolett.5b01852. eprint: https://doi.org/10.1021/acs.nanolett.5b01852.

[130] B. Hwang et al. "Electron-beam assisted growth of hexagonal boron-nitride layer". In: *Current Applied Physics* 13.7 (2013), pp. 1365–1369. DOI: https://doi.org/10.1016/j.cap.2013.04.018.

[131] C. Elias et al. "Direct band-gap crossover in epitaxial monolayer boron nitride". In: *Nature Communications* 10 (2019), p. 2649. DOI: 10.1038/s41467-019-10610-5.

[132] F. Paleari et al. "Excitons in few-layer hexagonal boron nitride: Davydov splitting and surface localization". In: *2D Materials* 5.4 (Aug. 2018), p. 045017. DOI: 10.1088/2053-1583/aad586.

[133] J. Coraux et al. "Growth of graphene on Ir(111)". In: *New Journal of Physics* 11.3 (Mar. 2009), p. 039801. DOI: 10.1088/1367-2630/11/3/039801.

[134] E. N. Voloshina et al. "Electronic structure and imaging contrast of graphene moiré on metals". In: *Sci Rep.* 3 (2013), p. 1072. DOI: 10.1038/srep01072.

[135] M. S. C. Mazzoni et al. "Electronic structure and energetics of $B_xC_yN_z$ layered structures". In: *Phys. Rev. B* 73 (7 Feb. 2006), p. 073108. DOI: 10.1103/PhysRevB.73.073108.

[136] K. Yuge. "Phase stability of boron carbon nitride in a heterographene structure: A first-principles study". In: *Phys. Rev. B* 79 (14 Apr. 2009), p. 144109. DOI: 10.1103/PhysRevB.79.144109.

[137] X. Ren et al. "Opening of Band Gap of Graphene with High Electronic Mobility by Codoping BN Pairs". In: *Chemical Research in Chinese Universities* 35.6 (2019), pp. 1058–1061. DOI: 10.1007/s40242-019-9151-0.

[138] A. T. N'Diaye et al. "Two-Dimensional Ir Cluster Lattice on a Graphene Moiré on Ir(111)". In: *Phys. Rev. Lett.* 97 (21 Nov. 2006), p. 215501. DOI: 10.1103/PhysRevLett.97.215501.

[139] R. Balog et al. "Bandgap opening in graphene induced by patterned hydrogen adsorption". In: *Nature Materials* 9 (2010), pp. 315–319. DOI: 10.1038/nmat2710.

[140] X. Fan et al. "Band gap opening of graphene by doping small boron nitride domains". In: *Nanoscale* 4 (6 2012), pp. 2157–2165. DOI: 10.1039/C2NR11728B.

[141] S. Azevedo. "Energetic stability of B–C–N monolayer". In: *Physics Letters A* 351.1 (2006), pp. 109–112. DOI: https://doi.org/10.1016/j.physleta.2005.10.053.

[142] J. Tersoff and D. R. Hamann. "Theory and Application for the Scanning Tunneling Microscope". In: *Phys. Rev. Lett.* 50 (25 June 1983), pp. 1998–2001. DOI: 10.1103/PhysRevLett.50.1998.

[143] J. Tersoff and D. R. Hamann. "Theory of the scanning tunneling microscope". In: *Phys. Rev. B* 31 (2 Jan. 1985), pp. 805–813. DOI: 10.1103/PhysRevB.31.805.

[144] S. K. Hämäläinen et al. "Structure and local variations of the graphene moiré on Ir(111)". In: *Phys. Rev. B* 88 (20 Nov. 2013), p. 201406. DOI: 10.1103/PhysRevB.88.201406.

[145] P. Lacovig et al. "Growth of Dome-Shaped Carbon Nanoislands on Ir(111): The Intermediate between Carbidic Clusters and Quasi-Free-Standing Graphene". In: *Phys. Rev. Lett.* 103 (16 Oct. 2009), p. 166101. DOI: 10.1103/PhysRevLett.103.166101.

[146] R. C. de Campos Ferreira et al. "Unraveling the Atomic Structure of Fe Intercalated under Graphene on Ir(111): A Multitechnique Approach". In: *Chemistry of Materials* 30.20 (2018), pp. 7201–7210. DOI: 10.1021/acs.chemmater.8b03186. eprint: https://doi.org/10.1021/acs.chemmater.8b03186.

[147] L. Cheng et al. "Two-dimensional hexagonal boron–carbon–nitrogen atomic layers". In: *Nanoscale* 11 (21 2019), pp. 10454–10462. DOI: 10.1039/C9NR00712A.

[148] K. Ba et al. "Chemical and Bandgap Engineering in Monolayer Hexagonal Boron Nitride". In: *Scientific Reports* 7 (1 2017), p. 45584. DOI: 10.1038/srep45584.

[149] C. Chen et al. "Electronic structure of graphene/hexagonal boron nitride heterostructure revealed by Nano-ARPES". In: *Journal of Physics: Conference Series* 864 (June 2017), p. 012005. DOI: 10.1088/1742-6596/864/1/012005.

[150] S. Lisi et al. "Observation of flat bands in twisted bilayer graphene". In: *Nature Physics* 17 (Sept. 2021), p. 189. DOI: 10.1038/s41567-020-01041-x.

[151] M. Lepper et al. ""Inverted" porphyrins: a distorted adsorption geometry of free-base porphyrins on Cu(111)". In: *Chem. Commun.* 53 (58 2017), pp. 8207–8210. DOI: 10.1039/C7CC04182A.

[152] J. C. Moreno-López et al. "Roles of Precursor Conformation and Adatoms in Ullmann Coupling: An Inverted Porphyrin on Cu(111)". In: *Chemistry of Materials* 31.8 (2019), pp. 3009–3017. DOI: 10.1021/acs.chemmater.9b00668. eprint: https://doi.org/10.1021/acs.chemmater.9b00668.

[153] A. Ceccatto dos Santos et al. "Cyano-Functionalized Porphyrins on Cu(111) from One-Dimensional Wires to Two-Dimensional Molecular Frameworks: On the Role of Co-Deposited Metal Atoms". In: *Chemistry of Materials* 32.5 (2020), pp. 2114–2122. DOI: 10.1021/acs.chemmater.9b05256. eprint: https://doi.org/10.1021/acs.chemmater.9b05256.

[154] P. T. P. Ryan et al. "Validation of the inverted adsorption structure for free-base tetraphenyl porphyrin on Cu(111)". In: *Chem. Commun.* 56 (25 2020), pp. 3681–3684. DOI: 10.1039/C9CC09638H.

[155] A. Ceccatto dos Santos et al. "Reassessing the Adsorption Behavior and on-Surface Reactivity of a Brominated Porphyrin on Cu(111)". In: *The Journal of Physical Chemistry C* 125.31 (2021), pp. 17164–17173. DOI: 10.1021/acs.jpcc.1c03346. eprint: https://doi.org/10.1021/acs.jpcc.1c03346.

[156] B. Cirera et al. "On-Surface Synthesis of Gold Porphyrin Derivatives via a Cascade of Chemical Interactions: Planarization, Self-Metalation, and Intermolecular Coupling". In: *Chemistry of Materials* 31.9 (2019), pp. 3248–3256. DOI: 10.1021/acs.chemmater.9b00125. eprint: https://doi.org/10.1021/acs.chemmater.9b00125.

[157] R. C. de Campos Ferreira et al. "Supramolecular Ordering and Reactions of a Chlorophenyl Porphyrin on Ag(111)". In: *The Journal of Physical Chemistry C* 124.26 (2020), pp. 14220–14228. DOI: 10.1021/acs.jpcc.0c02953. eprint: https://doi.org/10.1021/acs.jpcc.0c02953.

[158] T. A. Pham et al. "Self-assembly of pyrene derivatives on Au(111): substituent effects on intermolecular interactions". In: *Chem. Commun.* 50 (91 2014), pp. 14089–14092. DOI: 10.1039/C4CC02753A.

[159] L. Colazzo et al. "On-surface synthesis of heptacene on Ag(001) from brominated and non-brominated tetrahydroheptacene precursors". In: *Chem. Commun.* 54 (73 2018), pp. 10260–10263. DOI: 10.1039/C8CC04402C.

[160] M. Ammon et al. "On-Surface Synthesis of Porous Carbon Nanoribbons on Silver: Reaction Kinetics and the Influence of the Surface Structure". In: *ChemPhysChem* 20.18 (2019), pp. 2333–2339. DOI: https://doi.org/10.1002/cphc.201900347.

eprint: https://chemistry-europe.onlinelibrary.wiley.com/doi/pdf/10.1002/cphc.201900347.

[161] M. Lischka et al. "On-Surface Polymerization of 1,6-Dibromo-3,8-diiodpyrene—A Comparative Study on Au(111) Versus Ag(111) by STM, XPS, and NEXAFS". In: *The Journal of Physical Chemistry C* 122.11 (2018), pp. 5967–5977. DOI: 10.1021/acs.jpcc.7b10403. eprint: https://doi.org/10.1021/acs.jpcc.7b10403.

[162] B. Cirera et al. "Thermal selectivity of intermolecular versus intramolecular reactions on surfacesth". In: *Nature Communications* 7 (2016), p. 11002. DOI: 10.1038/ncomms11002. eprint: https://doi.org/10.1038/ncomms11002.

[163] J. Eichhorn et al. "On-Surface Ullmann Coupling: The Influence of Kinetic Reaction Parameters on the Morphology and Quality of Covalent Networks". In: *ACS Nano* 8.8 (2014). PMID: 25036422, pp. 7880–7889. DOI: 10.1021/nn501567p. eprint: https://doi.org/10.1021/nn501567p.

[164] J. Eichhorn et al. "On-surface Ullmann polymerization via intermediate organometallic networks on Ag(111)". In: *Chem. Commun.* 50 (57 2014), pp. 7680–7682. DOI: 10.1039/C4CC02757D.

[165] N. Kalashnyk et al. "The Orientation of Silver Surfaces Drives the Reactivity and the Selectivity in Homo-Coupling Reactions". In: *ChemPhysChem* 19.15 (2018), pp. 1802–1808. DOI: https://doi.org/10.1002/cphc.201800406. eprint: https://chemistry-europe.onlinelibrary.wiley.com/doi/pdf/10.1002/cphc.201800406.

[166] M. Langelaar, M. Breeman, and D. Boerma. "Mobility of Ag adatoms on Ag(100)". In: *Surface Science* 352-354 (1996). Proceedings of the 15th European Conference on Surface Science, pp. 597–601. DOI: https://doi.org/10.1016/0039-6028(95)01208-7.

[167] W. Auwärter et al. "Conformational Adaptation and Selective Adatom Capturing of Tetrapyridyl-porphyrin Molecules on a Copper (111) Surface". In: *Journal of the American Chemical Society* 129.36 (2007). PMID: 17705476, pp. 11279–11285. DOI: 10.1021/ja071572n. eprint: https://doi.org/10.1021/ja071572n.

[168] W. Auwärter et al. "Site-specific electronic and geometric interface structure of Co-tetraphenyl-porphyrin layers on Ag(111)". In: *Phys. Rev. B* 81 (24 June 2010), p. 245403. DOI: 10.1103/PhysRevB.81.245403.

[169] W. Auwärter et al. "A surface-anchored molecular four-level conductance switch based on single proton transfer". In: *Nature Nanotechnology* 7 (2012), pp. 41–46. DOI: 10.1038/nnano.2011.211. eprint: https://doi.org/10.1038/nnano.2011.211.

[170] S. P. Jarvis et al. "Physisorption Controls the Conformation and Density of States of an Adsorbed Porphyrin". In: *The Journal of Physical Chemistry C* 119.50 (2015), pp. 27982–27994. DOI: 10.1021/acs.jpcc.5b08350. eprint: https://doi.org/10.1021/acs.jpcc.5b08350.

[171] K. Seufert et al. "Cis-dicarbonyl binding at cobalt and iron porphyrins with saddle-shape conformation". In: *Nature Chemistry* 2 (2011), pp. 114–119. DOI: doi.org/10.1038/nchem.956. eprint: https://doi.org/10.1038/nchem.956.

[172] A. Baklanov et al. "On-Surface Synthesis of Nonmetal Porphyrins". In: *Journal of the American Chemical Society* 142.4 (2020). PMID: 31944105, pp. 1871–1881. DOI: 10.1021/jacs.9b10711. eprint: https://doi.org/10.1021/jacs.9b10711.

[173] F. Albrecht et al. "Direct Identification and Determination of Conformational Response in Adsorbed Individual Nonplanar Molecular Species Using Noncontact Atomic Force Microscopy". In: *Nano Letters* 16.12 (2016). PMID: 27779886, pp. 7703–7709. DOI: 10.1021/acs.nanolett.6b03769. eprint: https://doi.org/10.1021/acs.nanolett.6b03769.

[174] T. Vogl et al. "Compact Cavity-Enhanced Single-Photon Generation with Hexagonal Boron Nitride". In: *ACS Photonics* 6.8 (2019), pp. 1955–1962. DOI: 10.1021/acsphotonics.9b00314. eprint: https://doi.org/10.1021/acsphotonics.9b00314.

[175] C.-X. Wang et al. "On-surface synthesis of 2D COFs on Cu(111) via the formation of thermodynamically stable organometallic networks as the template". In: *Phys. Chem. Chem. Phys.* 21 (24 2019), pp. 13222–13229. DOI: 10.1039/C9CP01843C.

[176] J. D. Teeter et al. "Epitaxial growth of aligned atomically precise chevron graphene nanoribbons on Cu(111)". In: *Chem. Commun.* 53 (60 2017), pp. 8463–8466. DOI: 10.1039/C6CC08006E.

[177] M. Böhringer et al. "Reversed surface corrugation in STM images on Au(111) by field-induced lateral motion of adsorbed molecules". In: *Surface Science* 457.1 (2000), pp. 37–50. DOI: https://doi.org/10.1016/S0039-6028(00)00368-X.

[178] M. Wessendorf et al. "Electronic surface structure of n -ML Ag/Cu(111) and Cs/n -ML Ag/Cu(111) as investigated by 2PPE and STS". In: *Applied Physics A:*

Materials Science &amp Processing 78.2 (Jan. 2004), pp. 183–188. DOI: 10.1007/s00339-003-2313-3.

[179] F. E. Olsson et al. "Localization of the Cu(111) Surface State by Single Cu Adatoms". In: *Phys. Rev. Lett.* 93 (20 Nov. 2004), p. 206803. DOI: 10.1103/PhysRevLett.93.206803.

[180] J. Kröger et al. "Stark effect in Au„111... and Cu„111... surface states". In: *Physical Review B* 70.3 (July 2004). DOI: 10.1103/physrevb.70.033401.

[181] L. Talirz et al. "On-Surface Synthesis and Characterization of 9-Atom Wide Armchair Graphene Nanoribbons". In: *ACS Nano* 11.2 (2017). PMID: 28129507, pp. 1380–1388. DOI: 10.1021/acsnano.6b06405. eprint: https://doi.org/10.1021/acsnano.6b06405.

[182] R. Pawlak et al. "Bottom-up Synthesis of Nitrogen-Doped Porous Graphene Nanoribbons". In: *Journal of the American Chemical Society* 142.29 (2020). PMID: 32589029, pp. 12568–12573. DOI: 10.1021/jacs.0c03946. eprint: https://doi.org/10.1021/jacs.0c03946.

[183] G. Kim et al. "Blue emission at atomically sharp 1D heterojunctions between graphene and h-BN". In: *Nature Communications* 11.1 (Oct. 2020). DOI: 10.1038/s41467-020-19181-2.